TRAVERSING THE ELASTIC LANDSCAPE WITH THE POLYMER BRUSH ARCHITECTURE: LESSONS IN THE PURSUIT OF NATURE

Andrew Nicolas Keith

A dissertation submitted to the faculty at the University of North Carolina at Chapel Hill in partial fulfillment of the requirements for the degree of Doctor of Philosophy in the Department of Chemistry.

Chapel Hill
2020

Approved by:

Sergei Sheiko

Frank Leibfarth

Wei You

Abigail Knight

Stephen Craig

ABSTRACT

Andrew Nicolas Keith: Traversing the Elastic Landscape with the Polymer Brush Architecture: Lessons in the Pursuit of Nature
(Under the direction of Sergei Sheiko)

This dissertation draws inspiration from the unique mechanical properties of living tissue to develop a synthetic platform that can replicate tissue's unmatched elastic combinations of softness and firmness. Furthermore, contemporary polymer network models reveal an absence of a single materials design platform that enables sweeping control of both their softness and firmness to traverse the entire elastic landscape. Herein, the brush architecture incorporated into self-assembled linear-brush-linear (LBL) thermoplastic elastomers (plastomers) provides a pathway to filling this void. The platform's highly tunable architectural features are programmed through controlled atom transfer radical polymerization (ATRP) of polydimethylsiloxane (PDMS) macromonomers into brushes with subsequent growth of polymethylmethacrylate (PMMA) linear blocks to achieve various brush block lengths (n_{bb}), brush side chain lengths (n_{sc}), and linear block lengths (n_L) or volume fractions (ϕ_L). Strong phase separation of the compositionally and architecturally distinct blocks empowers the platform with enhanced firmness. Independent variation of ϕ_L and targeted n_{sc}, via side chain mixtures of different length, largely controls the LBL footprint on the elastic softness-firmness map. Furthermore, LBL plastomers exhibit a hierarchical telescoping deformation response that qualitatively mimics the underlying collagen fibers responsible for tissue's mechanics. Finally, additional

lessons learned regarding LBL plastomer side chain arrangements are discussed and serve as future research avenues to delineate the platform's limitations. The LBL platform has remarkable potential to couple the unprecedented elastic control demonstrated herein with additional desired properties to afford presently unrealized devices and applications.

To my parents, Mark and Suzan Keith, for their continued unconditional love and support.

To my brother, Adam Keith, who is a constant role model that inspired me down this path.

To my wife, Alissa Ward Keith, who accompanied and tolerated me on this endeavor every step of the way. I look forward to a long and happy life together.

To bind, to strive, to aid

Yours in the Double Bond

ACKNOWLEDGEMENTS

I would first like to acknowledge my advisor Sergei Sheiko who is not only a brilliant scientist and writer, but also has a wicked sense of humor. The high hopes and expectations you maintain for all of your students has forged me into a better scientist than I had dare not imagined upon starting this journey.

Second, I would like to acknowledge Mohammad Vatankhah-Varnosfaderani whose selfless labor single-handedly imparted me with a robust synthetic foundation, which I will continue to reap for years to come. Your remarkable work ethic and continued support are a true inspiration to us all.

Finally, I want to thank all of my colleagues and collaborators for their time, discussions and support, but most notably Matthew Everhart who served as my mentor that outlined a successful path to thriving in graduate school, and Erfan Dashtimoghadam whose profound professional and personal discussions has led me to become a more well-rounded scientist and better person.

TABLE OF CONTENTS

LIST OF FIGURES

LIST OF ABBREIVATIONS AND SYMBOLS

2f-BiB	ATRP difunctional initiator - ethylene bis(2-bromoisobutyrate)
AFM	Atomic force microscopy
AIBN	Azobisisobutyronitrile
ATRP	Atom transfer radical polymerization
$CDCl_3$	Deuterated chloroform
CTA	Chain transfer agent
$Đ$	Dispersity
DMA	Dynamic mechanical analysis
DP	Degree polymerization
d_1	Inter-brush distance
d_2	Physical domain size
d_3	Linear-brush periodicity
E	Structural modulus
E_0	Young's modulus
E_1	Linear modulus
E_e	Entanglement Modulus
Ebib	ATRP monofunctional initiator - Ethyl α-bromoisobutyrate
^{1}H-NMR	Proton nuclear magnetic resonance
LB	Langmuir-Blodgett technique
LBL	Linear-brush-linear
MCR-M11	Monomethacryloxypropyl-terminated PDMS, M_n=1000g/mol

MCR-M17	Monomethacryloxypropyl-terminated PDMS, M_n=5000g/mol
Me_6TREN	ATRP ligand - *tris*[2-(dimethylamino) ethyl] amine
MMA	Methyl methacrylate
M_n	Number average molecular weight
M_w	Weight average molecular weight
n_{bb}	Degree polymerization of a brush backbone
n_c	Degree polymerization of brush cores
n_e	Degree polymerization of polymer entanglements
n_g	Grafting density of side chains
n_L	Degree polymerization of linear blocks
n_r	Number of elastic repeat units in graft copolymer brushes
n_s	Degree polymerization of brush strands
n_{sc}	Number average degree polymerization of a side chain
$n_{sc,n}$	Number average degree polymerization of a side chain
$n_{sc,w}$	Weighted average degree polymerization of a side chain
n_x	Degree polymerization between covalent cross-links
PCL	Poly(caprolactone)
PDMS	Poly(dimethylsiloxane)
PMMA	Poly(methyl methacrylate)
Q	Linear block aggregation number
Q_s	Solvent fraction
$\langle {R_{in}}^2 \rangle$	Mean square end-to-end distance

RAFT	Reversible addition fragmentation chain-transfer
ROMP	Ring opening metathesis polymerization
ROP	Ring opening polymerization
R_{max}	Poly chain contour length
T_g	Glass transition temperature
THF	Tetrahydrofuran
T_m	Melting temperature
USAXS	Ultra-small angle X-ray scattering
β	Strain stiffening or firmness parameter
δ	Solubility parameter
λ	Elongation ratio
λ_{fit}	Elongation ratio fitting
λ_{max}	Maximum elongation ratio or extensibility
σ_{max}	Maximum true stress or strength
σ_{true}	True stress
$\partial\sigma_{true}/\partial\lambda$	Differential modulus

CHAPTER 1

THE PURSUIT OF NATURE: INSPIRATIONS FROM TISSUE

1.1 Introduction

Biological tissues are an extraordinary class of materials with a unique set of mechanical properties. Although this is fairly self-evident, it is a valuable exercise to appreciate tissue's mechanics with our own two hands by simply stretching and releasing the skin on the forearm. Outside of the pain likely felt, a few observations can be made. First, skin is initially relatively soft to touch compared to the hard materials we interact with in everyday life. Second, skin becomes increasingly difficult to stretch as it adaptively increases its stiffness with further deformation. Third, skin has incredible strength akin to hard rigid plastics. Finally, skin is resilient and quickly snaps back to its initial state upon release. These observations embody Nature's key mechanical defense mechanism, which both prevents accidental tissue rupture while maintaining seamless interaction with the environment and serves as a benchmark for various industrial and biomedical applications. Specifically, mimicking tissue's mechanical properties is of significant interest for use in topical adhesives, implantable and injectable devices and fillers, tissue scaffolds or replacements, and even in future soft robots (**Figure 1.1**). Therefore, mastering and encoding these mechanical features into synthetic systems is paramount, but first it is essential to understand how Nature accomplishes these incredible feats in order to inspire synthetic design.

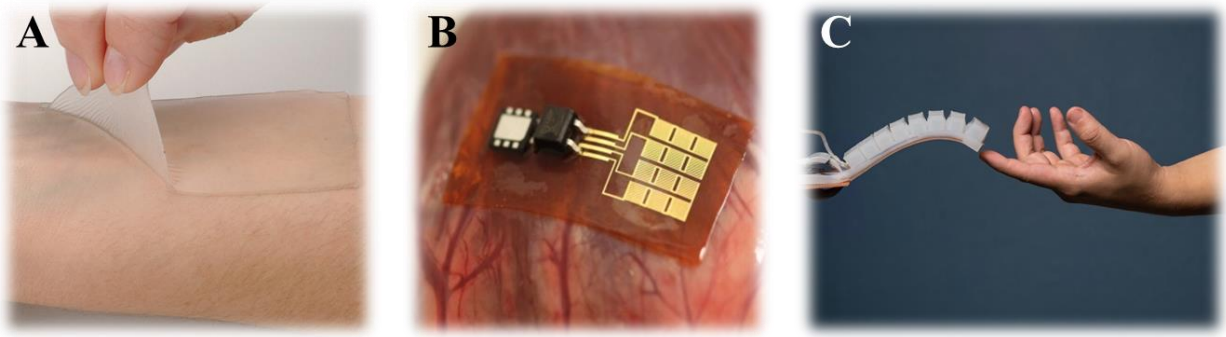

Figure 1.1: Examples of applications requiring tissue-like materials. (A) Topical adhesives. **(B)** Implantable devices.[1] **(C)** Soft robotics.[2]

1.2 Tissue Structure and Resulting Mechanics

As demonstrated by the aforementioned skin stretching experiment (**Section 1.1**), soft tissues possess a distinct oxymoronic mechanical property combination: they are compliant at touch, yet resistant to deformation. With an initial slope or *Young's modulus* (E_0) ranging from 10^3-10^7 Pa, biological tissues rapidly stiffen by a factor of 10^2-10^3× within a short interval. This can be observed in plots of *true stress* (σ_{true}), or the force response (F) over the changing cross-sectional area (A), produced by an applied *strain* (ε), or as interchangeably used in this dissertation, the *elongation ratio* ($\lambda = \varepsilon + 1 = L/L_0$) where the sample is deformed from its initial size L_0 to length L (**Figure 1.2A**).[3-6] Tissue's non-linear stress increase, or *strain-stiffening*, holds true until an observed shift where tissue stress linearly scales with strain, known respectively in tissue literature as the *elastic* and *yielding* regimes.[5,6] As the name suggests, stretching and releasing within the elastic regime leads to a completely recoverable and reversible process irrespective of strain rate. In contrast, literature sources often characterize the yielding phase by the slope of true stress linearity (E_1) until material rupture,[5,6] which exhibits both a hysteresis upon release and a strain-rate dependent stress response (**Chapter 7**). This regime transition may be explicitly observed by plotting the rate of stress change or the

differential modulus ($\partial\sigma_{true}/\partial\lambda$) (**Figure 1.2B**), which highlights tissue's characteristic sigmoidal S-shape curve. Both the elastic regime's Young's Modulus (E_0) and yielding regime's linear modulus (E_1) can be clearly identified to assist in comparing different tissue, however, a keen observer would realize these descriptors do not capture the shape of the stress-strain curve as addressed in **Chapter 2** and demonstrated in **Chapter 3**.

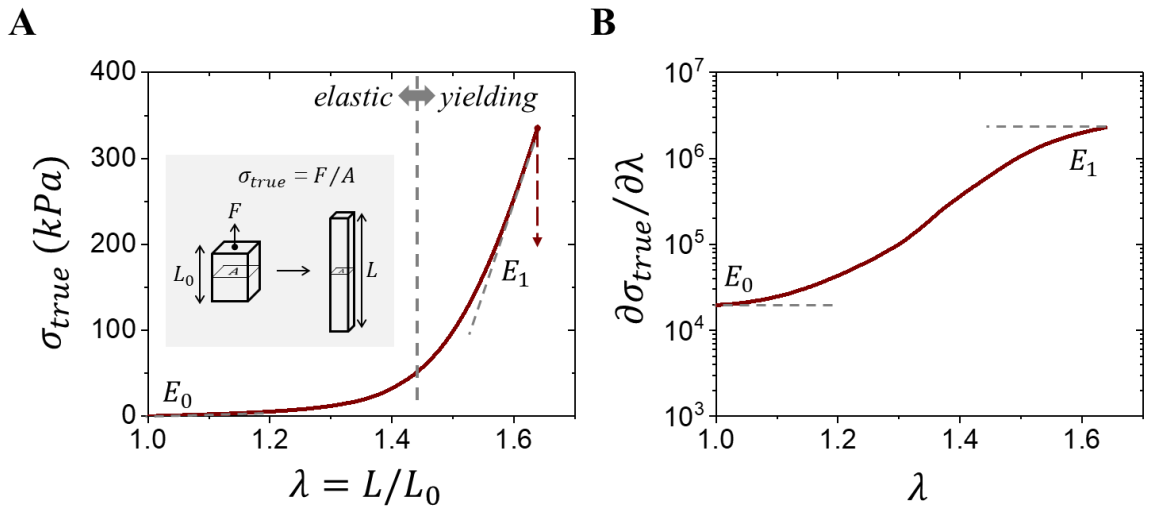

Figure 1.2: Representative deformation response of tissues. (A) A representative stress-strain curve of a fetal membrane[7] displaying an initial non-linear elastic regime and subsequent linear yielding regime, which is respectively characterized in the literature by the Young's Modulus (E_0) and Linear modulus (E_1). **(B)** A corresponding differential modulus ($\partial\sigma_{true}/\partial\lambda$) plot shows tissue's characteristic sigmoidal S-shape curve, which highlights E_0 and E_1.

Tissue's distinct mechanics arises from their composite nature of various proteins such as collagen and elastin;[8,9] however, in order to extract an elementary understanding of how tissue's structure influences mechanics, specific focus can be applied to Type 1 Collagen (**Figure 1.3**), which accounts for a plurality of the bioproteins found in animals.[9] Type I Collagen, like all of Nature, has a complex hierarchical structure with order and function at every length scale (**Figure 1.3**).[9,10] The base mechanical unit, tropocollagen, is comprised of three procollagen protein strands primarily consisting of a hydroxyproline-glycine-proline trimer that coils into a

triple helix held together by intramolecular hydrogen bonding (**Figure 1.3A**). The tropocollagen base unit then self-assembles into collagen microfibrils, which consist of five staggered and spiraled tropocollagen units. Lysine residues provide covalent crosslinking both within microfibrils and with neighboring microfibrils to provide stability to the overarching structure. Assemblies of these collagen microfibrils then go on to align into variously sized macroscopic collagen fibers oriented in tissue.

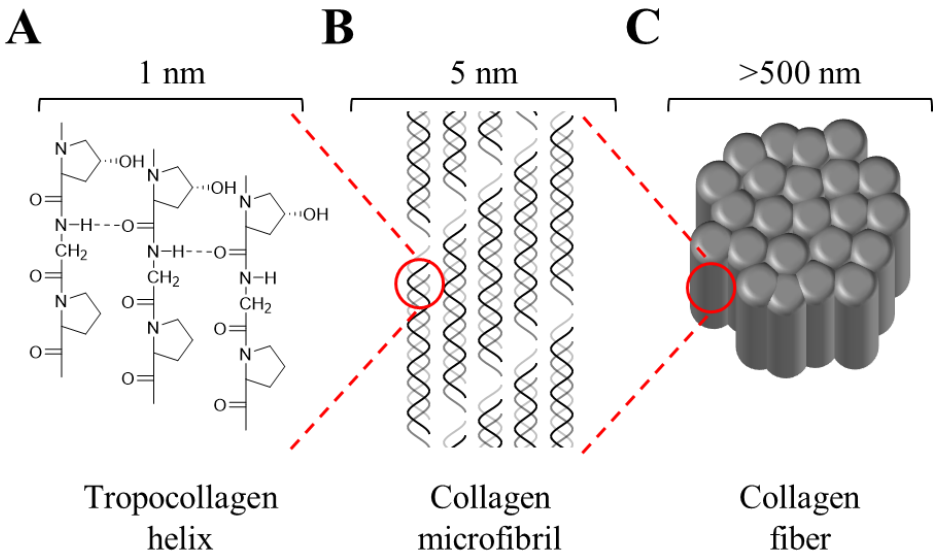

Figure 1.3: Hierarchical structure of Collagen I. Collagen I is ordered at many different length scales: **(A)** Single protein strands made primarily of hydroxyproline-glycine-proline trimers coil into a tropocollagen helix serving as the base mechanical unit of collagen macrostructure. **(B)** Individual tropocollagen self-assemble into collagen microfibrils via five staggered tropocollagen units in a cross-sectional area wrapped around each other like rope. Latent lysine units dispersed though tropocollagen strands chemically crosslink with neighboring tropocollagen helices. **(C)** Collagen microfibrils orient into individual fibers of different lengths also covalently crosslinked by lysine residues. These oriented bundles form the underlying structure of various tissues found throughout the body.

This remarkable hierarchical structure and order not only serves as inspiration to material scientists, but also empowers tissue's hierarchical deformation response, which can be largely attributed to tropocollagen deformation inside collagen microfibrils (**Figure 1.4**).[11] In an

undeformed state at rest, the five wrapped tropocollagen in the microfibrils imperfectly self-assemble from both misalignments and kinks in individual tropocollagen helices (*Stage I*). Upon deformation, the misalignment is easily corrected with minimal forces imparting tissue's softness (*Stage II*). After this adjustment has occurred, further extension causes the wrapped microfibril structure to uncoil and unravel as each individual rigid tropocollagen are stretched, which imparts the observed sharp strain-stiffening response (*Stage III*). Importantly, these three events represent purely elastic processes and with the release of strain will reversibly recover. When deformation forces become sufficiently large, the tropocollagen self-assembly breaks and strained tropocollagen units will begin sliding past each other, thus providing a linear yielding response (*Stage IV*). However, sliding eventually becomes impeded by the lysine covalent cross-links that break and lead to tissue rupture (*Stage V*).

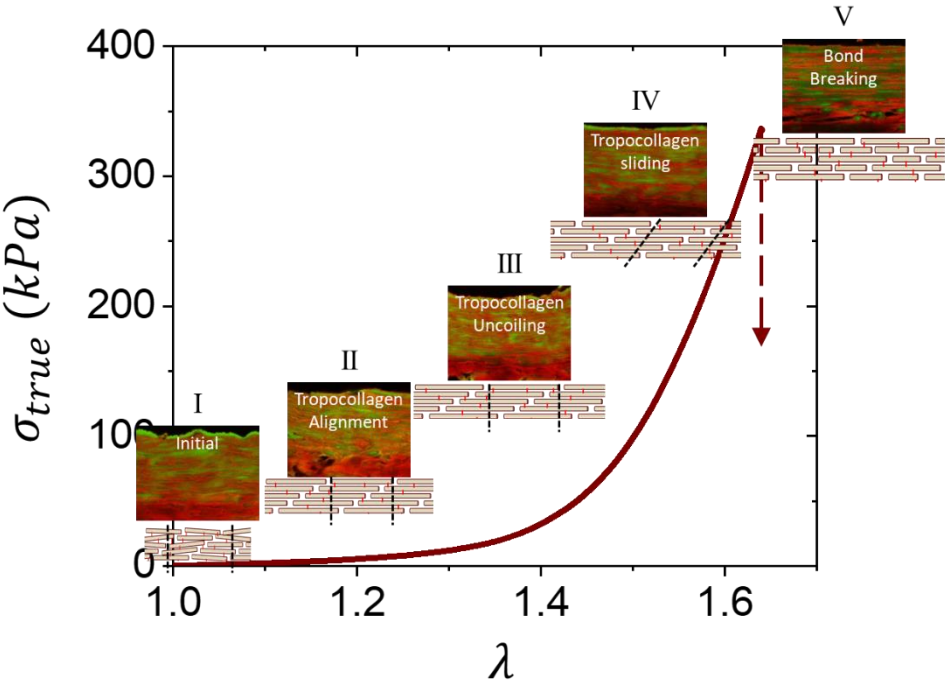

Figure 1.4: Tissue's sequential hierarchical deformation. Stress-strain response of Fetal Membrane tissue[7] with confocal microscopy images of a representative tissue[12] that maps strand stress during deformation that serves as a representation of the collagen microfibril structure

response. Different mechanisms operate and activate at different stresses via either an elastic (*Stage I-III*) or yielding (*Stage IV,V*) process: (*I*) undeformed state where tropocollagen microfibrils are imperfectly coiled and contain misaligned kinks; (*II*) deformation straightens these kinks as tropocollagen helices align; (*III*) tropocollagen helices uncoil and begin stretching; (*IV*) critical stresses overcome tropocollagen self-assembly and enable sliding; (*V*) sliding continues until lysine chemical cross-links reach a maximum stress and results in either cross-link cleavage or rupturing tropocollagen strands inside the helix.

1.3 Summary and Outline

In summary, tissue's remarkable hierarchical structure empowers a unique and unprecedented set of mechanical properties coveted by material scientists for use in future applications. Specifically, tissues possess a nearly identical chemical composition and water fraction, yet exhibit a broad range of mechanical properties (i.e. $E_0 = 10^3$-10^7 Pa), which highlights the importance of tissue's underlying architecture. Therefore, inspired by these natural occurring materials, future material design should look to architecture in order to enable novel material properties such as the synthetic mimicking of tissue mechanics itself. It is imperative to emphasize that the discussion presented in this chapter and dissertation does not serve as a comprehensive study on the complex structure and facets of tissue, which is best left to qualified biologists in the field.[5-12] Rather, this chapter serves as a primer to the field of polymer materials and their mechanical properties. In the following chapters, this dissertation draws inspiration from biology's structure and mechanics to develop a platform that can traverse the entire elastic landscape by producing synthetic materials with unprecedented mechanical properties. Topics of discussion include: theoretical considerations regarding material elasticity (**Chapter 2**), elastic characterization of various material classes (**Chapter 3**), a brief state-of-the-art review of synthetic strategies for the brush-like architecture (**Chapter 4**), introduction to a new brush-like polymer platform (**Chapter 5**), which enables mimicking tissues elasticity and coverage of the

entire elastic landscape (**Chapter 6**), and qualitatively mimics tissue's hierarchical deformation mechanisms (**Chapter 7**), with additional lessons learned regarding brush side chain arrangement (**Chapter 8**), and finally, future endeavors and concluding remarks (**Chapter 9**).

CHAPTER 2

THE ELASTIC LANDSCAPE: THEORETICAL INSIGHTS

2.1 Decoupling Softness and Firmness

A material's strain-stiffening character, as introduced in **Chapter 1,** can be simplified as its ability to resist deformation. This description could also be also associated with a material's initial softness or stiffness, however, as discussed in **Chapter 1**, the initial feeling of a material and its subsequent deformation response are two distinct concepts. Some literature[13-15] and industrial[16,17] sources recognize this distinction and aim to classify the resistance to deformation of various foods,[14,16] mattresses,[17] and our very own tissue[15] (**Figure 2.1**) as *firmness*.

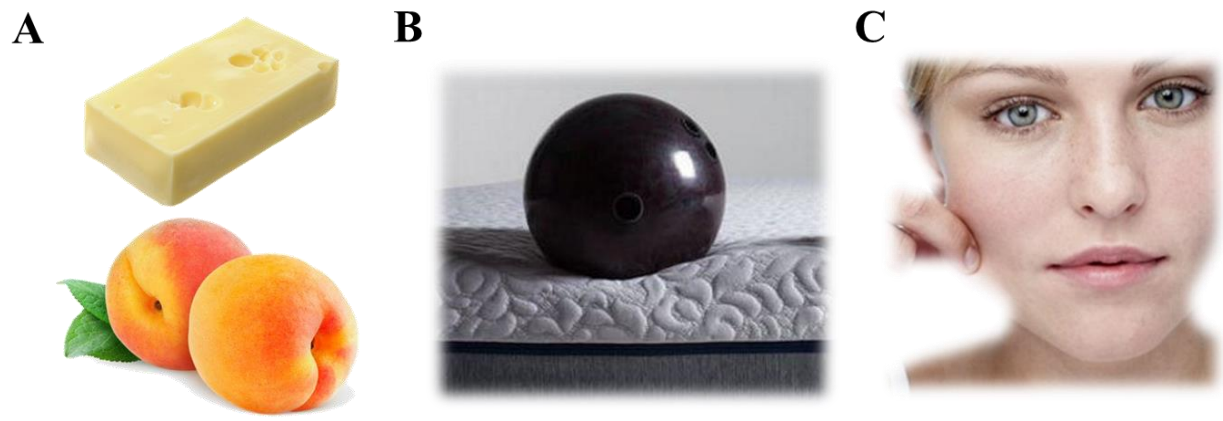

Figure 2.1: Colloquial examples using firmness. Firmness is used to describe **(A)** various food products including fruits and cheeses, **(B)** mattresses, and **(C)** tissues including skin.

To the native English speaker, this assigned name will likely cause confusion as colloquial usage suggests firmness is on the same scale as softness or stiffness by only differing

in magnitude, yet *firmness is not softness*. Although these sources[13-17] correctly identify this distinction, they typically define firmness as the measured stress at a standard strain (i.e. 10%),[15-17] but this single point value provides some ambiguity (**Figure 2.2**). For instance, theoretical cases exist where two distinct materials with different initial slopes and different intensities of their strain-stiffening curvature may achieve identical firmness (**Figure 2.2C**). Furthermore, simply redefining the strain standard will deliver different firmness values. Therefore, the current description for firmness is neither robust nor complete, but two key features can be identified: (i) softness and firmness are distinct concepts, and (ii) firmness is related to the intensity of a material's strain-stiffening curvature.

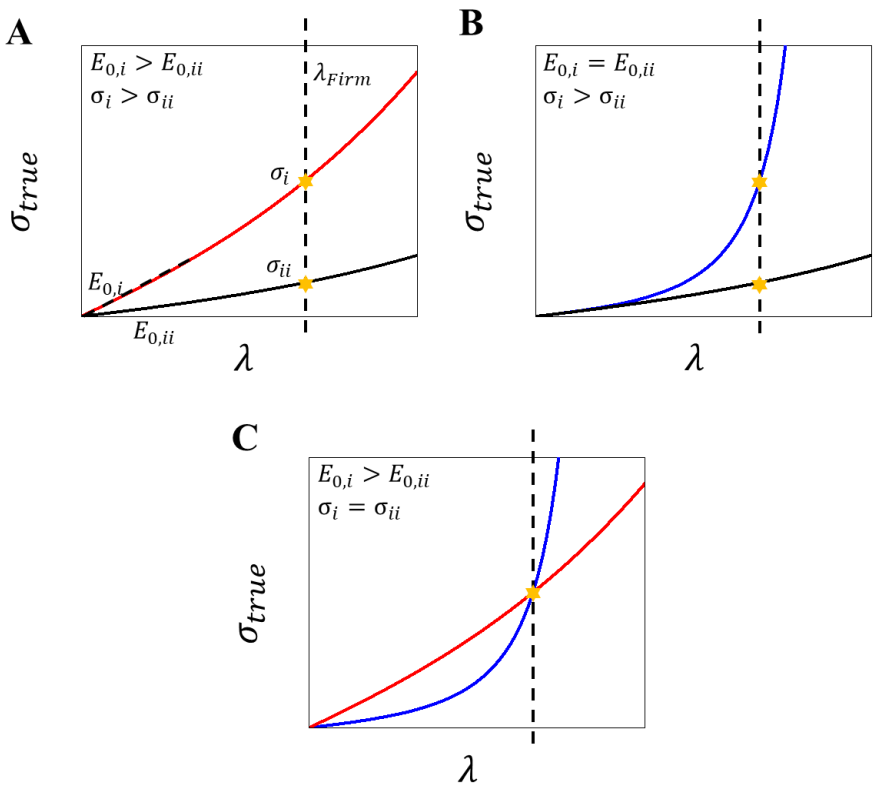

Figure 2.2: Literature defined firmness in theoretical stress-strain curves. Ambiguity of firmness as defined in the literature[13-15] and industry[16,17] by a single point stress-strain couple (σ, λ) is highlighted in three cases. **(A)** Two materials with different Young's modulus ($E_{0,i} > E_{0,ii}$) and similar curvatures have distinct firmness ($\sigma_i > \sigma_{ii}$). **(B)** Two materials with similar Young's modulus ($E_{0,i} = E_{0,ii}$) and different curvatures have distinct firmness ($\sigma_i > \sigma_{ii}$). **(C)**

Two materials with both different Young's modulus ($E_{0,i} > E_{0,ii}$) and curvatures have identical firmness ($\sigma_i = \sigma_{ii}$) according to the single point definition.

2.2 Redefining Firmness via an Elastic Model

In order to better quantify and compare different materials and material classes it is imperative to identify a theoretical model that precisely describes the entire stress-strain curvature and not simply as a single point value (**Figure 2.2**). Such a model will instruct intelligent and programmable design of desired stresses at various given strains in future materials. Fortunately, theoreticians have developed an equation of state relating true stress σ_{true} with sample elongation ratio λ as shown in equation 2.1. [18,19]

$$\sigma_{true} = \frac{E}{9}(\lambda^2 - \lambda^{-1})\left(1 + 2\left(1 - \beta\frac{(\lambda^2 + 2\lambda^{-1})}{3}\right)^{-2}\right) \qquad 2.1$$

This model describes the non-linear elastic response as a function of two molecular parameters: structural modulus E and strain-stiffening parameter β. Avoiding the complexities surrounding the inception of both these parameters and equation 2.1, which has been thoroughly discussed elsewhere,[18,19] these two parameters have real molecular origin that can be associated with specific network features (**Figure 2.3**) unlike other models.[5,20-23] The structural modulus (E) is related to the configuration of network's mesh size or the density of stress supporting strands (${n_x}^{-1}$) (**Figure 2.3A**). The strain-stiffening parameter (β) is related to the conformation of individual strands, or the initial undeformed strand conformation $\langle {R_{in}}^2 \rangle$ in relation to its fully extended contour length R_{max} (**Figure 2.3B**), such that $0 < \beta = \langle {R_{in}}^2 \rangle / {R_{max}}^2 < 1$. The β parameter is thus intimately related to elastic material's extensibility as $\beta = {\lambda_{max}}^{-0.5}$, where rigid and nearly fully extended network strands (${R_{max}}^2 \sim \langle {R_{in}}^2 \rangle,\ \beta \to 1$) form inextensible and

brittle materials. This particular equation ignores the presence of trapped entanglements within the network, which may be accounted for with an additional fitting parameter,[18] and is a concept discussed later (**Section 3.3**).

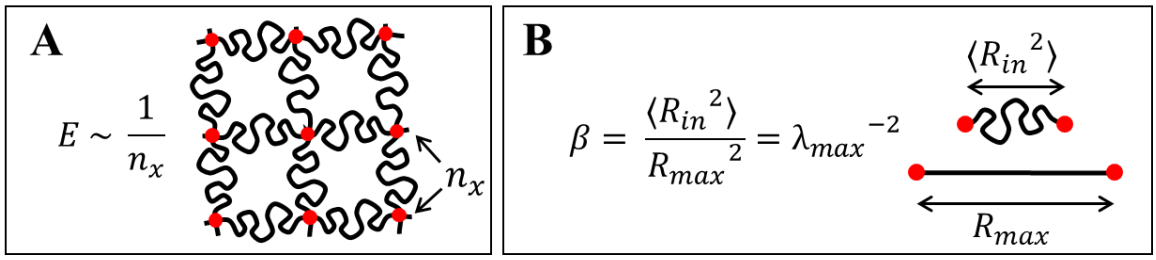

Figure 2.3: Physical origins of elastic parameters. (A) Structural modulus (E) is classically related to the density of the material mesh size ($1/n_x$). **(B)** Strain-stiffening parameter (β) is related to the initial conformation of individual strands $\langle {R_{in}}^2 \rangle$ in relation to their contour length (R_{max}) and is thus intimately related to material extensibility (λ_{max}).

A consequence of this model is the realization that a material's Young's modulus (E_0), depends not only on the cross-linking density (E) but also on the initial strand conformation (β) as highlighted in equation 2.2.

$$E_0 = \frac{\partial \sigma_{true}}{\partial \lambda}\Big|_{\lambda \to 1} = E/3(1 + 2(1-\beta)^{-2}) \qquad 2.2$$

Taking this one step further, combining both equations 2.1 and 2.2 into equation 2.3 yields an equation of state that provides two fitting parameters with observable features in stress-strain curves: the initial slope, or *softness* (E_0), and the following strain-stiffening curvature, or *firmness* (β).

$$\sigma_{true} = \frac{E_0}{3(1 + 2(1-\beta)^{-2})}(\lambda^2 - \lambda^{-1})\left(1 + 2\left(1 - \beta\frac{(\lambda^2 + 2\lambda^{-1})}{3}\right)^{-2}\right) \qquad 2.3$$

To demonstrate the power of this elastic model, two sets of theoretical stress-strain curves have been calculated by either holding E_0 constant and varying β (**Figure 2.4A**) or vice versa

(**Figure 2.4B**). In the first case, curves display an identical initial slope as designed, but distinct curvatures and extensibilities as higher β materials show enhanced strain-stiffening and lower extensibilities. In the second case, curves display distinct initial slopes, but identical curvatures and extensibilities. These theoretical exercises delineate and validates the origins of the elastic curvature through the equation of state (equation 2.3) by eliminating the ambiguity surrounding the current usage of firmness as presented in **Figure 2.2**.

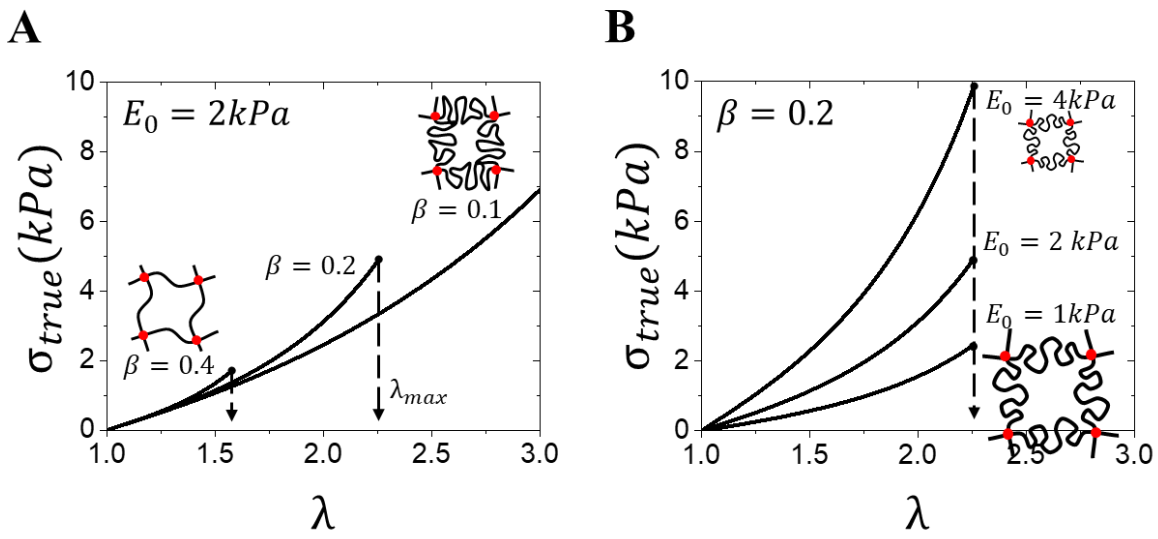

Figure 2.4: Theoretically constructed stress-strain curves. Varying fitting parameters of softness and firmness in equation 2.3 shows observable changes in theoretical stress-strain plots. **(A)** constant softness at different firmness or **(B)** different softness at constant firmness.

2.3 Conclusion and Outlook

This foundation for both the origin and mechanical characterization of polymer networks serves as a stepping stone to future intelligent material design. The elastic model both precisely characterizes a materials softness (E_0) and firmness (β), and enables cataloging different material classes to streamline comparisons of large data sets in contrast to Edisonian approaches of overlapping stress-strain response couples. Furthermore, this material informatics empowers

general material design rules and allows establishing material class boundaries on an elastic map (**Chapter 3**).

CHAPTER 3
INDEXING ELASTIC SYSTEMS: FROM TISSUE TO ELASTOMERS

3.1 Introduction

Various molecular and macroscopic constructs have endeavored to mimic the stress-strain behavior of tissue; however, most attempts rely on Edisonian approaches without questioning the validity of the underlying platform. Therefore, before proposing an approach to achieve tissue softness and firmness, it is essential to first systematically characterize the mechanical limitations and boundaries of various material classes. Using the elastic model (**Section 2.2**), tissues (**Section 3.2**) are compared with different material classes including linear elastomers (**Section 3.3**), swollen elastomers or gels (**Section 3.4**), and the relatively young field of brush-like elastomers (**Section 3.5**).

3.2 Tissues

The extreme firmness of skin as demonstrated in **Chapter 1**, is ubiquitous to all tissues across the animal kingdom regardless of bodily location and functionality including: muscles, eyes and connective tissue (**Figure 3.1A**). Application of the elastic model shows a good fit within tissue's elastic regime until yielding occurs where a clear divergence with the model is observed as expected (**Figure 3.1B**).

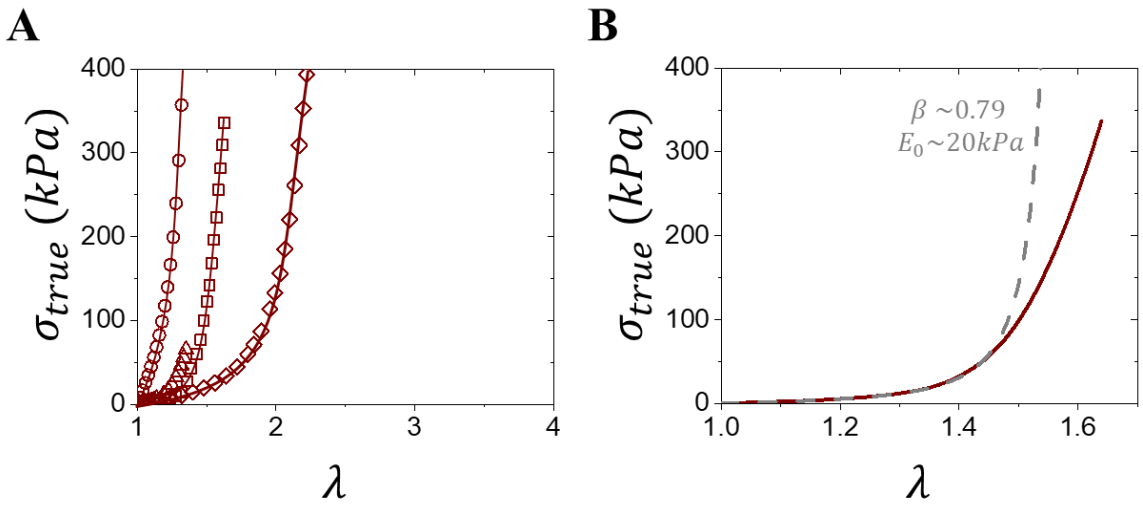

Figure 3.1: Characterizing tissue's mechanical properties. (A) Stress-strain curves of various tissues including fetal membrane (squares),[7] lens capsule (circles),[24] muscle (triangle)[25] and pig belly (diamonds).[26] Note that connecting lines only serve to guide the reader and the chosen axis window does not fully capture every tissue's stress-strain response. **(B)** Fitting of fetal membrane tissue using the elastic model to extract softness (E_0) and firmness (β). Note that the model only characterizes elasticity and thus deviates during the yielding regime.

Both of the extracted fitting parameters from an ensemble of tissues found within the literature[27] can be plotted onto an [E_0,β] map, which highlights tissue's mechanical boundaries of E_0 = 10^3-10^7 Pa and β > 0.7 (**Figure 3.2**). This realization may not at first seem that impressive, but becomes exceedingly remarkable when stacked against other material classes (**Sections 3.3-3.5**).

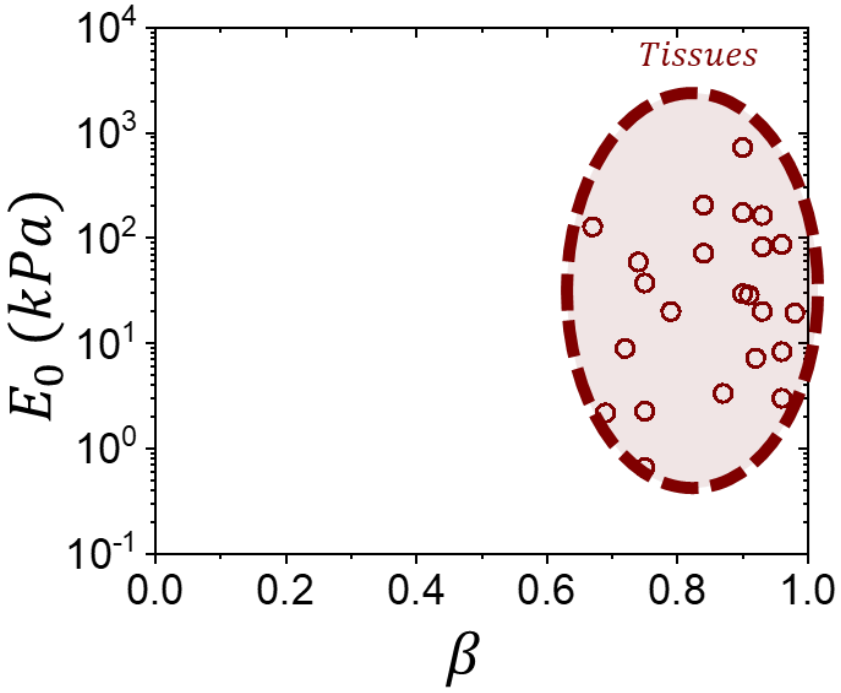

Figure 3.2: Tissues on the elastic landscape. An [E_0,β] map showing extracted elastic parameters from various tissues (red circles).[27] Most tissues show exceedingly high firmness (β > 0.7) and a wide softness range (E_0 = 10^3-10^7 Pa) revealing the tissue's elastic zone.

3.3 Linear Elastomers

Elastomer networks constructed from chemically crosslinking linear strands has been ubiquitously used in various industrial applications (e.g. tires and rubber bands) ever since Goodyear first demonstrated vulcanization of natural rubber. Since then, the field of traditional linear elastomers has exploded to encompass numerous chemistries where rubbery polymers, i.e. neither crystalline (T_m) nor glassy (T_g) solids at normal operating temperatures, are coupled with various crosslinking schemes. These include historical sulfur crosslinking of unsaturated isoprene units in natural rubber or styrene-butadiene random copolymers[28] to modern approaches such as simultaneous growth and crosslinking of poly(butyl)acrylate with small difunctional molecules[29] or strand coupling by hydrosilylation of two component silicones.[30] The last of

which comprises various commercial brand names such as Sylgard, Ecoflex and Dragon Skin that persists into novel research to date.[31,32] However, linear elastomers have an extremely narrow elastic range stemming from the lack of architectural control via their single classical network parameter of cross-linking density (n_x) (**Figure 3.3A**). This limitation leads to two distinct issues: (i) crosslinking leads to permanent trapping of inherent strand entanglements and (ii) variations in n_x lead to a coupled softness (network configuration) and firmness (strand conformation) (**Section 2.2**). The first issue is an unavoidable product of polymer physics as all polymer strands, regardless of chemistry, entangle at specific length scales (n_e).[33,34] Crosslinked elastomers naturally inherit this issue resulting in trapped entanglements that behave as topological crosslinks. Although this is a nonissue when targeting low n_x and hard networks, upon increasing n_x to theoretically access softer elastomers, these topological crosslinks begin bearing a significant portion of the network load (**Figure 3.3B**). Therefore, these preordained confinements constrain the linear elastomer platform as a lower limit softness plateau emerges, which cannot be traditionally overcome by only varying n_x. It is important to note that some literature[35,36] aims to avoid linear entanglements via cross-linking in very dilute solutions, but these approaches face steep synthetic challenges.

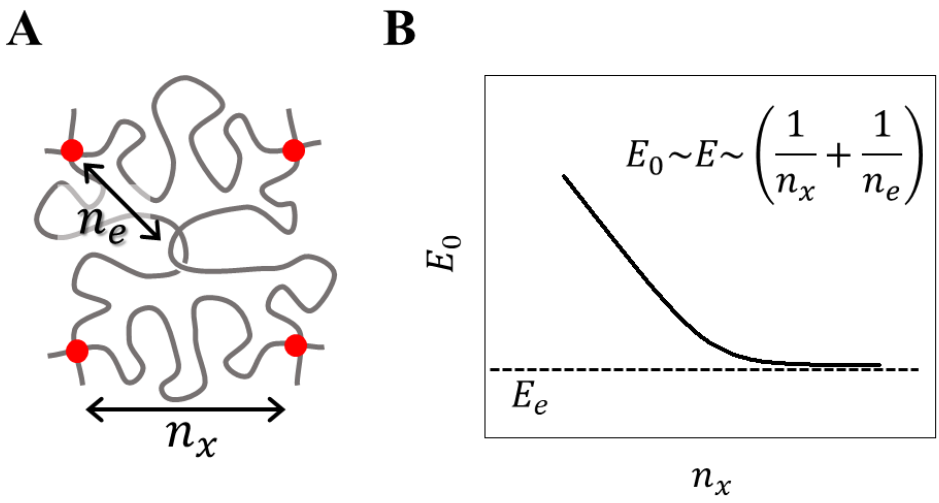

Figure 3.3: Physical limitations of linear elastomers. (A) Schematic of an elastomer network with programmable crosslinking density (n_x) and inherent chain entanglements (n_e) **(B)** Representative plot of n_x versus Young's Modulus (E_0) in linear elastomers. Although theoretical n_x can be programmed via stoichiometry of various crosslinking strategies, a softness barrier (E_e) is observed as inherent and unavoidable chain entanglements persist at large n_x and behave as topological crosslinks. Note in linear elastomers, strand firmness is negligible ($\beta \rightarrow 0$) and ($E_0 \sim E$).

The second issue arises as variations in n_x both augment the density of mechanically active strands (**Figure 2.3A**) and individual strand conformations (**Figure 2.3B**), leading to a coupling of softness and firmness. This limitation follows classical intuition that hard networks are brittle and soft networks are extensible.[34] Furthermore, attempts to increase material firmness, by shortening the network strands via lower n_x, fail to achieve significant enhancement. All of these limitations culminate in linear elastomer networks containing a narrow elastic range as evidenced by natural rubber,[18] styrene-butadiene rubber,[18] silicone[29] and butyl acrylate[29] linear elastomers (**Figure 3.4**), which are unsuitable to match tissue with both an observed softness ($E_0 > 10^5$ Pa) and firmness barrier ($\beta < 0.1$) with most failing to achieve $\beta > 0.05$.

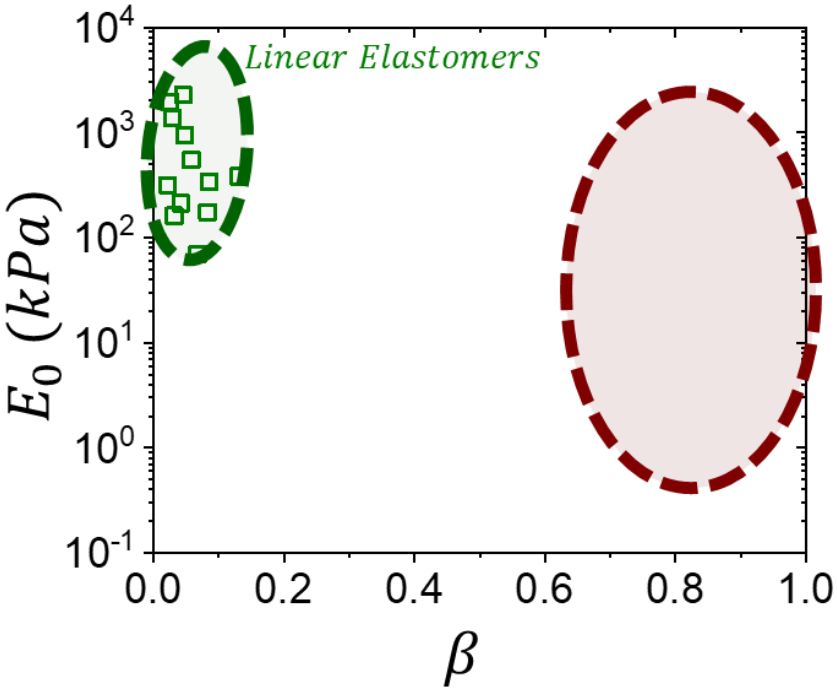

Figure 3.4: Linear elastomers on the elastic landscape. An [E_0,β] map showing linear elastomers (green squares).[18,29] Linear elastomers face a softness barrier (E_0 > 10^5) and exceedingly low firmness (β < 0.1) unsuitable for matching tissue mechanics (red).

3.4 Synthetic Gels

Linear elastomers swollen with solvent, also-known-as gels, are often touted as replicating tissue mechanics. This is partly true as some of the limitations facing linear elastomers can be addressed by the semi-independent parameter of solvent fraction (Q_s)[29] (**Figure 3.5**). Synthetic strategies for such systems are synonymous with linear elastomers as they often require solvent to facilitate crosslinking (e.g. Jell-O). In addition, elastomers crosslinked from the "dry" state (without additional solvent) may be swelled with compatible solvents to the desired swelling ratio. The presence of solvent has significant impacts on the resulting mechanical properties as it both dilutes network crosslinks towards lower E_0 and extends network strands towards higher β, which are imperative to achieve tissue mechanics. In

spite of this improvement, gels face additional mechanistic and application issues. For instance, depending on the synthetic strategy, they inherit the entanglements from their linear network precursors (**Figure 3.5**) creating materials that are both soft but also very brittle as the entanglements become highly strained.[34] Additionally, gel's solvent fraction will inevitably evaporate or leak causing unwanted mechanical property drifting over time.

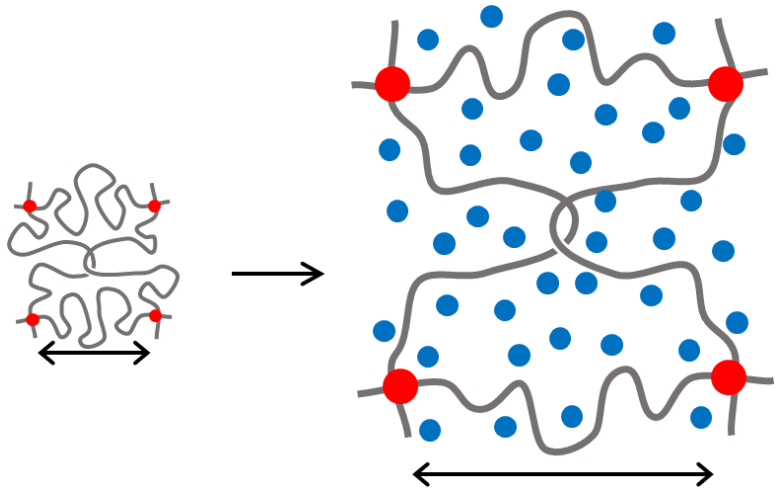

Figure 3.5: Synthetic gels: swelling linear networks. Schematic of swelling linear elastomers with solvent (blue circles), which (i) dilutes crosslinks toward lower softness and (ii) extends network strands toward higher firmness. Note that gels synthesized through linear elastomer swelling maintains the entanglements and imparts brittleness.

Nevertheless, gels represent a deep and active research field for various applications with a wider mechanical footprint (**Figure 3.6A**) than their linear network counterparts. Application of the elastic model yields good agreement over the full stress-strain curve (**Figure 3.6B**), unlike the inevitable yielding observed in tissues. Visually comparing the stress-strain curves of gels (**Figure 3.6A)** versus tissue (**Figure 3.1A**) reveals that gels successfully replicate tissue's softness, yet not tissue's firmness.

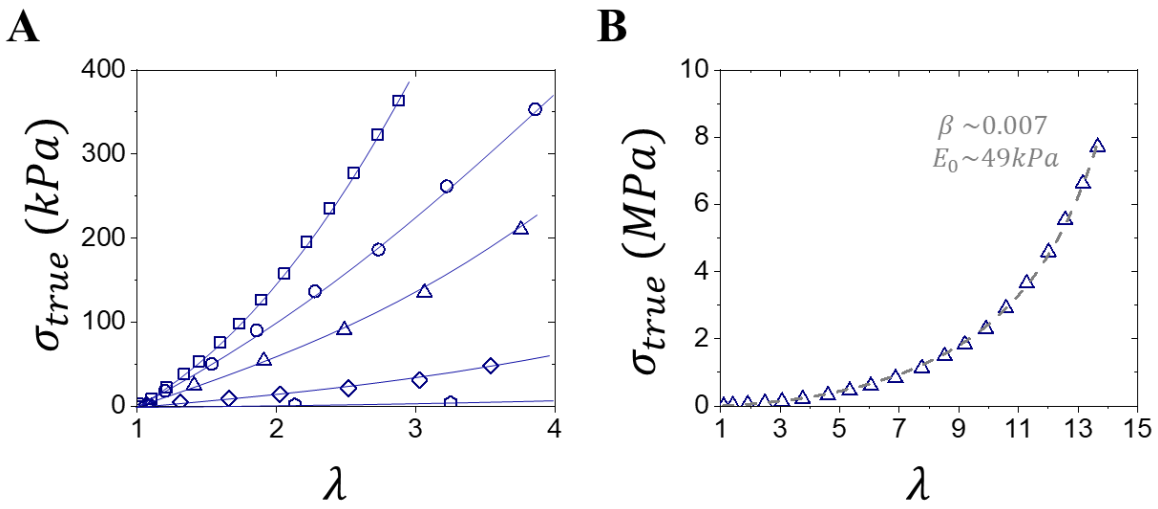

Figure 3.6: Characterizing gel's mechanical properties. (**A**) Stress-strain curves of various gels including PEDOT/PSS (squares),[37] PVA-PAAM (circles),[38] PAAM-PAAc (triangles), [39] Polyrotaxane (diamonds) [40] and a clay nanocomposite (hexagons).[41] Note that connecting lines only serve to guide the reader and the chosen axes window does not fully capture the entirety of every gel curve so as to match the window in **Figure 3.1A**. (**B**) Fitting of a PAAM-PAAc gel using the elastic model to extract softness (E_0) and firmness (β). Note that the model fits the whole range in stark contrast with tissues.

The origin of this firmness divide stems from the weak strand extension of their linear chain networks, which mostly show $\beta_{dry} \cong 0.01$, and the upper bound on their swelling ratio ($\alpha < 100$). Taking these two limitations into consideration, a theoretical gel firmness barrier can be outlined according to equation 3.1 and is approximately $\beta_{gel} < 0.2$.[27]

$$\beta_{gel} = \beta_{dry} \langle R_{in}^2 \rangle_{gel} / \langle R_{in}^2 \rangle_{dry} = \beta_{dry} \alpha^{2/3} \qquad 3.1$$

The observed firmness barrier may cause confusion as it is anticipated that network strands could conceivably swell and extend indefinitely to their extension limit $\beta \to 1$, however, a gel's maximum Q_s is a product of the balance between osmotic pressure and its swellability.[29] Therefore in summary, gel's semi-independent parameters (n_x and Q_s)[29] allows access to tissue-relevant softness and enables decoupling E_0 and β to provide limited mobility on the elastic map

within a given chemistry (**Figure 3.7**), albeit with significant firmness limitations $\beta < 0.2$.[27] This analysis does not include recent progress with more complex gel architectures such as dual network interpenetrating gels,[42] and utilizing sacrificial bonds.[43] Although, these reported systems also face similar elastic limitations ($\beta < 0.4$) and typically demonstrate high modulus due to initially high crosslink density.

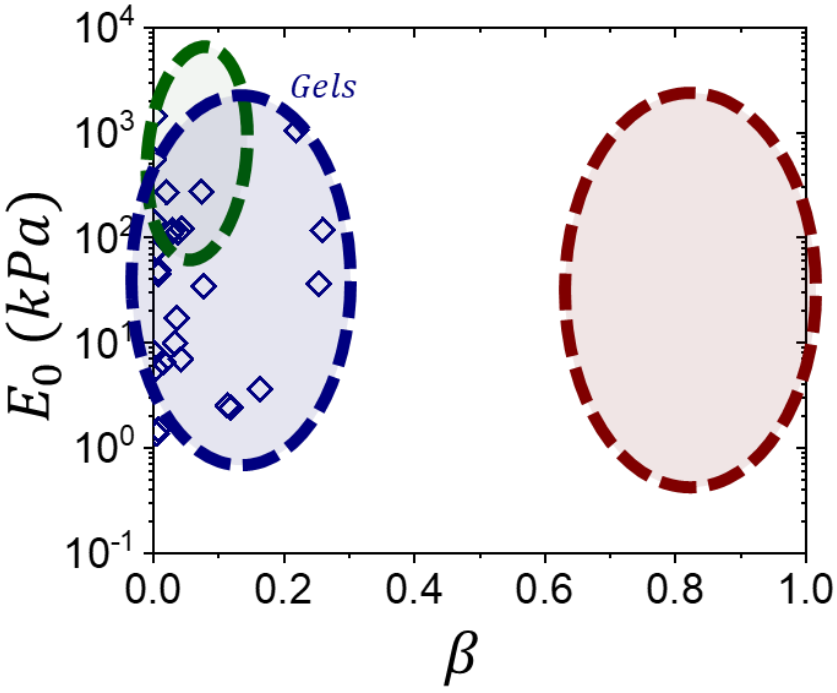

Figure 3.7: Synthetic gels on the elastic landscape. An [E_0,β] map showing extracted elastic parameters from various synthetic gels (blue diamonds).[27] Gels enable piercing linear elastomer's softness barrier with comparable softness to tissue (E_0 = 10^3 - 10^6 Pa), and enhanced firmness albeit far from replicating tissue (β < 0.2).

3.5 The Brush-like Architecture

The brush-like architecture[34,44-46] (i.e. bottlebrushes, brushes and combs), is in hindsight, an obvious iteration of both dry (**Section 3.3**) and swollen (**Section 3.4**) elastomer networks whereby side chains are chemically grafted onto network strands. Instead of containing just one

controlled architectural parameter (n_x) and limited by strand entanglements (n_e), as is the case in linear elastomers (**Figure 3.8A**), the brush architecture suppresses entanglements through the inclusion of two additional coded architectural parameters of side chain length (n_{sc}) and side chain grafting density (n_g) (**Figure 3.8B**).[34] The brush-like architecture's ability to suppress entanglements can be summarized by a simple thought experiment highlighted in **Figure 3.8C**. Let us assume linear strands become entangled on length scales outside of the black circle resulting in confinements to the mechanical properties as discussed in **Section 3.3**. Grafting side chains expands the flexible and skinny linear network strands into larger cylindrical and rigid filaments, thereby changing the requirements for strand entanglement shown by a new red circle. Therefore, a wide range of crosslinking densities (n_x) become available at length scales between the black and red circles as brush strands are not entangled. An elegant analogy can be found in the world of cooked pasta (**Figure 3.8D**) where flexible and skinny spaghetti (i.e. linear strands) notoriously entangle into a ball like mass in contrast to rigid cylindrical penne (i.e. brush-like strands) that easily slide and flow past each other. While this is an imperfect analogy as penne pasta are crafted to be relatively short (**Figure 3.8D**), it can be easily imagined that the length requirements to entangle penne are much larger than that of spaghetti. It is important to reiterate that the brush-like architecture does not eliminate entanglements, but simply expands their criteria such that they are nonexistent on any practical scale of application.

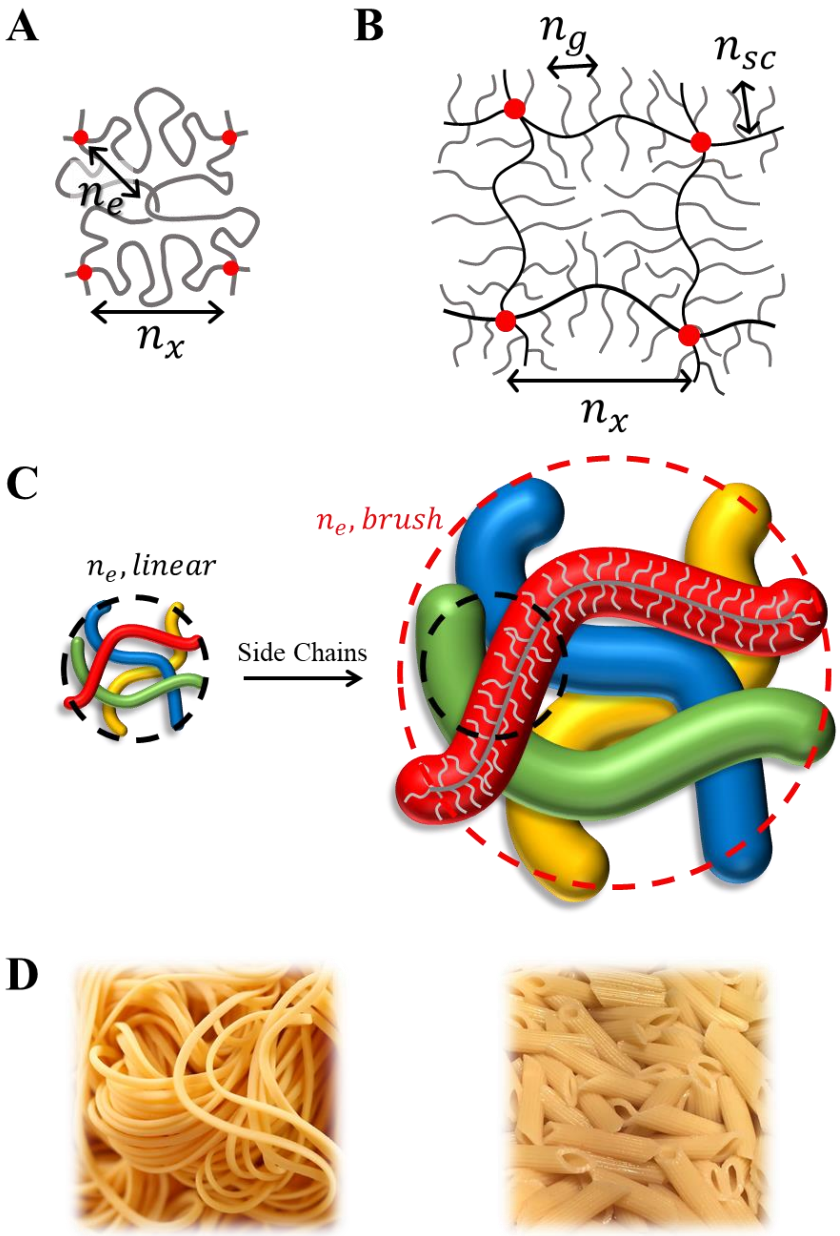

Figure 3.8: The brush effect. Structural differences between **(A)** Linear networks and **(B)** brush-like networks. Linear networks are programmed via network crosslinking density (n_x), but face inherent entanglements (n_e). Brushes contain two additional programmable features: side chain length (n_{sc}) and side chain grafting density (n_g). (**C**) On similar length scales of linear entanglements (black circle), brush strands are disentangled as added side chains increase the requirements for entanglement (red circle) (**D**) A cooked pasta analogy where linear polymers behave similar to spaghetti, which often entangle into a ball like mass, while brush polymers behave similar to penne pasta, which easily slide past each other.

Therefore, the consequences of the brush architecture are two-fold: (i) the removal of the linear network entanglement barrier provides access to tissue-relevant softness, and (ii) grafted side chains behave analogously to solvent found in gels (**Section 3.4**). This second realization has important implications as side chains play a dual oxymoronic role to both dilute crosslinks towards tissue-relevant softness and extend network strands via side chain steric repulsion towards enhanced strand rigidity or firmness without the use of solvent. Furthermore, the independent nature of the brush-like architectural triplet (n_x, n_{sc}, n_g) can be exploited to achieve fine-tuning of both softness and firmness independently.[45,46] This was demonstrated by a model system utilizing a copolymer mixture of methacrylate end functionalized polydimethylsiloxane (PDMS) macromonomer with well-defined n_{sc}, a butyl acrylate monomer spacer and difunctional PDMS crosslinker in specified ratios via free radical polymerization to achieve various n_g and n_x.[45,46] For instance, softness may be held constant while tuning firmness analogous to theoretical curves in **Figure 2.4A**, via simultaneous increases of n_x and n_g (**Figure 3.9A**). This occurs as the strand mass between crosslinks is held constant while the strand rigidity is adjusted. Similarly, firmness may be held constant while tuning softness analogous to theoretical curves in **Figure 2.4B**, via counterbalancing n_x and n_g (**Figure 3.9B**). Here the strand mass between crosslinks is adjusted while the strand rigidity is held relatively constant. It is important to note that n_{sc} and n_g are semi-related parameters that achieve similar effects.

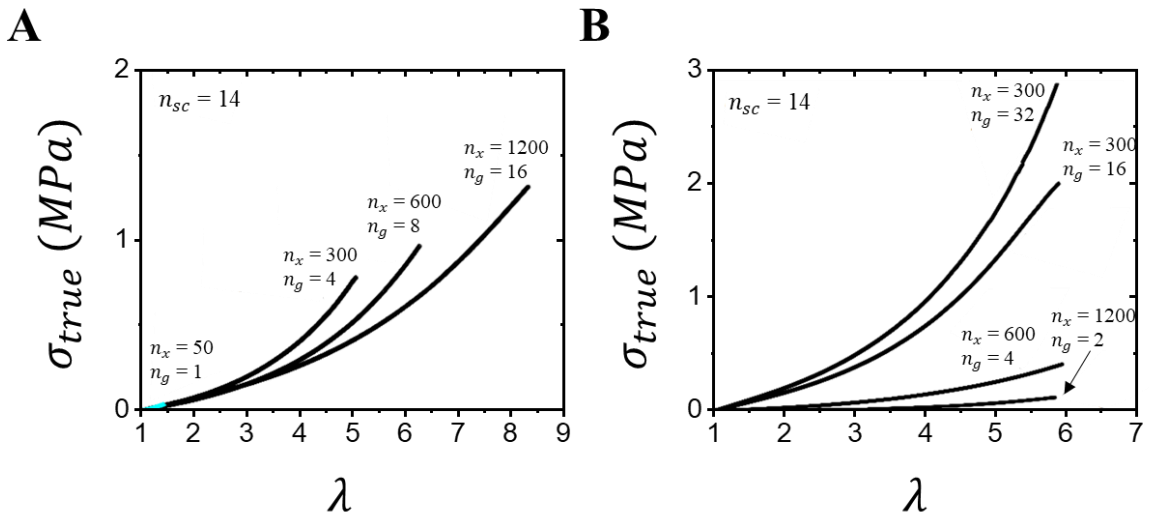

Figure 3.9: Stress-strain responses of brush-like elastomers. Programming brush-like elastomers to have either **(A)** The same softness (E_0) by fixing the strand mass via simultaneously increasing n_x and n_g, and **(B)** the same firmness (β) and extensibility by fixing the strand rigidity via counterbalancing n_x and n_g.

In summary, the brush-like architecture empowers an elegant platform for unprecedented control over softness and firmness independently, while also paving a solvent-free pathway to mimic the mechanical properties of gels (**Figure 3.10**). This addresses many of the practical limitations of gels as these materials do not leak or evaporate and are mechanically invariant over time. Unfortunately, like gels, they face severe limitations in the achieved firmness ($\beta <$ 0.3) as theoretical architectural combinations (n_x, n_{sc}, n_g) to attain tissue-like firmness are synthetically unfeasible.[45]

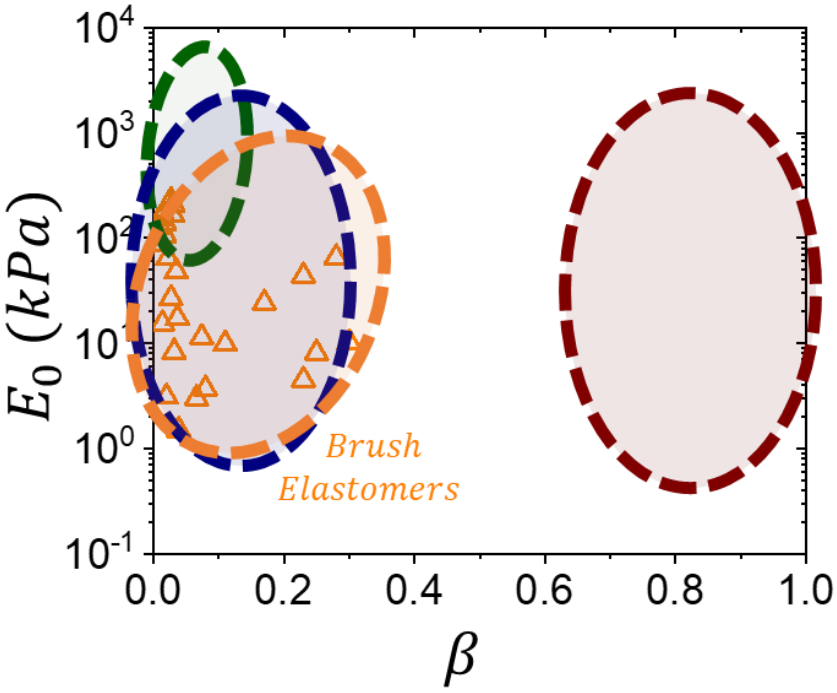

Figure 3.10: Brush-like elastomers on the elastic landscape. An [E_0,β] map showing extracted elastic parameters from various brush-like elastomers (orange triangles).[45.46] Brush elastomers enable programmable solvent-free mimicking of gels thus providing comparable softness to tissue (E_0 = 10^3 - 10^6 Pa), but still far from replicating tissue firmness (β < 0.3).

3.6 Conclusion and Outlook

In an effort to characterize different elastic material classes (**Section 3.3-3.5**), it has become clear that no current *synthetic* platform has attained both tissue softness and firmness (**Section 3.2**). Additionally, **Figure 3.11** also illuminates a large unpopulated firmness void (0.3 < β < 0.7) suggesting that no *single* platform has access to the entire elastic landscape, not even tissue. Therefore, the goals are two-fold: (i) design a material platform to provide access to the tissue elastic zone and mimic select tissue, which (ii) can also extend over the entire elastic landscape to provide synthetic materials with unprecedented combinations of softness and

firmness. Despite the highlighted limitations, brush-like networks emerges as the most promising avenue given the elegant nature of the architecture's programmable design.

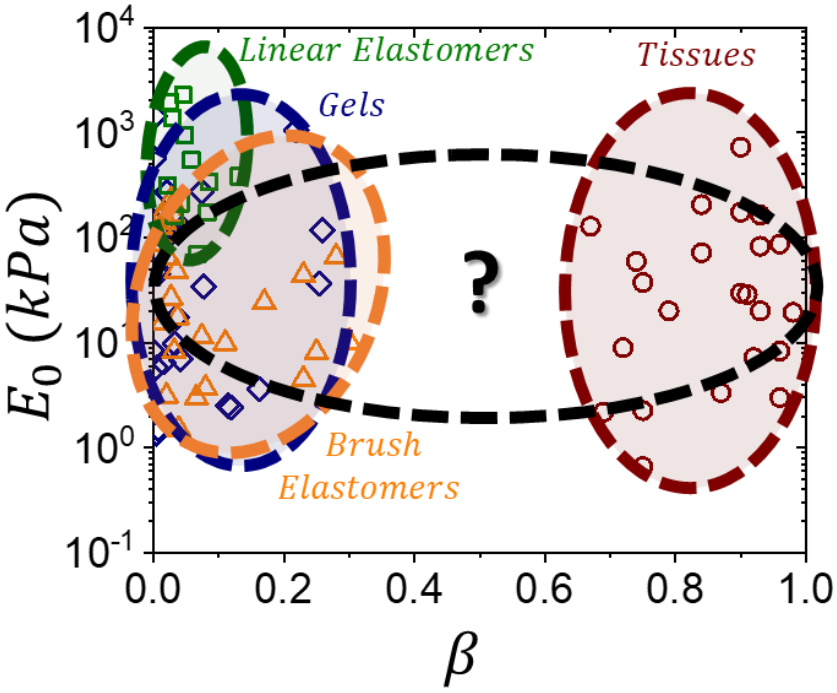

Figure 3.11: Populations of the elastic landscape. An $[E_0,\beta]$ map showing all classes of elastic materials tissue (red circles), linear elastomers (green squares), gels (blue diamonds) and brush-like elastomers (orange triangles). No synthetic platform has achieved tissue softness and firmness while no single platform has achieved broad control over softness and firmness.

CHAPTER 4

SYNTHETIC STRATEGIES FOR THE BRUSH ARCHITECTURE

4.1 Introduction

As the mechanical implications of the brush architecture are clearly outlined in **Section 3.5**, it is essential to speak briefly on the state-of-the-art of brush synthesis. Extensive literature reviews[47-49] have already explored the different pathways to synthesize brushes with distinct chemistries and for various applications, yet it is imperative to ground the discussion within the goal of this dissertation. To this end, the limited elastic control of the chemically crosslinked brush elastomers described in **Section 3.5** also has significant synthetic limitations that excludes careful characterization of the brush architectural parameters. Therefore, this chapter aims to refocus the discussion on a bottom up approach by first crafting well defined brushes that may then form materials to coverthe entire elastic landscape (**Chapter 5,6)**.

4.2 A Brush Synthetic Strategies

Readers immersed in the polymer brush field will recognize three distinct approaches towards the brush architecture (**Figure 4.1**): (i) grafting-to, (ii) grafting-from and (iii) grafting through.[47-49]

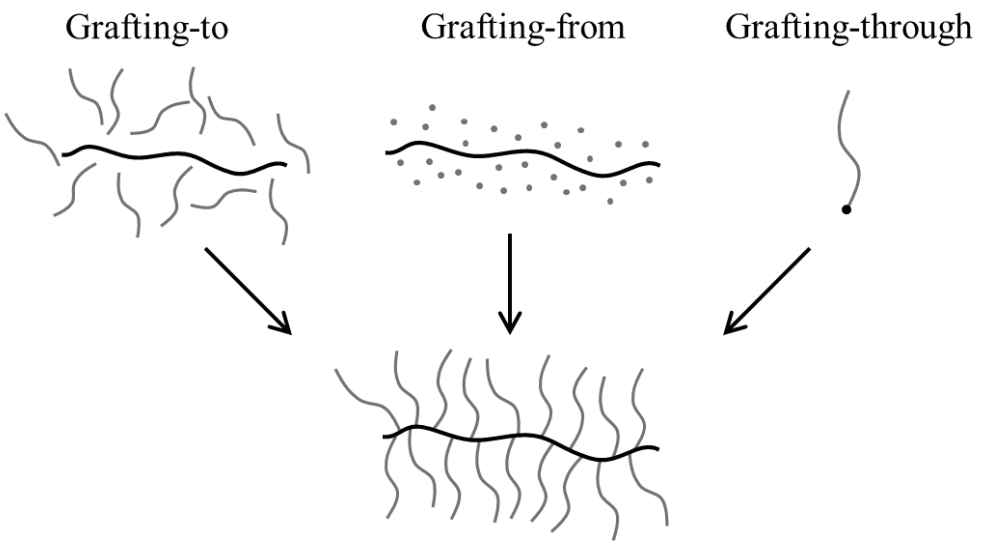

Figure 4.1: Different pathways to brushes. Grafting well defined side chains to brush backbone strands (left), growing side chains from brush backbones (middle) and grafting through end functionalized group of side chains.

The grafting-to technique utilizes well defined end functionalized polymer side chains that contain complementary chemistries with functional groups on polymer strand backbones (**Figure 4.1**). In this approach, both the side chains and polymer backbones may be fully characterized and synthesized separately. Such grafting-to chemistries typically include highly efficient "click" reactions such as Diels-Alder[50] and azide-alkyne coupling.[51] This method is strongest for low grafting densities ($n_g \gg 1$) as immiscibility between polymer side chains and backbones of different chemistries, and side chain steric hindrance precludes this method from achieving high degrees of grafting density. Grafting-from similarly utilizes a polymer strand backbone with functional groups that enable sequential growth of added monomers into side chains. This approach faces less immiscibility issues; however, careful measurement of brush side chain dispersity and grafting density is difficult to achieve. It is especially challenging to synthesize dense and homogenous side chains as the first initiated backbone sites bury and

suppress growth of shorter side chains that initiated later. Lastly, grafting-through utilizes polymer side chains with an end functionalized group that may be sequentially polymerized into well-defined brushes. This method often faces slow reaction times due to both the dilution of the functional end group and steric hindrance at the growing backbone end. Additionally, the most limiting feature is the challenge of purifying residual unreacted macromonomers from the brush mixtures, a similar problem faced in the grafting-to approach.

Although each method has its niche uses, the grafting-through approach is the most relevant to seamlessly ensure densely grafted brush materials that can then enable traversing the elastic map. Indeed, brush elastomers reported in **Section 3.5** utilize this single step approach to encode different polymerized mixtures of macromonomers, spacers and cross-linkers into network strands of the elastomer. In comparison, both the grafting-to and grafting-from approaches requires two steps of respective side chain coupling or polymerization after first crosslinking network strands. Furthermore, it is difficult to ensure homogenous functionalization over each network strand deep inside elastomer films. Similarly, grafting-through via free radical polymerization highlighted in **Section 3.5** may also lead to network strand inhomogeneity due to uncontrolled radical termination, coupling, and chain transfer or due to a difference in reactivity ratios between monomer spacers, and the diluted functional end groups of long macromonomers and crosslinkers. These consequences are impossible to characterize with typical analytical techniques due to the chemically crosslinked nature of the elastomer, and can only be explored via the resulting mechanical behavior. Therefore, it is imperative to build a platform from a brush first approach that can be easily characterized and tuned to enable a broader scope of mechanical properties.

Various controlled polymerization schemes have been implemented to graft-through well-tailored brushes, however, few have emerged as effective strategies with wide chemical applicability and high degree of control. Premier examples include ring opening metathesis polymerization (ROMP),[52] reversible addition-fragmentation chain transfer (RAFT), [53] and atom transfer radical polymerization (ATRP).[54] To a reader versed in polymer synthesis, such complex systems are often restricted to small scales of the academic chemistry benchtop due to their costly initiators and catalysts. However, their industrial applicability is improved through the grafting-through approach as large macromolecules synthesized by traditional industrial approaches, such as ring opening polymerization (ROP) [55] and coordination-insertion polymerization (e.g. Ziegler-Natta), [56] dilute the costly requirements of the controlled polymerizations.

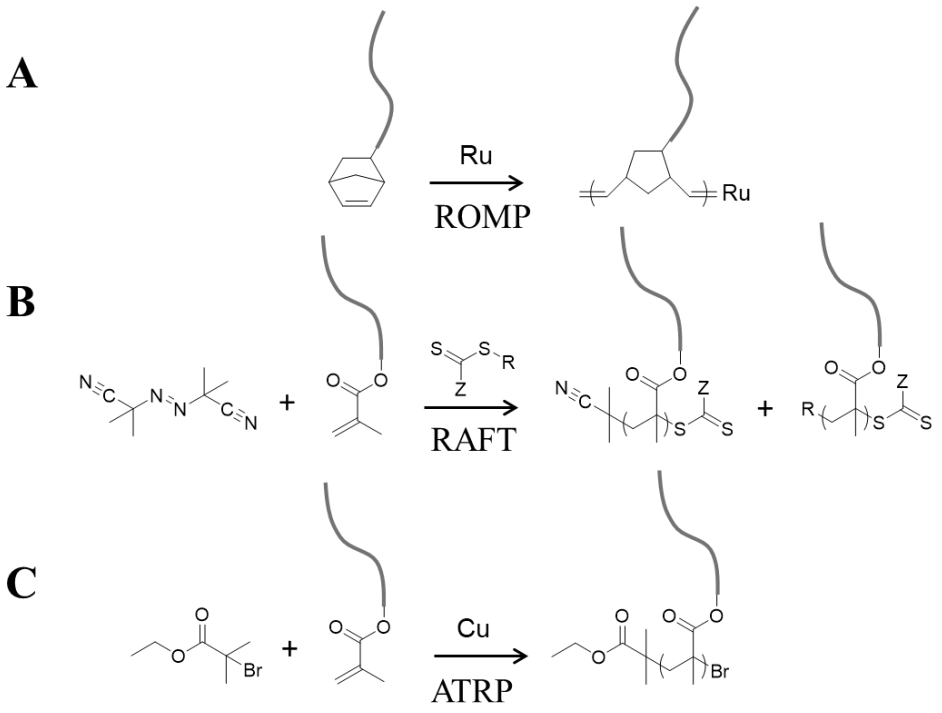

Figure 4.2: Grafting-through brushes using controlled polymerizations. (**A**) Ring opening metathesis polymerization (ROMP) of macromonomers with a norbornene end group using a generic ruthenium catalyst. Ruthenium catalyst specifics such as Grubbs catalysts can be found

in literature.[52] (**B**) Reversible addition-fragmentation chain transfer (RAFT) polymerization of macromonomers with a methacrylate end group using AIBN as an initiator and a generic RAFT chain transfer agent (CTA). Both the AIBN and CTA initiated brushes are shown in their "off" state. CTA specifics can be found in literature.[53] (**C**) Atom transfer radical polymerization of macromonomers with a methacrylate end group using ebib as an initiator and a generic copper catalyst. Copper catalyst and ligand specifics can be found in literature.[54]

ROMP[52] (**Figure 4.2**) is a polymerization technique that originated from the great success of small molecule metathesis, or rearrangement of olefin fragments, using various late transition metal catalysts and has expanded with the commercialization of improved Grubbs catalysts (G3). The synthetic strategy is now often employed in brush synthesis typically leveraging the high ring strain of norbornene end functionalized macromonomers. However, one key issue is the catalyst also functions as the initiator, which remains tethered to the growing chain end and thus requires stoichiometric quantities per desired number of polymer strands. Additionally, ROMP limits backbone chemistries to strained rings (i.e. norbornene, cyclobutene, etc.) and requires end termination (e.g. with vinyl acetate) and further functionalization to enable sequential polymerization of different chemistries (e.g. methyl methacrylate).

RAFT[53] (**Figure 4.2**) is a living radical polymerization where the polymer chain ends spend a majority of their time in a deactivated state, thereby limiting unwanted chain transfer or termination events. It is empowered by the inclusion of a chain transfer agent (CTA), typically a dithioester Z-C(=S)S-R, which undergoes reversible on-off switching with growing polymer chains first activated by an added initiator (e.g. AIBN). Depending on the identity of the R/Z substituents, RAFT CTA's are able to widely control the polymerization of various monomers including (meth)acrylates, (meth)acrylamides, acrylonitrile, styrene, butadiene, vinyl acetate and vinyl chloride. However, one of the main issues with RAFT is the result of polymer strand mixtures initiated either by the added initiator (AIBN) or the CTA itself, which precludes

polymer strands with homogenous end functionalization. Furthermore, the number of actively growing strands (i.e. “on”) are defined by the amount of added initiator and not the CTA, which creates a balance between reaction time and the end functionalization impurity described above.

ATRP[54] (**Figure 4.2**) is a similar living radical polymerization where the transfer of a capping bromine from the growing chain end to a catalyst dictates the on-off state. Traditionally, ATRP catalysts are copper (I) species with complexing multidentate nitrogen ligands that tune the catalyst activity. In contrast to RAFT, monomer polymerization is more limited to (meth)acrylates, styrene and acrylonitrile, but polymerization of monomers such as (meth)acrylamides and methacrylic acid are achievable with careful tuning of reaction conditions. Unique to this polymerization, the catalyst can easily be purified and removed with fresh catalyst added to enable seamless continuation of the chain end polymerization on demand. Furthermore, the bromine end cap can easily undergo substitution to enable homogenous brush end functionalization.

4.3 Conclusion

It is important to note that grafting-through macromonomers using the controlled polymerization strategies discussed in this chapter neither represents a comprehensive insight into the nuances of each system nor the current state-of-the-art of each polymerization scheme. Instead, it is intended to highlight the various strategies currently used within the literature in order to provide context to brush synthesis presented in this dissertation. Those who are interested in ongoing research aimed to increase polymerization efficiency, scalability and applicability within the context of brushes should pursue work conducted by more qualified polymer chemists in the field.[52-54] Although each polymerization strategy can be effectively used,

ATRP is heavily leveraged in this dissertation to graft-through brushes to empower a novel material platform (**Chapter 5,6,8**). Furthermore, a combination of orthogonal polymerization methods (e.g. RAFT & ATRP) is proposed to empower future architectural design (**Chapter 9**).

CHAPTER 5

BRIDGING THE FIRMNESS GAP: LINEAR-BRUSH-LINEAR TRIBLOCKS

5.1 Introduction

Although the brush-like architecture offers an elegant foundation to independently program softness and firmness into elastomers, it is necessary to bolster the architecture with additional synthetic tools beyond what traditional elastomer networks can provide (**Section 3.5**). Fortunately, a host of literature on self-assembled triblock copolymer physical networks provides welcomed insight as the triblock structure has shown enhanced mechanical properties over their covalently crosslinked counterparts.[57-60] Thus, the brush-like architecture can be embedded into a linear-brush-linear (LBL) ABA scaffold, which not only contain dissimilar chemical blocks but also physically distinct architectures (**Figure 5.1**). The result is a highly tunable self-assembled LBL thermoplastic elastomer (or plastomer) platform that has enhanced firmness empowered by strong microphase separation. This platform maintains the brush-like architectural triplet of brush length (n_{bb}), side chain length (n_{sc}) and grafting density (n_g), while adding linear block length (n_L) and corresponding volume fraction (ϕ_L). Self-assembly also enables observable physical features on length scales nontrivially related to the linear-brush periodicity (d_3), physical domain size (d_2), and inter-brush distance (d_1). The following sections will discuss a synthetic summary for LBL's covered in this entire dissertation (**Section 5.2**), the structural and physical characterization of LBL's by tuning the parameters of n_{bb} and n_L (**Section 5.3**), and an analysis of these tuned parameters (**Section 5.4**).

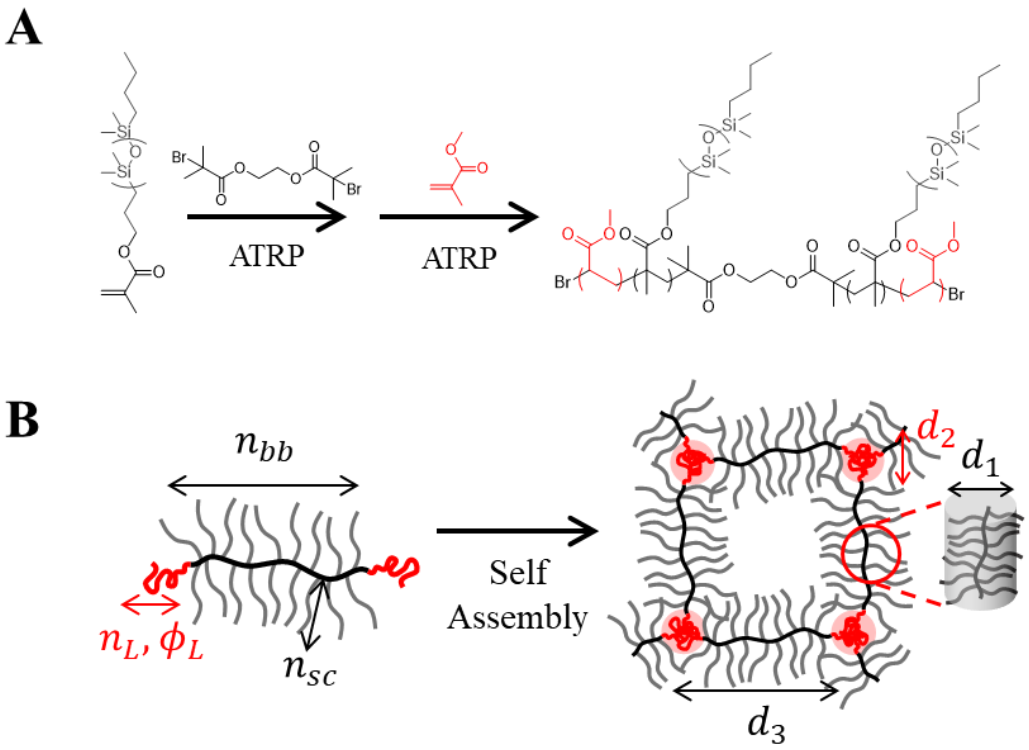

Figure 5.1: Linear-brush-linear (LBL) self-assembled platform. (**A**) Representative synthetic scheme showing the sequential polymerization of the LBL platform (**B**) Programmable features of the LBL platform include brush length (n_{bb}), side chain length (n_{sc}), linear block length (n_L) and volume fraction (ϕ_L), which self assembles into physical networks with nontrivially related physical parameters of linear-brush periodicity (d_3), physical domain size (d_2) and inter-brush distance (d_1).

5.2 LBL Plastomer Synthesis and Molecular Characterization

The procedures and expertise outlined herein serve as a general guiding principal for the synthesis of LBL plastomers. A full description and characterization of LBL plastomers with specific architectural parameters can be found in the literature.[61]

Typical LBL plastomers covered in this dissertation are synthesized from two components comprising each block: monomethacryloxypropyl-terminated poly(dimethylsiloxane) (PDMS) macromonomers as the brush B-block and methyl methacrylate

(MMA, 99%, ACROS) monomers as the linear L-block. This chemical combination is chosen as it shows a particularly strong phase separation.[62] PDMS macromonomers are commercially available in two lengths as either MCR-M11 (Gelest, average molar mass M_n = 1000 g/mol and dispersity, $Đ$ =1.15) or MCR-M17 (Gelest, M_n = 5000 g/mol and, $Đ$ =1.15), with their corresponding ^{1}H-NMR spectra in **Figure 5.2.** The side chain length (n_{sc}) of each is determined by the number of PDMS repeat units from ^{1}H-NMR plus approximately 3 additional repeat units to account for the extra non-PDMS length (i.e. 11.4 + 3) to respectively yield n_{sc} = 14.4 and 71.2 for MCR-M11 and MCR-M17. Both the PDMS macromonomers and MMA should first be passed through a basic alumina column to remove radical inhibitor added by the suppliers.

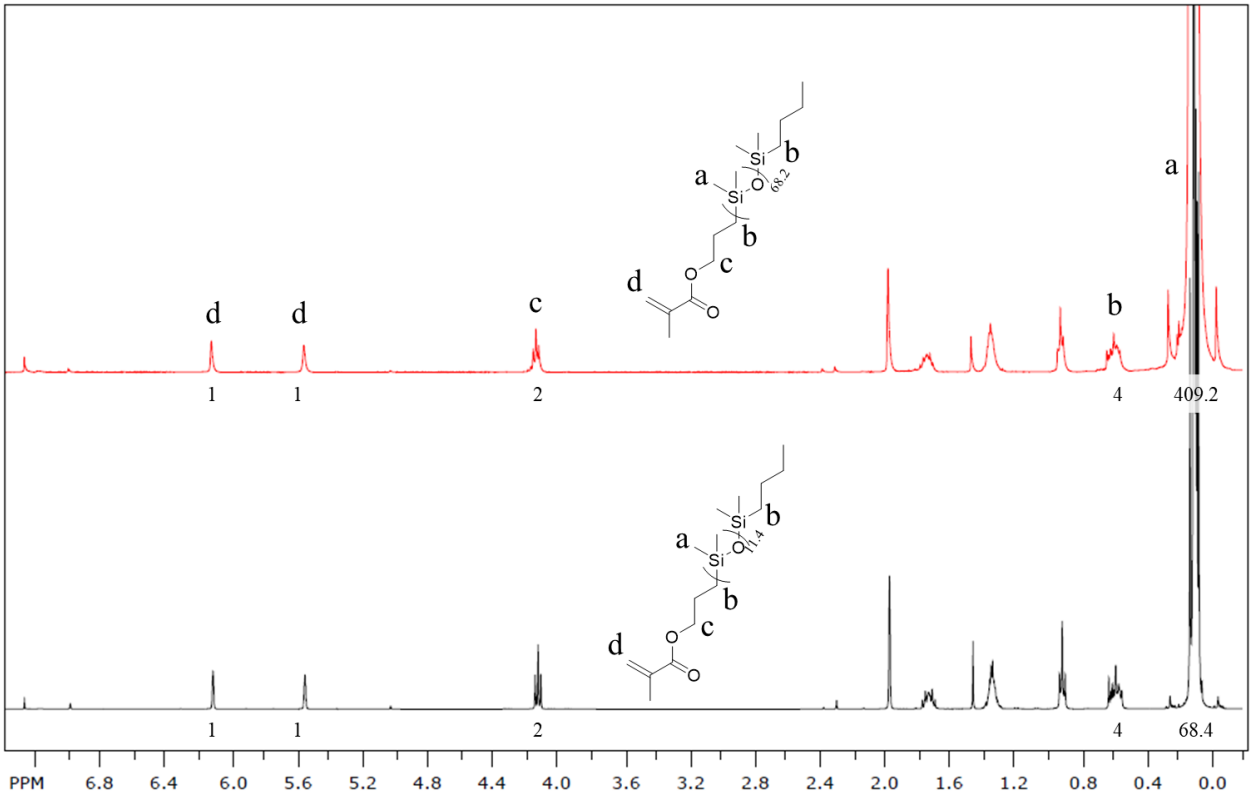

Figure 5.2: ^{1}H-NMR of raw MCR-M11 and MCR-M17 PDMS macromonomers. (400 MHz, $CDCl_3$): 6.12, 5.56 (C**H**$_2$=C(CH_3)C=O, s, 1H), 4.12 (CO-OC**H**$_2$-, t, 2H), 3, 0.55 (-C**H**$_2$-($Si(CH_3)_2$-O)$_n$-C**H**$_2$-CH_2-, m, 4H) 0.09 (-(Si(C**H**$_3$)$_2$-O)$_n$-, s, 68.4H MCR-M11 (black) and 409.2

MCR-M17 (red)). n_{sc}= [area(a)/6] + 3, providing 14.4 (MCR-M11) and 71.2 (MCR-M17) by approximating 3 additional repeat units comprise the side chain outside of PDMS.

An LBL plastomer is synthesized by sequential growth of the brush and then linear blocks via atom transfer radical polymerization (ATRP)[54] using a difunctional initiator and a highly active copper complex to promote polymerization of the sterically hindered side chains. As an example, MCR-M11 (50.0 g, 50.0 mmol), ATRP difunctional initiator ethylene bis(2-bromoisobutyrate) (2f-BiB, 97%, Sigma Aldrich, 15mg, 41.6 μmol), ATRP ligand *tris*[2-(dimethylamino) ethyl] amine (Me_6TREN, Sigma Aldrich, 19.2 mg, 22.2 μL, 83.3μmol) and toluene are bubbled with dry nitrogen for approximately 1 hour inside a Schlenk flask. Copper(I) bromide (Cu(I)Br, 99.999%, Sigma Aldrich, 8.3 mg, 83.3 μmol) is quickly added to the reaction mixture through the top of the flask. Subsequently, the flask is resealed, additionally purged with nitrogen for approximately 15 minutes, and then immersed in a 45 °C oil bath. The polymerization is allowed to proceed with periodic samples taken from the nitrogen purged Schlenk arm and monitored by ^{1}H-NMR. The polymerization is stopped by opening the flask and exposing the reaction mixture to air upon reaching the desired brush length (n_{bb}) (approximately 70-80% conversion), as determined by the disappearance of methacrylate end group (d) in relation to the PDMS reference (a+a') (**Figure 5.3**). With the provided chemical quantities above, the brush length reaches approximately n_{bb} = 900 after 12 hours at 75% monomer conversion. Using this sequential growth process, it is imperative to remove residual unreacted macromonomer from the reaction mixture. One effective approach is identifying a solvent which dissolves the macromonomer, but not the brush. For instance, residual unreacted MCR-M11 macromonomer can be removed by precipitating the reaction mixture in excess methanol, which also sufficiently removes residual catalyst. After drying, growth of MMA linear blocks proceeds

in a relatively similar fashion, as tracked by the emergence of PMMA (e') in reference to PDMS (a') within the brush (**Figure 5.3**). During this step, MMA can be added in excess (~1 brush mass equivalent) and the polymerization stopped with the desired n_L or ϕ_L tracked by ^{1}H-NMR. The resulting LBL is swelled and washed with excess acetone to remove MMA homopolymer as tracked by the disappearance of PMMA, then swelled and washed with excess hexane to remove unreacted PDMS bottlebrush as tracked by the increase in PMMA of the system, and dried overnight. Representative ^{1}H-NMR spectra of each sequential polymerization and washing steps (unreacted macromonomer, brush growth, purified brush, unpurified LBL, LBL purified with acetone, LBL then sequentially purified with hexane) is quantified in **Figure 5.3** of an LBL using MCR-M17 (**Chapter 6**). Finally, the LBL plastomer is dissolved in solvent, cast into Teflon petri-dishes (Welch Fluorocarbon) and left to dry under ambient conditions overnight. Casting conditions (solvent, concentration, drying rate, etc.) has minimal impact on the resulting mechanical properties (not shown) and does not preclude comparison of different LBL's. For a typical LBL cast in this dissertation, the triblock copolymer is dissolved in 85 weight% of THF.

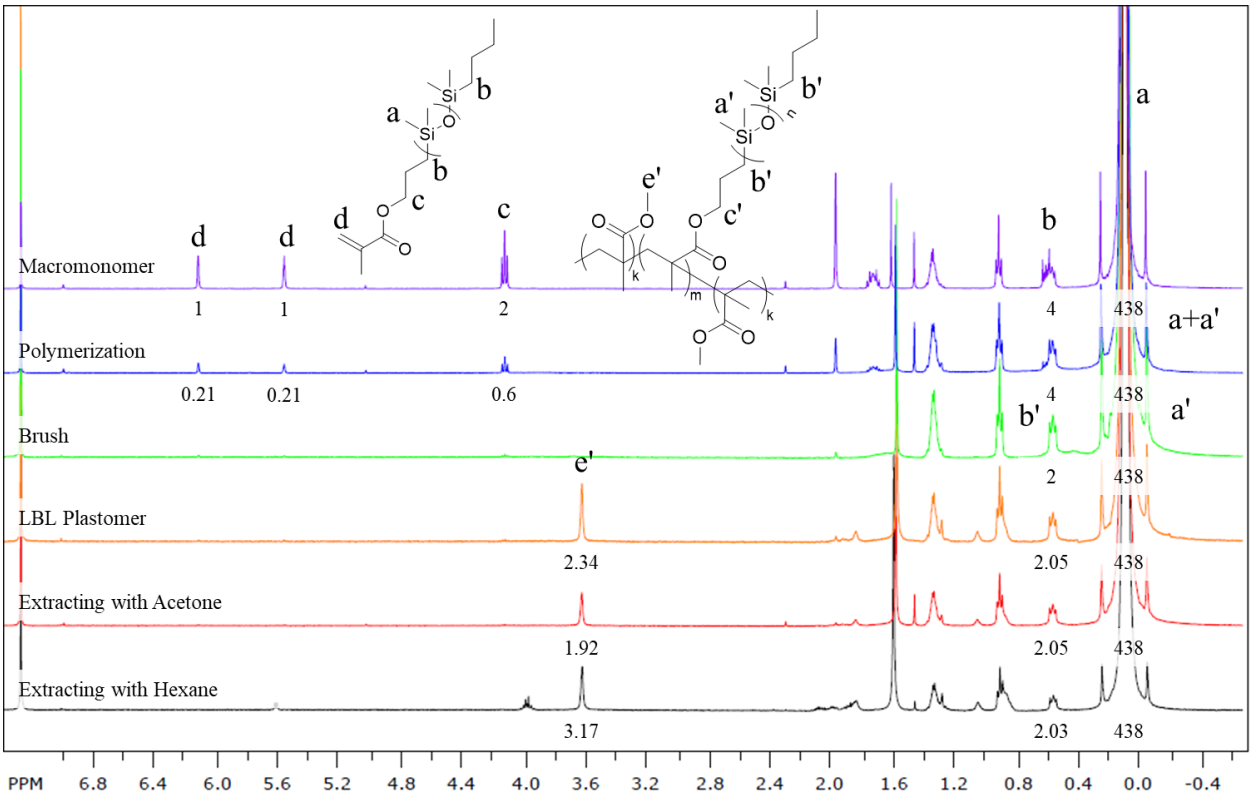

Figure 5.3: ^{1}H-NMR of LBL plastomers at different stages of synthesis. For PDMS n_{sc} = 70 (chapter 5) brushes (400 MHz, $CDCl_3$): 6.12, 5.57 (CH_2=C(CH_3)C=O, PDMS macromonomer, s, 1H), 4.12 (CO-OCH_2-, PDMS macromonomer, t, 2H), 0.55 (-CH_2-(Si(CH_3)$_2$-O)$_n$-CH_2-CH_2-, PDMS macromonomer and brush mixture, m, 4H) 0.09 (-(Si(CH_3)$_2$-O)$_n$-, PDMS macromonomer and brush mixture, s, 438H). For PMMA-PDMS-PMMA (**LBL**) plastomer (400 MHz, $CDCl_3$): 3.62 (COO-CH_3, s, 3H), 0.55 (-CH_2-(Si(CH_3)$_2$-O)$_n$-CH_2-CH_2-, m, 2H) 0.09 (-Si(CH_3)$_2$-, s, 438H). $Conv_{PDMS} = ([Area(a + a')/438] - [Area(d)/1])/[Area(a)/438]$. Peaks c' and 1 set of 2H b' for MCR-M17 brushes do not show on ^{1}H-NMR in $CDCl_3$ in contrast to MCR-M11 brushes (**see 5.2**), $n_L = [Area(e')/3]/[Area(a)/438] * n_{bb}$ where $n_{bb} = Conv_{PDMS} * \frac{[M]}{[I]}$. Subsequent washing with PDMS anti-solvent acetone and PMMA anti-solvent hexane removes acetone soluble PMMA homopolymer and hexane soluble PDMS brush, respectively.

5.3 LBL Physical Characterization

Both brush block (n_{bb}) and linear block (n_L) lengths or linear block volume fraction (ϕ_L) can be verified by independent analytical techniques to shed light on the brush and LBL self-assembly structure responsible for their enhanced mechanical properties. For instance, molecular

imaging of B-block brushes via atomic force microscopy (AFM) is made possible by exploiting the unique spreadability of brushes on substrates.[63] Monolayers prepared by Langmuir-Blodgett (LB) techniques enable visual characterization of their worm-like brush backbones such as the series shown in **Figure 5.4**, which verifies increasing n_{bb} consistent with ^{1}H-NMR.

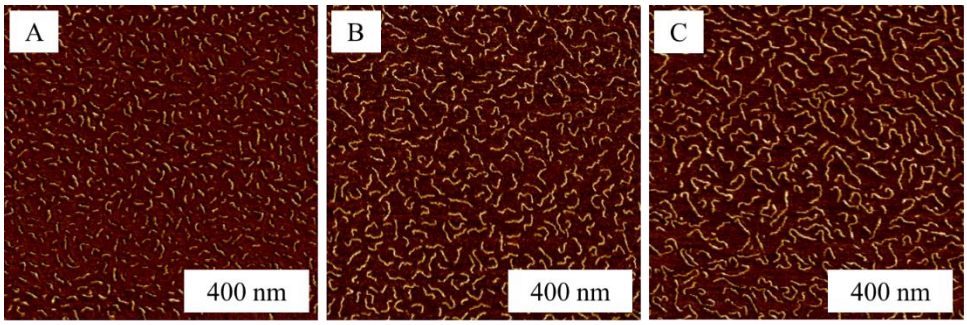

Figure 5.4: AFM of brushes. Monolayers of MCR-M17 brushes (**Section 6.2**) with different brush lengths (n_{bb}) prepared by Langmuir-Blodgett (LB) technique. **(A)** n_{bb} = 100 **(B)** n_{bb} = 300 **(C)** n_{bb} = 450.

Furthermore, LBL plastomers can be self-assembled into thin films that may be probed via AFM by tapping into the films to reveal hard glassy PMMA L-block domains, such as the series in **Figure 5.5** showing increasing ϕ_L. Note that these images only elucidate the morphology and dimensions of the glassy domains and not their actual connectivity within the soft brush matrix. Nevertheless, the spherical domains grow in size and show a potential transition to vesicle-like self-assembly at higher ϕ_L.

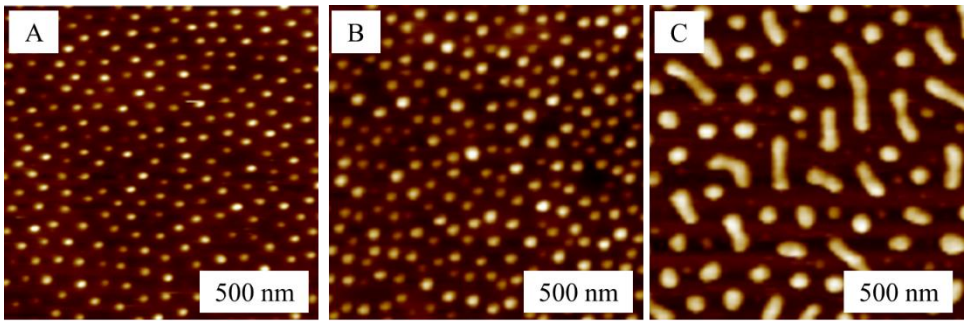

Figure 5.5: AFM of self-assembled LBL domains. LBL plastomer thin films via drop-casting with increasing L-block volume fraction (ϕ_L). Domains are enhanced by exposing thin films to solvent vapors. **(A)** ϕ_L = 0.032 **(B)** ϕ_L = 0.055 **(C)** ϕ_L = 0.105.

LBL physical features are also probed via ultra-small-angle X-ray scattering (USAXS) to reveal order at various length scales nontrivially related to the linear-brush periodicity (d_3), characteristic ripples of monodisperse spherical domains (d_2) and inter-brush distance (d_1) (**Figure 5.6A**). Depending on the programmed dimensions, these lengths range from d_3 = 40-150 nm, d_2 = 20-40 nm and d_1 = 3.4 nm for LBL's synthesized with MCR-M11.[61,64] In order to satisfy packing constraints within domain size d_2, remarkable degrees of L-block strand aggregation (Q = 300-1000) are required.[61,64]

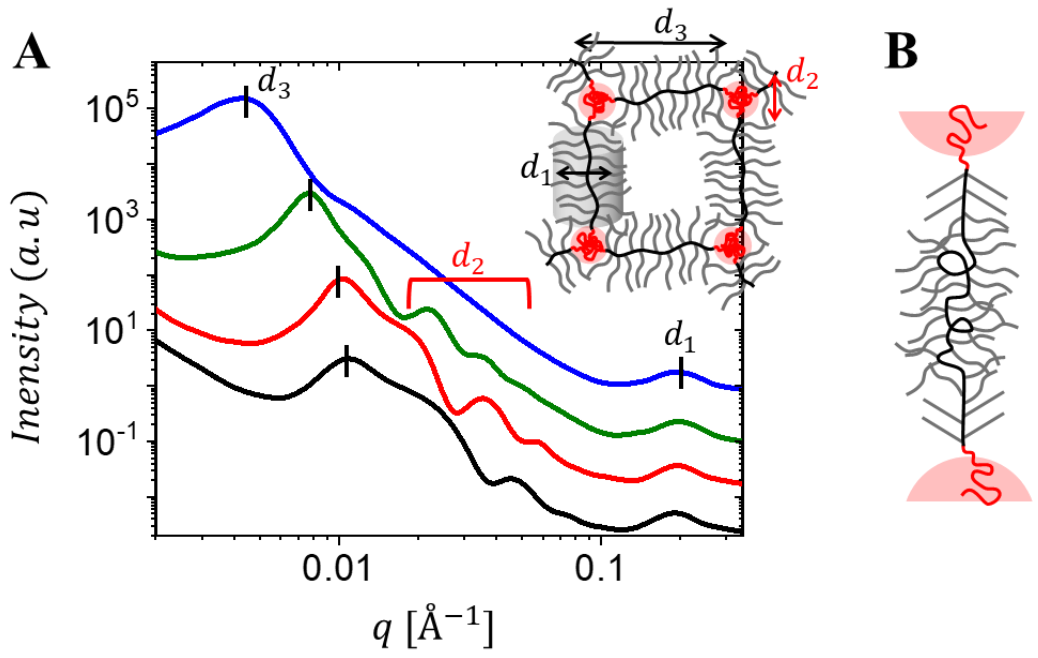

Figure 5.6: USAXS of LBL plastomers with increasing ϕ_L decodes LBL firmness. (**A**) Characteristic length scales of physical parameters are observed in X-ray traces including: inter brush distance (d_1), characteristic interference (form-factor) pertinent to the spherically-shaped domains (d_2), and domain-brush periodicity (d_3). (**B**) Strong microphase separation and high degree of packing at the linear-brush interface locally strains both the brush backbone and side chains into a nearly fully extended conformation.[64]

This unusually high aggregation and strong microphase separation causes brush network strands to adopt a nearly fully extended conformation localized at the linear-brush interface such that the side chains themselves are fully extended and angled away from the interface. The exceptionally strained conformation is aimed to minimize the brush strand footprint at the interface in order to satisfy the microphase domain packing constraints (**Figure 5.6B**).[64] This effect drops off away from the interface as brush segments return to typical brush bulk physics, however, the overall enhanced strain within the network strand results in enhanced firmness.[64] Importantly, this effect does not interfere with the platform's ability to achieve tissue-relevant softness as the brush side chains maintain a soft matrix between physical crosslinks. Resulting

stress-strain responses can be measured under tension using a dynamic mechanical analysis (DMA) instrument from TA instruments. Unless otherwise stated, stretching experiments in this dissertation are performed at a strain rate of $0.005s^{-1}$. A representative series of LBL plastomers with distinct n_{bb} and similar ϕ_L cast in toluene (**Figure 5.7**) show significantly enhanced firmness relative to those observed by brush elastomers (**Section 3.5**).

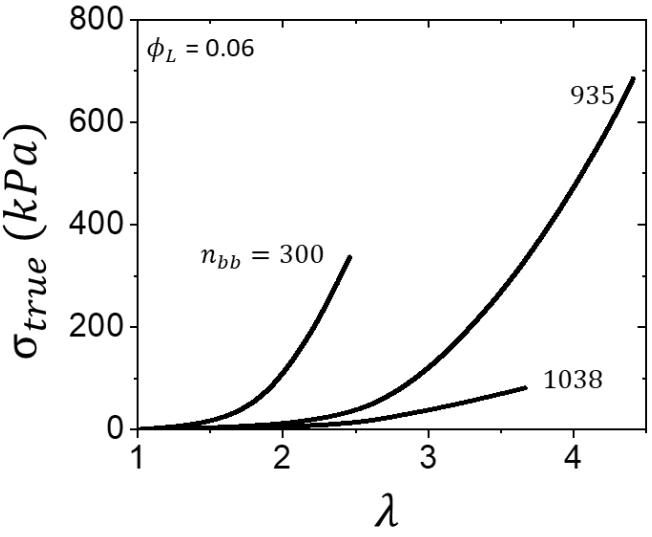

Figure 5.7: Representative stress-strain responses of MCR-M11 LBL plastomers. All samples contain similar L-block volume fraction (ϕ_L) and distinct brush length (n_{bb}). Tuning these two parameters demonstrates adequate control over the LBL platform mechanics.

5.4 Summary and Implications

An ensemble of elastic parameters extracted from LBL plastomers synthesized with n_{bb} = 300 - 1200, ϕ_L = 0.04 - 0.2 and cast in toluene are shown in **Figure 5.8**.[61] It is important to note that LBL plastomers exhibit a yielding phase analogous to tissue, discussed further in **Chapter 7**, and thus the extracted parameters only correspond to their elastic phase.

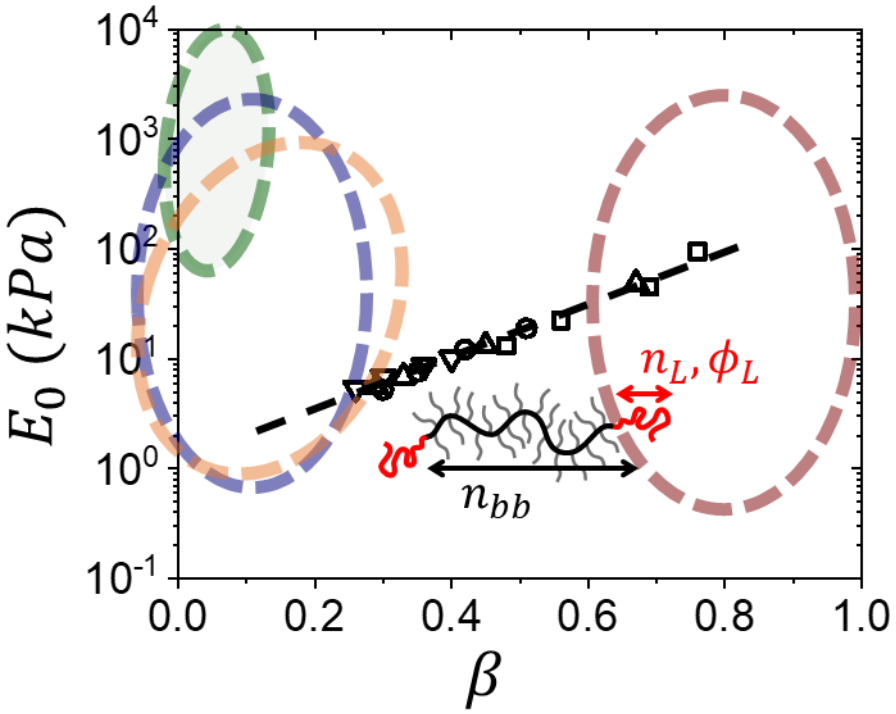

Figure 5.8: LBL plastomers bridge the firmness gap. An [E_0,β] map showing LBL plastomers using MCR-M11 (black) in relation to all other classes of elastic materials tissue (red), linear elastomers (green), gels (blue) and brush-like elastomers (orange). LBL series include n_{bb} = 300 (squares), 600 (circles), 900 (triangles), 1200 (upside down triangles) with increasing ϕ_L. The LBL platform successfully bridges the firmness gap between tissue and gels and improves upon brush elastomer firmness, however tuning of parameters n_{bb} and ϕ_L only leads to an observable coalescence of all materials and does not afford complete tuning over the entire [E_0, β] map.

Plotting these parameters on the elastic map reveals two observable features: (i) the LBL platform allows unprecedented bridging of the firmness gap and even penetrates the tissue zone, but (ii) the LBL plastomers unexpectedly coalesce and skirt many essential soft tissues such as muscle and fat. Therefore, although LBL plastomers outperform any current synthetic platform, varying the parameters of n_{bb} and ϕ_L simply does not provide complete independent control of softness and firmness to traverse the entire elastic landscape. However, the keen reader will

observe that a key brush architectural parameter (n_{sc}) has not been presently tuned, which can reasonably provide an avenue to decouple softness and firmness as discussed in **Chapter 6**.

CHAPTER 6

A PLATFORM TO TRAVERSE THE ENTIRE ELASTIC LANDSCAPE

6.1 Introduction

As it stands, LBL plastomers clearly outperform any synthetic platform in their ability to bridge the firmness gap, but the platform faces significant limitations without successfully decoupling the elastic features. Theoretically, the independent parameter of n_{sc} should enable successful regulation of softness and firmness, as demonstrated by covalent brush elastomers (**Section 3.5**), to provide access to the entire elastic map. However, as presented in **Section 5.2**, this dissertation only uses two commercial macromonomers (MCR-M11, MCR-M17), which would unfortunately constrain the platform's mechanical versatility. In light of this limitation, and to avoid the laborious synthesis of macromonomers with discrete n_{sc}, it is possible to program mixtures of macromonomers and spacers of different lengths to achieve the desired effect (**Figure 6.1**). Thus, this approach serves as an industry-friendly synthetic route to control the average n_{sc} over the entire network strand. The following sections will cover a synthetic summary for these LBL's tailored with (macro)monomers and the efforts to quantify the final programmed n_{sc} within the strand (**Section 6.2**), the structural and physical characterization of LBL's by tuning n_{sc} (**Section 6.3**) and a mechanical summary analysis of the LBL platform (**Section 6.4**).

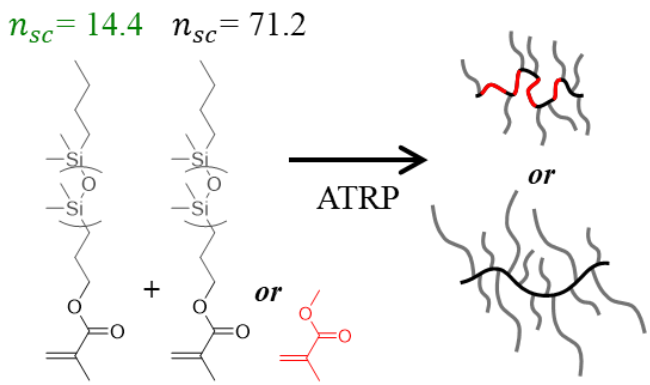

Figure 6.1: Tuning brush n_{sc} with mixtures of side chain lengths. Copolymerization of different (macro)monomers (n_{sc}= 1, 14, 70) enables tunable n_{sc} for implementation into the LBL scaffold (n_{bb}, n_{sc}, n_L, ϕ_L).

6.2 Synthesis of LBL Plastomers with Mixed Side Chains

The expertise outlined herein serves as a general guiding principal for the synthesis and characterization of LBL plastomers with mixed side chain lengths. Descriptions and characterizations of LBL plastomers specifically with long side chains (MCR-M17) and other architecturally parameters can be found in the literature.[27]

Without repeating general LBL plastomer synthetic approaches presented in **Section 5.2**, which largely remains the same, a few key distinctions should be highlighted for growing brushes with mixed side chain lengths. First, macromonomer mixtures (i.e. MCR-M11 and MCR-M17) are prepared by molar equivalents not mass equivalents to target desired n_{sc}. Second, using volatile spacers, in this case MMA, requires reduced temperatures (e.g. dry ice in acetone) during initial nitrogen purging to prevent evaporation, as evaporation which would affect the mixture stoichiometry and final n_{sc}. Third, it is prudent to use a different solvent system to facilitate mixtures containing long macromolecules due to the dilution of the functional methacrylate end group, which slows the polymerization rate. For instance, a mixture

of anisole and toluene ranging between 100% toluene with pure MCR-M11, and 80% anisole and 20% toluene with pure MCR-M17 is used. Note pure anisole is ill advised for PDMS MCR-M17 macromonomers due to poor solubility. Finally, longer macromonomers require distinct solvent systems for extracting residual unreacted macromonomer. In this case, sequential methanol and isopropanol washes is an effective choice for respectively removing MCR-M11 and MCR-M17 macromonomers selectively from the final brush mixture.

In order to properly characterize the resulting copolymer brush, it is essential not only to identify the final brush composition and conversion, but also the comonomer gradient during growth as different length side chains are expected to polymerize at different rates due to dilution of the end group. Copolymerization of MCR-M11 macromonomer and MMA spacer is relatively trivial as their copolymerization can be separately identified as demonstrated in a representative ^{1}H-NMR of a 25/75 mol% MMA/MCR-M11 stoichiometric mixture (**Figure 6.2**). This is accomplished by sampling the brush mixtures during growth and subsequently evaporating residual MMA monomer to yield a mixture of unreacted MCR-M11 macromonomer and the MCR-M11/MMA brush. Although an expected slight enrichment of MMA spacer is initially observed, the comonomer inclusion stabilizes towards initial stoichiometric values.

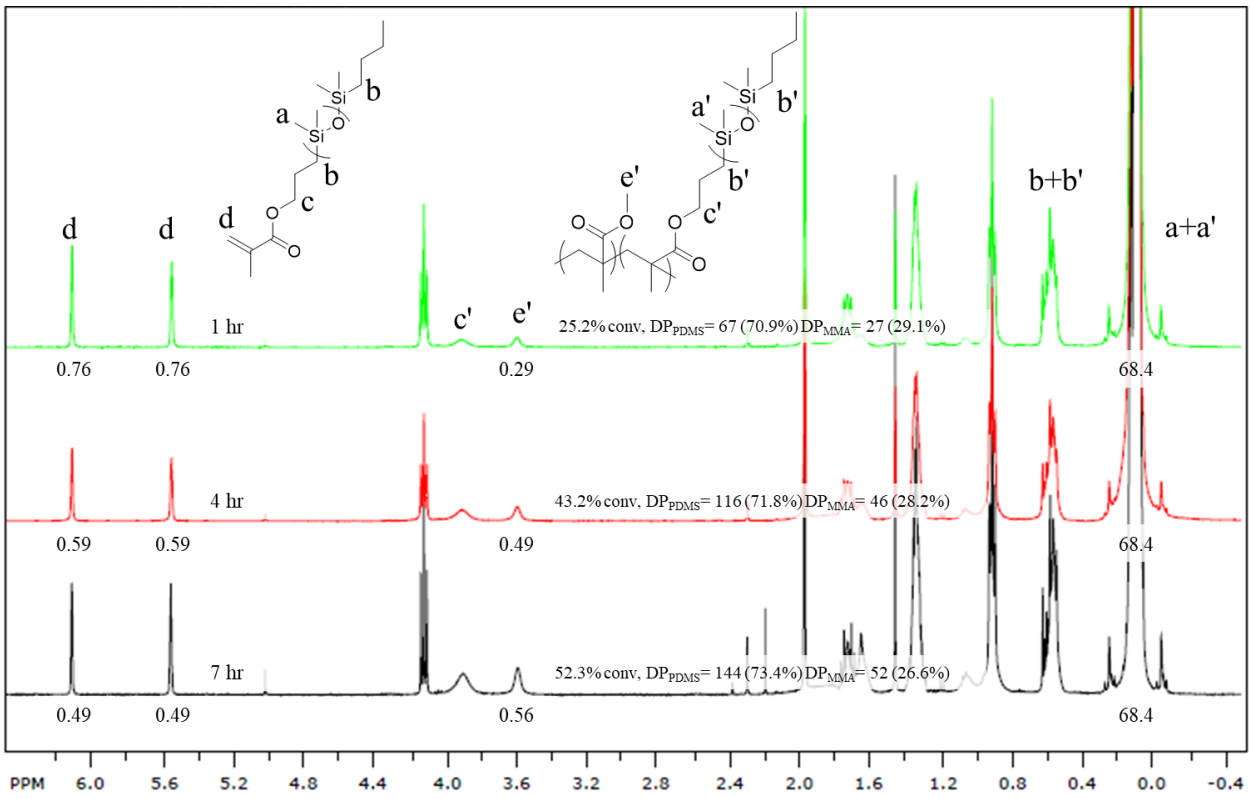

Figure 6.2: ^{1}H-NMR growth of a random MMA and MCR-M11 mixed brush. (400 MHz, $CDCl_3$): 6.12, 5.56 (C**H**$_2$=C(CH_3)C=O, PDMS macromonomer, s, 1H), 4.12 (CO-OC**H**$_2$-, PDMS macromonomer, t, 2H), 3.91 (CO-OC**H**$_2$-, PDMS brush, m, 2H), 3.62 (COO-C**H**$_3$, MMA brush, s, 3H), 0.55 (-C**H**$_2$-(Si(CH_3)$_2$-O)$_n$-C**H**$_2$-CH_2-, PDMS macromonomer and brush mixture, m, 4H) 0.09 (-(Si(C**H**$_3$)$_2$-O)$_n$-, s, 68.4H). DP$_{bbPDMS}$ = [area(a'+a)/68.4-area(d)/1]/[area(a'+a)/68.4]∗[PDMS]/[I], DP$_{bbMMA}$ = [area(e')/3]/[area(a'+a)/68.4] ∗[PDMS]/[I], n_{bb} = DP$_{bbPDMS}$ + DP$_{bbMMA}$, Conv$_{bb}$= n_{bb}/{([PDMS]+[MMA])/[I]}. ([PDMS]+[MMA])/[I] = 375, [PDMS]/[I] = 281.2.

Copolymerization and analysis of MCR-M11 and MCR-M17 macromonomer mixtures presents a more complex challenge as it is impossible to decompose their signals in ^{1}H-NMR. A reader well versed in ^{1}H-NMR may suggest comparing the PDMS polymer peak, which should be a combination of the two raw polymer peaks in **Figure 5.2**, to a fixed discernable reference that both macromonomers share, such as the hydrogens nearest the methacrylate end group that shifts upon polymerization (c to c'). However, this suggestion breaks down given ^{1}H-NMR of various unpurified brushes (**Figure 6.3**) as this peak all but disappears or infinitely broadens with

increased longer side chain fractions. In fact, even the c' reference in pure MCR-M11 brushes does not integrate to expectations. This problem is similarly observed in ^{1}H-NMR of large macromolecules studied in biochemistry,[65] but is largely unaddressed in most brush synthetic discussions. One possible explanation for this observation is that longer side chains shield the backbone from resonating in ^{1}H-NMR, but it ultimately remains a puzzling and unanswered casualty of the brush synthesis that should be investigated by more qualified NMR experts. Nevertheless, the n_{bb} can still be accurately determined from unpurified brush mixtures (**Figure 6.3**) as described in **Section 5.2**.

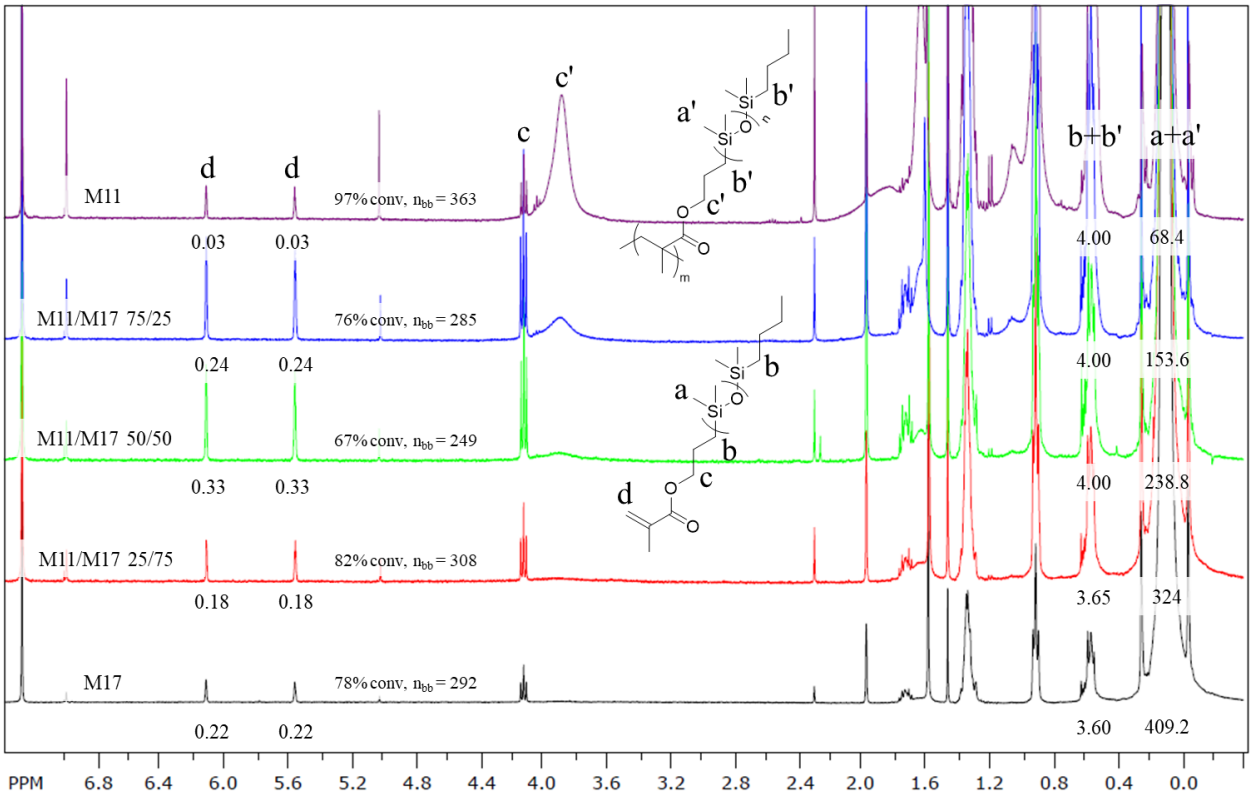

Figure 6.3: ^{1}H-NMR of random MCR-M11 and MCR-M17 mixed brushes. (400 MHz, $CDCl_3$): 6.12, 5.56 (C**H**$_2$=C(CH_3)C=O, unreacted macromonomer, s, 1H), 4.12 (CO-OC**H**$_2$-, t, 2H), 0.55 (-C**H**$_2$-(Si(CH_3)$_2$-O)$_n$-C**H**$_2$-CH_2-, m, 4H) 0.09 (-(Si(C**H**$_3$)$_2$-O)$_n$-, PDMS macromonomer and brush mixture, s, 68.4H - 409.2H depending on the stoichiometric ratio of added side chains). n_{bb} = [area(a'+a)/{corresponding stoichiometric H's}-area(d)/1]/[area(a'+a)/{corresponding stoichiometric H's}]∗[PDMS]/[I].

However, attempts to carefully measure final n_{sc} should be made in order to precisely and fully characterize the resulting brushes. In order to identify the final side chain composition, brush mixtures were first purified of residual macromonomers and a benzaldehyde external reference was added to each brush for further ^{1}H-NMR analysis (**Figure 6.4**). As previously shown, the methacrylate backbone peak (c') does not provide a universal pathway for measuring these brushes, however the peak associated with hydrogens surrounding either side of the siloxane polymer (b to b') has a unique shift without additional extraneous overlap that provides a viable pathway. Indeed, the hydrogens nearest to the backbone partially resonate in pure MCR-M17 brushes, while all four hydrogens do resonate in pure MCR-M11 brushes. Therefore, the a'/b' ratio, or the PDMS polymer peak (a') related to the macromonomer (b') peak, (**Figure 6.4**) of pure MCR-M11 and MCR-M17 brushes can be correlated to their corresponding n_{sc} (**Figure 6.5**) to serve as a reference for brush mixtures. Here the a'/b' vs n_{sc} relationship can be considered as a linear two-point calibration that can back calculate the n_{sc} of macromonomer mixtures given their measured a'/b' ratio. As expected, the y-intercept respectively falls between the theoretical cases of 3 and 9.2, where all b' resonate and perfectly equates to the extraneous PDMS repeat units described in **Figure 5.2** and where only the two b' hydrogens away from the backbone of MCR-M17 brushes resonate. It is important to note that a linear approach may not serve as the ideal calibration and could be better served by a non-linear fit (e.g. power law). Regardless of the best methodology, true n_{sc} can be considered falling within a narrow range of ~ 5-10 n_{sc} between a linear fit lower limit and perfect stoichiometric upper limit. However, the most efficient and direct approach to resolving this issue is future analysis by qualified NMR experts to enable resonance of the entire macromolecule. Furthermore, this lack of accurate structural analysis does not detract from the underlying effects on the resulting mechanical

properties, whereby mixing side chains into brushes can be efficiently utilized to enable sweeping control over firmness (**Section 6.3**).

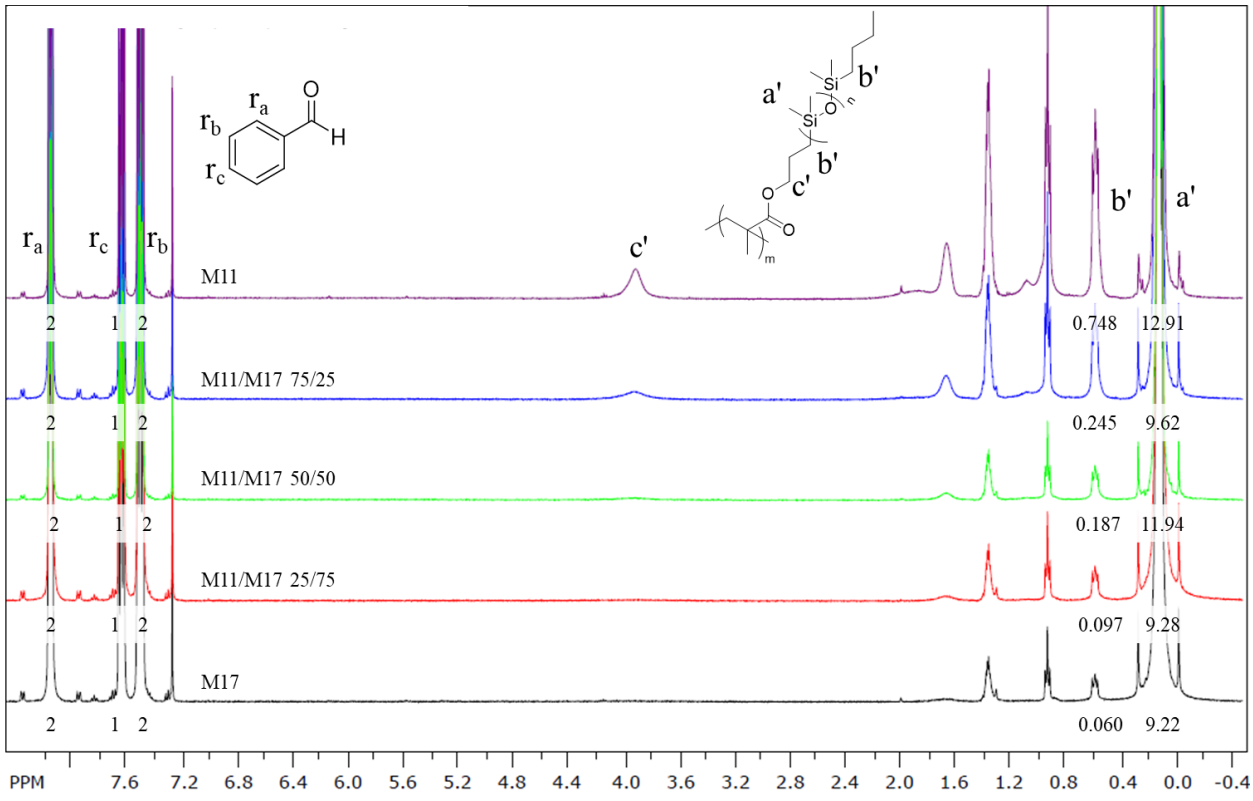

Figure 6.4: ^{1}H-NMR of purified random MCR-M11 and MCR-M17 mixed brushes with an external reference. (400 MHz, $CDCl_3$): 8.16 (Bz, d, 2H), 7.64 (Bz, t, 1H), 7.51 (Bz, t, 2H), 4.12 (CO-OC**H**$_2$-, t, 2H), 0.55 (-C**H**$_2$-(Si(CH$_3$)$_2$-O)$_n$-C**H**$_2$-CH$_2$-, m, 2H-4H, depending on effective side chain length) 0.09 (-(Si(C**H**$_3$)$_2$-O)$_n$-, brush, s, 68.4H - 409.2H depending on inclusion of side chains). Depending on side chain length the b' peak integrates between 4H (MCR-M11) or 2H (MCR-M17) consistent with disappearance of other peaks (i.e. c') near the brush backbone.

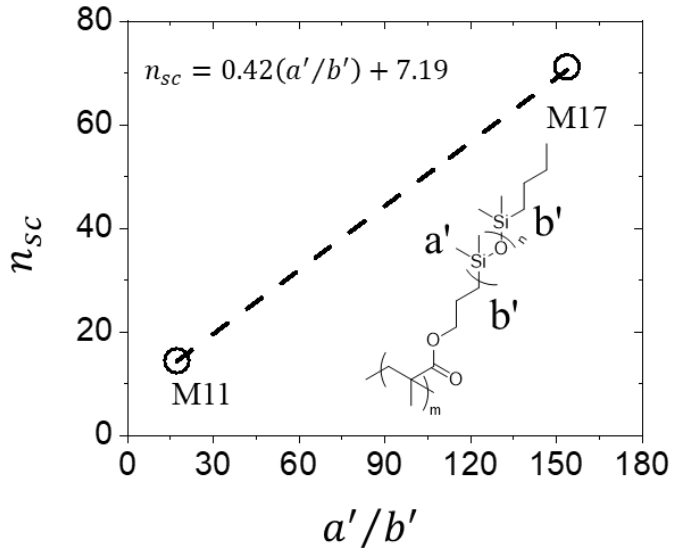

Figure 6.5: Two-point n_{sc} calibration using pure MCR-M11 and MCR-M17 brushes. The a'/b' ratio may be utilized as a reference to determine true inclusion of both MCR-M11 and MCR-M17 into brushes synthesized with macromonomer mixtures.

The linear fit can similarly be used to quantify the copolymerization gradient of MCR-M11 and MCR-M17 mixtures during growth (**Figure 6.6A-C**). First the n_{bb} and conversion is measured (**Figure 6.6A**), then the n_{sc} is calculated using the two point calibration from purified brushes (**Figure 6.6B**), and finally the calculated n_{sc} may be plotted versus the conversion (**Figure 6.6C**). While an expected enrichment of shorter MCR-M11 is initially observed, comacromonomer incorporation approaches stoichiometry albeit offset from expectations at higher conversions, most likely due to the inadequacies of the n_{sc} determination (**Figure 6.5**). After characterization of the final brush n_{sc} in MCR-M11 and MCR-M17 mixed brushes, MMA linear blocks were grown as described in **Section 5.2** using the attained PDMS composition (a') as a reference to calculate n_L as described in **Section 5.2**.

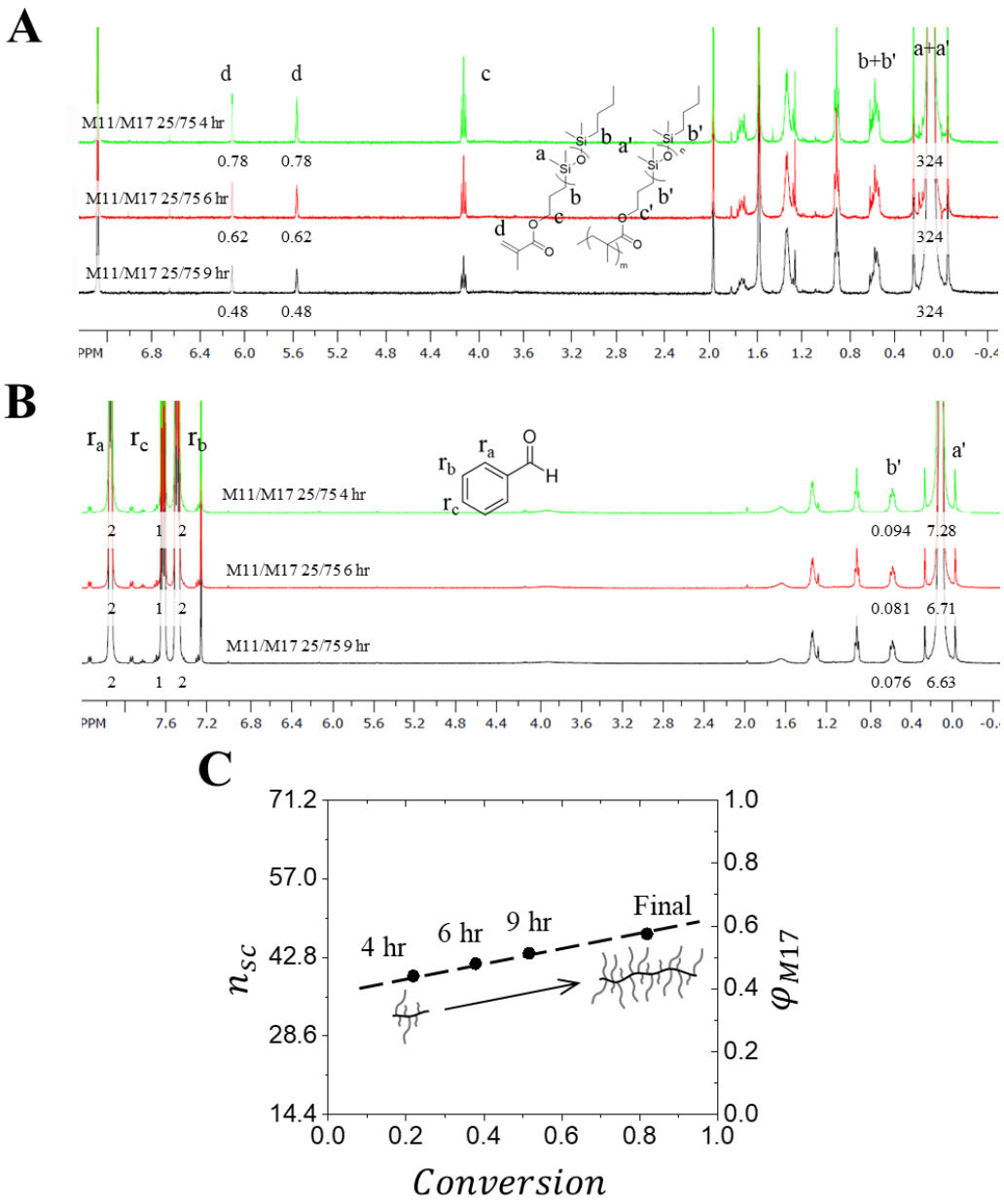

Figure 6.6: Tracking growth of a random MCR-M11 and MCR-M17 mixed brush. (A) ^{1}H-NMR of an unpurified random brush to quantify brush growth and conversion (400 MHz, $CDCl_3$): 6.12, 5.56 (C**H**$_2$=C(CH_3)C=O, s, 1H), 4.12 (CO-OC**H**$_2$-, t, 2H), 0.55 (-C**H**$_2$-(Si(CH_3)$_2$-O)$_n$-C**H**$_2$-CH_2-, m, 4H) 0.09 (-(Si(C**H**$_3$)$_2$-O)$_n$-, PDMS macromonomer and brush mixture, s, 324H characteristic of a 25/75 MCR-M11/MCR-M17 mixture). **(B)** ^{1}H-NMR of a purified random brush with external reference to quantify the side chain gradient during growth (400 MHz, $CDCl_3$): 8.16 (Bz, d, 2H), 7.64 (Bz, t, 1H), 7.51 (Bz, t, 2H), 4.12 (CO-OC**H**$_2$-, t, 2H), 0.55 (-C**H**$_2$-(Si(CH_3)$_2$-O)$_n$-C**H**$_2$-CH_2-, m, 2H-4H, depending on effective side chain length) 0.09 (-(Si(C**H**$_3$)$_2$-O)$_n$-, brush, s, depending on effective side chain length). The a'/b' ratio during growth

is input in to the two-point calibration (**Figure 6.5**) to determine n_{sc} of macromonomer mixtures. **(C)** conversion of a random brush from **A** versus calculated n_{sc} or fraction of MCR-M17 (φ_{17}) from **B**.

For MMA and MCR-M11 mixed brushes, it is observed in ^{1}H-NMR that growth of MMA linear (L) blocks (e") superimpose with the MMA (e') contained in the brush (**Figure 6.7**), but both of these can be deconvoluted through careful initial characterization of the mixed brush (**Figure 6.2**). Interestingly, both types of PMMA are visually discernable in ^{1}H-NMR as PMMA contained in linear blocks are sharp while PMMA contained in the brush are broad.

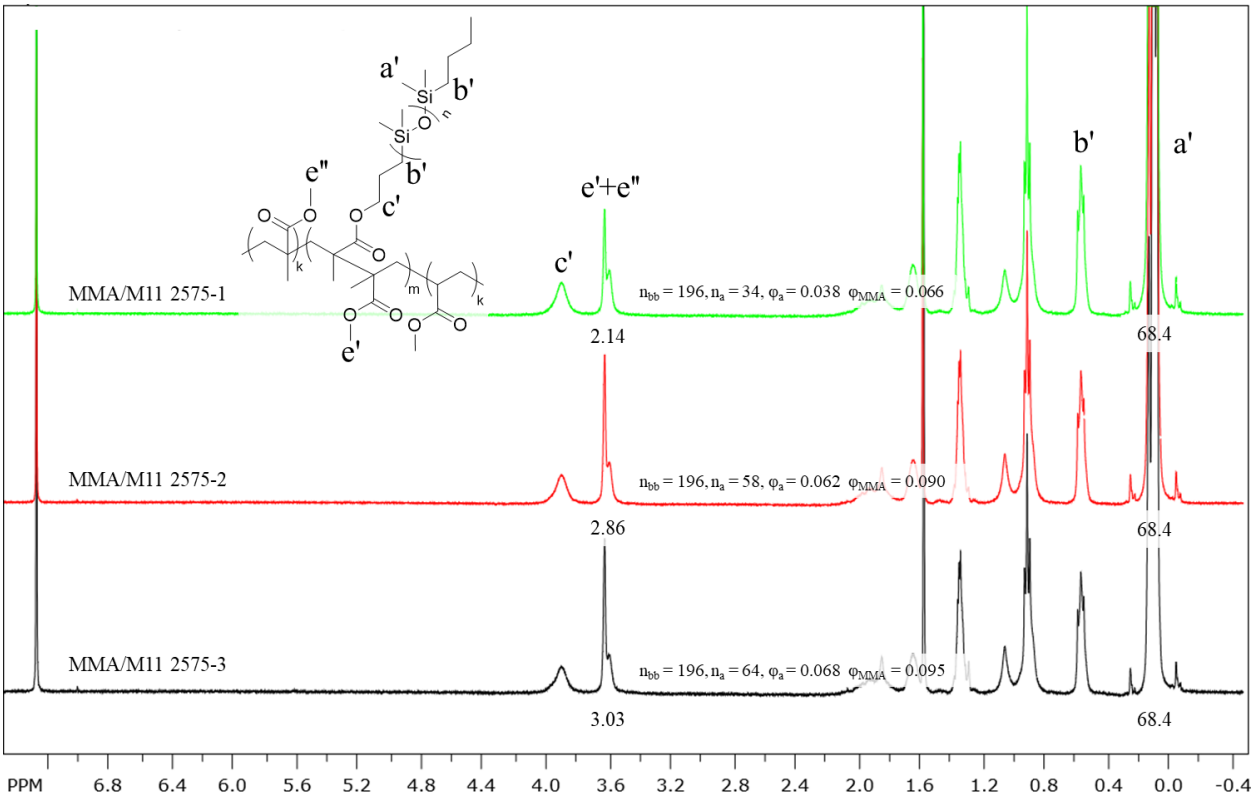

Figure 6.7: ^{1}H-NMR of an LBL series using a random MMA and MCR-M11 mixed brush. (400 MHz, $CDCl_3$): 3.91 (CO-OC**H**$_2$-, PDMS brush, m, 2H), 3.62 (COO-C**H**$_3$, MMA brush and linear mixture, s, 3H), 0.55 (-CH_2-($Si(CH_3)_2$-O)$_n$-C**H**$_2$-CH_2-, m, 2H) 0.09 (-Si(C**H**$_3$)$_2$-, s, 68.4H). n_L={area(e'+e'')/[area(a')/68.4]-[area(a')/68.4∗DP_{bbMMA}/DP_{bbPDMS}∗3]}∗n_{bb}/(3∗2).

6.3 Physical Characterization

Physical characterization techniques are largely identical to those described in **Section 5.3**; However, tuning n_{sc} affords discernable differences under AFM and USAXS. For instance, monolayers of MCR-M11 and MCR-M17 mixed brushes prepared by the LB method show increased spacing between neighboring backbones under AFM (**Figure 6.8A**). This spacing can be quantified and related to the increasing weight average side chain length ($n_{sc,w}$) (**Figure 6.8B**) calculated from ^{1}H-NMR (**Figure 6.5**), which is consistent with the thermodynamically preferred adsorption of longer side chains to substrates.[66] The near linear correlation suggests that the calibration in **Figure 6.5** is reasonable approximation.

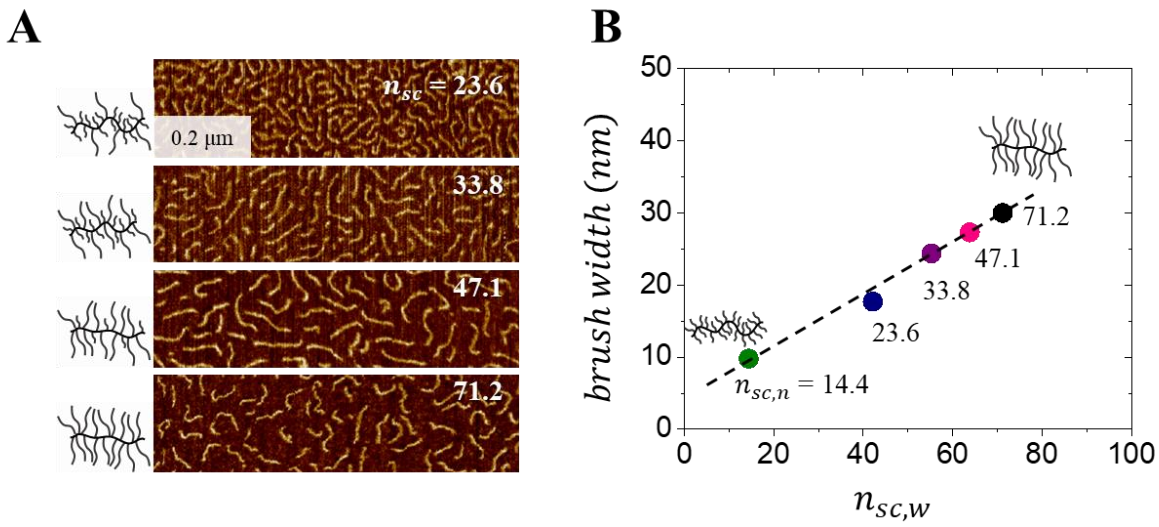

Figure 6.8: AFM characterization of MCR-M11 and MCR-M17 mixed brushes. (A) Images of brush block monolayers showing increased interbrush distance with increased n_{sc} = 71.2 fraction. **(B)** Brush width determined by AFM as compared to weighted average side chain length ($n_{sc,w}$) determined by ^{1}H-NMR **(Figure 5.4, 5.5**) showing a non-linear correlation due to long side chains first adhering to substrates. Brushes with n_{sc} = 14.4 (green), 23.6 (navy), 33.8 (violet), 47.1 (pink) and 71.2 (black).

USAXS of LBL plastomers grown with longer side chains also exhibit an increase on length scales related to the linear-brush periodicity (d_3) and the inter-brush distance (d_1) (**Figure**

6.9). Increases in d_3 from an increased n_{sc}, where n_{bb} and ϕ_L are held relatively constant, suggest network strand extension and enhanced firmness empowered by a stronger microphase separation of more sterically hindered longer side chains. LBL's from mixed MCR-M11 and MCR-M17 brushes also exhibit a consistent increase on length scales nontrivially related to the inter-brush distance (d_1) (**Figure 6.10A**) and follows theoretical predictions with number average side chain length ($n_{sc,n}$) as $d_1 \sim {n_{sc}}^{3/8}$ (**Figure 5.10B**).[27,67]

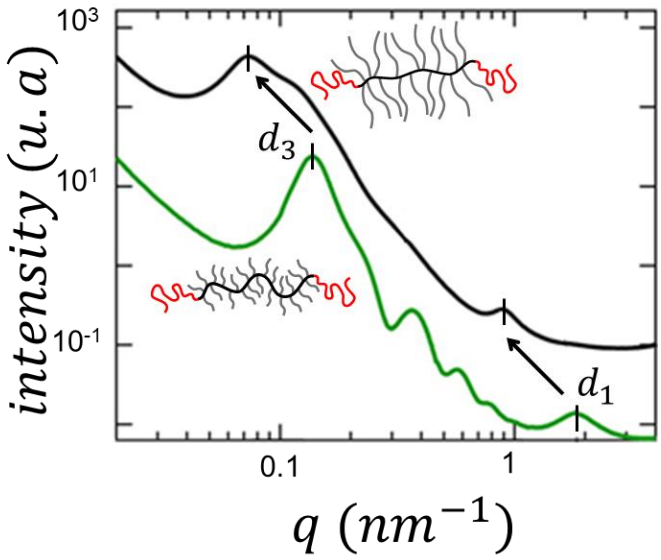

Figure 6.9: X-ray characterization of pure MCR-M11, MCR-M17 LBL plastomers. Both samples were prepared with a similar n_{bb} and ϕ_L. The observed increase of the interdomain spacing (d_3) of MCR-M17 plastomers (black) correlates with enhanced firmness from longer side chains (d_1).

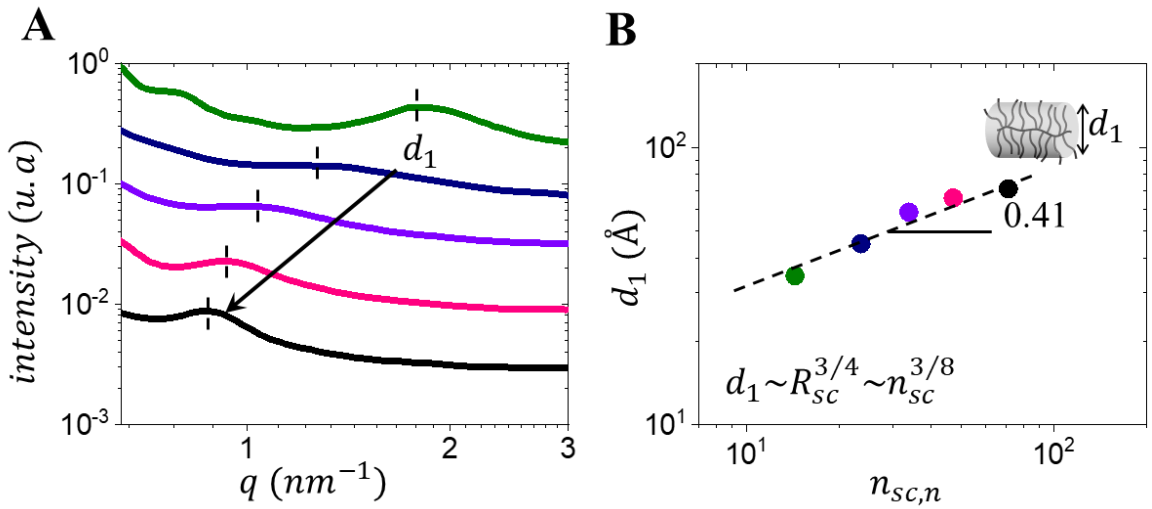

Figure 6.10: X-ray d_1 characterization of MCR-M11 and MCR-M17 mixed brushes. (A) Tracking increased interbrush distance peak (d_1). **(B)** Peak heights can be converted into d_1 values, which are consistent with increasing number average side chain length ($n_{sc,n}$) as predicted by theoretical considerations. Brushes with $n_{sc,n}$ = 14.4 (green), 23.6 (navy), 33.8 (violet), 47.1 (pink) and 71.2 (black).

Most importantly, the stress-strain responses were measured for an ensemble of mixed brush LBL plastomers programmed with n_{bb} = 200 - 450, ϕ_L = 0.02 - 0.1 and n_{sc} = 7.5 - 71.2, and cast in THF. A collection of stress-strain curves with similar E_0 (**Figure 6.11A**) and similar β **(Figure 6.11B**) highlights the versatility of varying n_{sc} with ϕ_L. Note that similar β does not equate to identical λ_{max} as predicted by theory (**Section 2.2)**. This is explained by LBL plastomer's yielding phase, which can provide relatively unpredictable extensibility (**Chapter 7**).

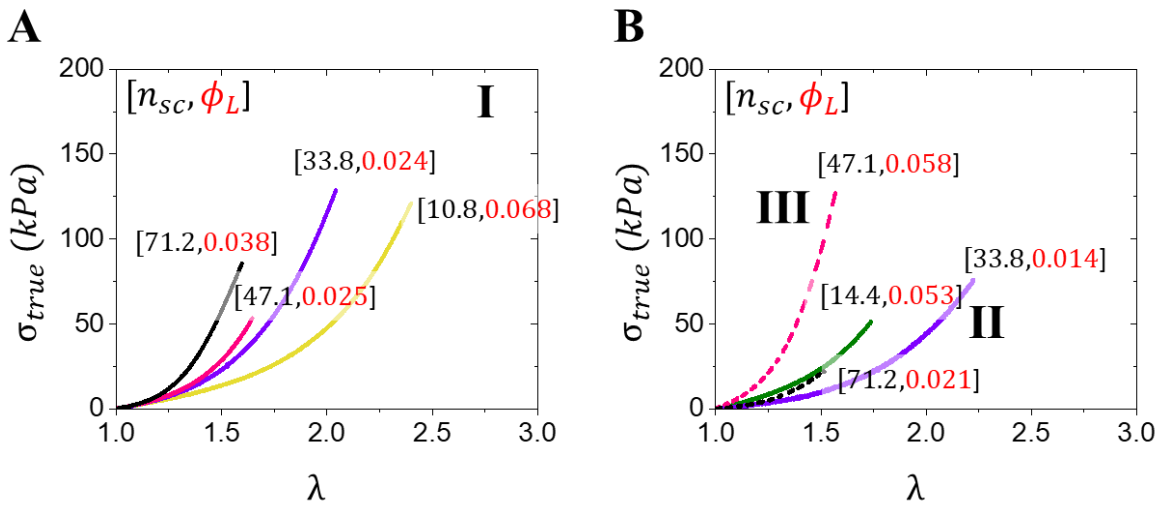

Figure 6.11: Representative stress-strain responses of mixed brush LBL plastomers. Varying the architectural parameters of n_{sc} and ϕ_L enable collections of either **(A)** LBL plastomers with similar E_0 = 25kPa and different β, or **(B)** two groups of LBL plastomers (dashed vs solid line) respectively with similar β = 0.77 and β = 0.46 but different E_0.

6.4 Summary and Applications

The extracted elastic parameters of an ensemble of LBL plastomers are shown on an [E_0, β] map in **Figure 6.12**. Successful variations of n_{sc}, n_{bb} and ϕ_L yields many notable features: (i) vertical or lateral cross sections can respectively yield collections of materials similar to those found in **Figure 6.11A,B**, (ii) each series universally coalesce onto discrete lines for a given average n_{sc} (dashed lines **Figure 6.12**) (iii) increasing $n_L$or ϕ_L simultaneously increases E_0 and β up the coalesced line, while increasing n_{bb} simultaneously decreases E_0 and β down the coalesced line, and (iv) increasing n_{sc} laterally shifts the observed coalesced line towards higher β. These empirical correlations enable general design rules towards traversing the [E_0,β] landscape, yet it is important to note that the dashed lines extend beyond the measured samples and can be theoretically filled with additional LBL triplets as evidenced by an supplementary MCR-M17 series with n_{bb} = 450 (hollow hexagons **Figure 6.12**).[27] However, the trend

boundaries are currently ill-defined and there likely exists a microphase regime change upon reaching high ϕ_L > 0.3. Comparison of these LBL plastomers with those in **Figure 5.8**, show a slight mismatch caused by the difference in casting solvent, which does not diminish the underlying importance of n_{sc} variation. Note that the vertical scale in **Figure 6.12** is shortened for ease of viewing.

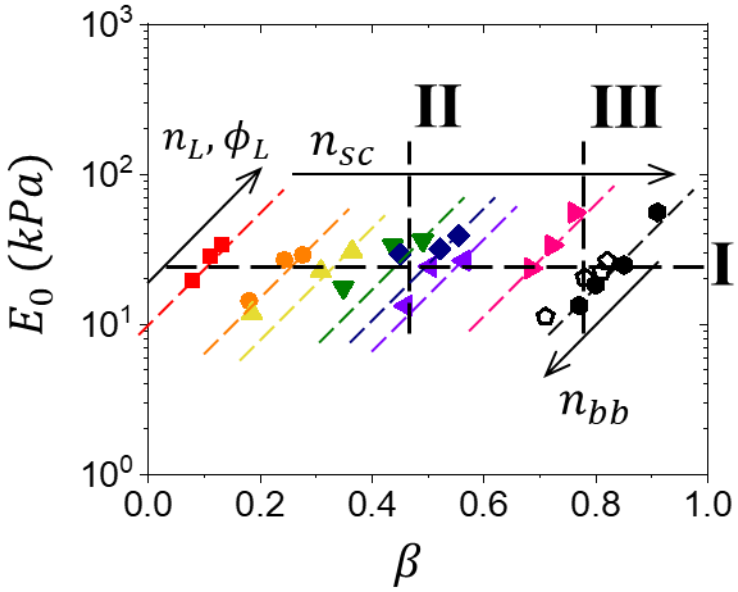

Figure 6.12: Programming LBL platform to traverse the elastic landscape. Elastic parameters of reported LBL plastomers extracted from corresponding stress-elongation curves on an [E_0, β] map. Identical colored symbols indicate samples with identical n_{sc} and n_{bb}, and varied ϕ_L, while a difference in colored symbol represents samples with increasing n_{sc} = 7.5 (red squares), 10.8 (orange circles), 12.9 (yellow triangles), 14.4 (green upside down triangles), 23.6 (navy diamonds), 33.8 (violet left triangles), 47.1 (pink right triangles) and 71.2 (black hexagons). Dashed lines are provided to guide the reader and delineate the coalescence of each series. Collections of materials that show either constant E_0 and different β (**Figure 6.11A**) or constant β and different E_0 (**Figure 6.11B**) may be identified by respectively dropping lateral lines (*I*) or vertical lines (*II, III*). General design rules (arrows) can be inferred from the collected series for tuning mechanical properties with architectural parameters (n_{bb}, n_{sc}, n_L, ϕ_L).

Theoretical analysis[27] enables universality for the overarching platform by correlating the attained mechanical properties with the corresponding architectural parameters (**Figure 6.13**) and serves as a foundation for fine-tuning future materials.

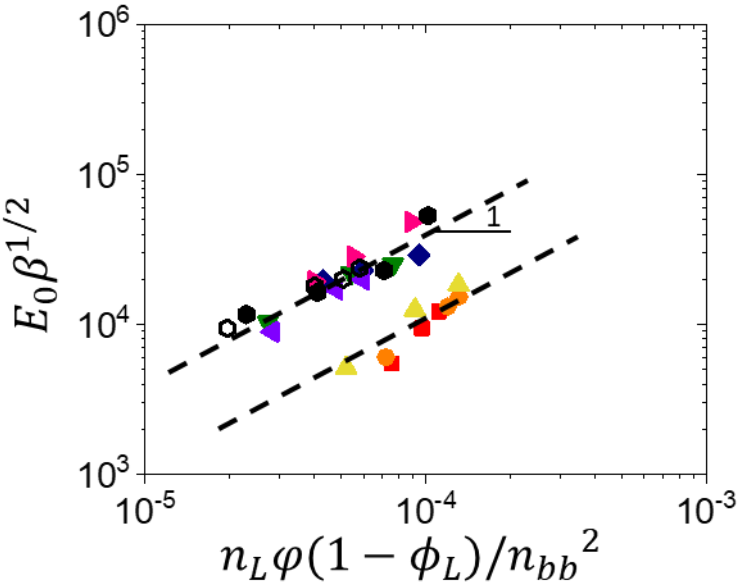

Figure 6.13: Universally collapsing the LBL platform. Theoretical considerations provide a direct route for universally programming the LBL platform, where $\varphi = n_g/(n_g + n_{sc})$

Keen observers will notice that pure MCR-M17 LBL plastomers in the [E_0, β] map (**Figure 6.12**) appear well within the tissue zone. Thus, **Figure 6.14A** demonstrates the successful replication of tissues by overlapping the stress-strain curves of spinal cord, fetal membrane, and brain with corresponding LBL plastomers. Additionally, these materials closely match the adipose tissue found in breasts (**Figure 6.14B**), and highlights an avenue for future application by way of implantable breast implants. These solvent-free and mechanically invariant materials serve as a superior solution to commercially available silicone gel-based products that

leach into the body,[68,69] and which do not adequately mimic the mechanics of surrounding tissue.[27]

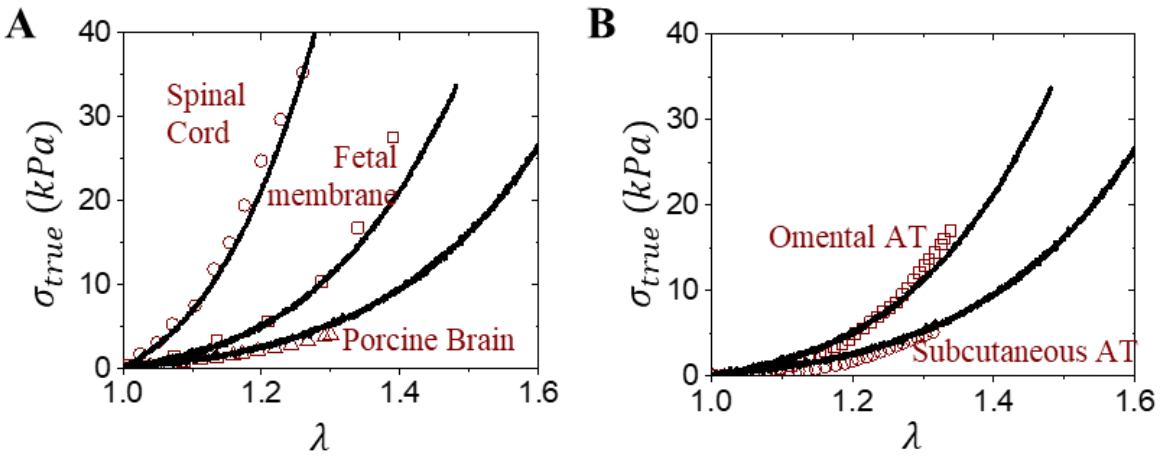

Figure 6.14: Mimicking tissue mechanics. (A) Selected true stress-strain curves of MCR-M17 LBL plastomers (lines) overlaid onto spinal cord,[70] fetal membrane,[7] and porcine brain[71] tissues (symbols) found in the literature with similar mechanical properties. **(B)** Selected true stress-strain curves of MCR-M17 LBL plastomers (lines) match different types of adipose tissue[72] (symbols).

The LBL platform also exhibits excellent biocompatibility as demonstrated by the adhesion and proliferation of human normal mammary epithelial and adipose-derived mesenchymal stem cells (MSCs) cultured onto an LBL plastomer surface with MCR-M17 brushes (**Figure 6.15**). Monitoring the cultured cells by fluorescence microscopy over the course of a week reveals plastomers as adequate substrates for both cell's viability and proliferation.[27]

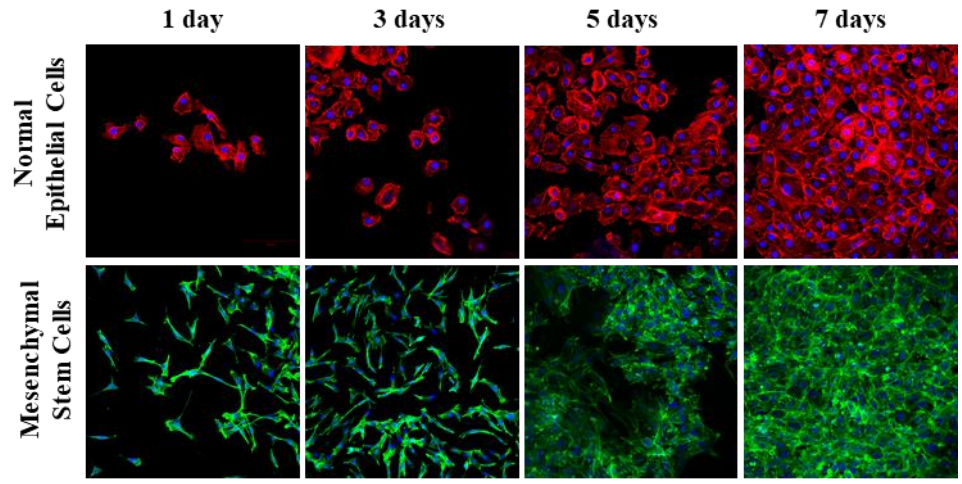

Figure 6.15: LBL plastomer biocompatibility. The proliferation of human normal mammary epithelial and adipose-derived mesenchymal stem cells cultured onto an LBL plastomer surface with MCR-M17 brushes and monitored by fluorescence microscopy after 1, 3, 5 and 7 days. Cells became confluent within 7 days.

In summary, the ability to replicate tissue elasticity is a relatively exciting triumph in its own right, but the larger achievement is a highly tunable synthetic platform that can access the entire elastic landscape. This platform empowers unprecedented combinations of softness and firmness that enable predictable stresses within given strains and represents a Pandora's box of mechanical properties for presently unrealized applications.

CHAPTER 7

SEQUENTIAL DEFORMATION HIERARCHY OF LBL PLASTOMERS

7.1 Introduction

The observed mechanical behaviors of the LBL plastomer platform is a manifestation of a two-phase deformation process, an *elastic regime*, which perfectly tracks with the elastic model, followed by a *yielding regime* (**Figure 7.1A**). Consequently, LBL plastomers exhibit a characteristic sigmoidal shape in differential modulus ($\partial\sigma_{true}/\partial\lambda$) curves (**Figure 7.1B**) that is strikingly similar to that of tissue (**Figure 1.2B**). Both of these observations suggest that LBL plastomers qualitatively mimic tissue's hierarchical deformation response. Therefore, the following sections aim to elucidate LBL plastomer mechanics through observations and characterization of LBL plastomers under deformation (**Section 7.2**) and a unifying theory for the hierarchical deformation response of LBL plastomers (**Section 7.3**).

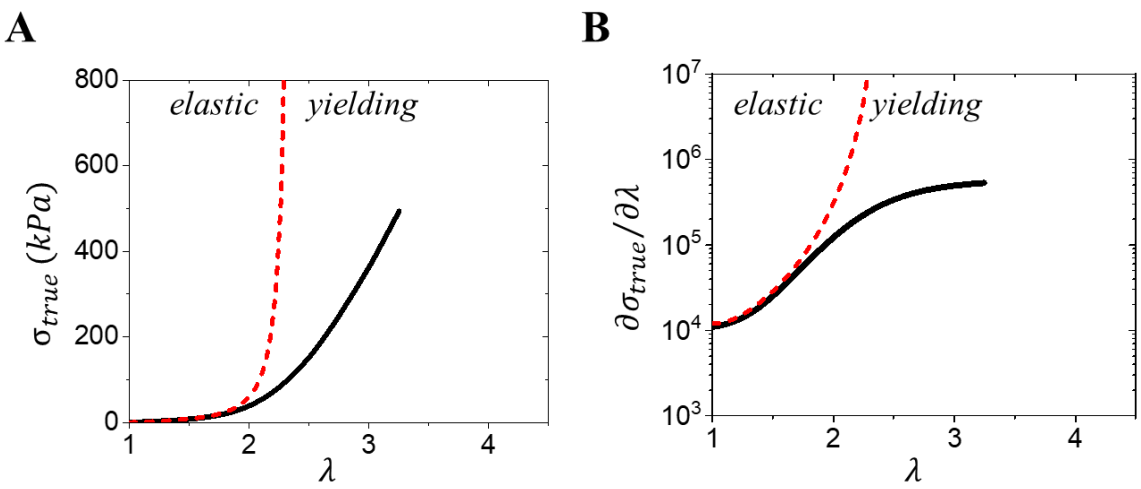

Figure 7.1: Elastic and yielding response of LBL plastomers. (A) A representative plastomer stress-strain curve (solid black) fit with the elastic model eq 2.3. The fitting curve (dashed red) shows excellent agreement in the elastic range and diverges from the experimental curve in the yielding range. **(B)** The corresponding differential modulus plot shows a reminiscent of sigmoidal shape of tissue.

7.2 Characterizing the Hierarchical Deformation Response

The molecular origin of the LBL plastomer platform's deformation response can be conveniently deciphered by coupling USAXS and stretching experiments. For instance, extension of the brush backbone is evidenced by low-q shifts of the d_3 spacing (**Figure 7.2A**), which exhibits a linear response with strain. Concurrently, deformation causes a high-q decrease of the d_1 spacing (**Figure 7.2B**), which indicates backbone extension given constant volume constraints of the cylindrical network strand filament. LBL plastomers with longer side chains experience a stronger dependence due to their enhanced firmness.[64]

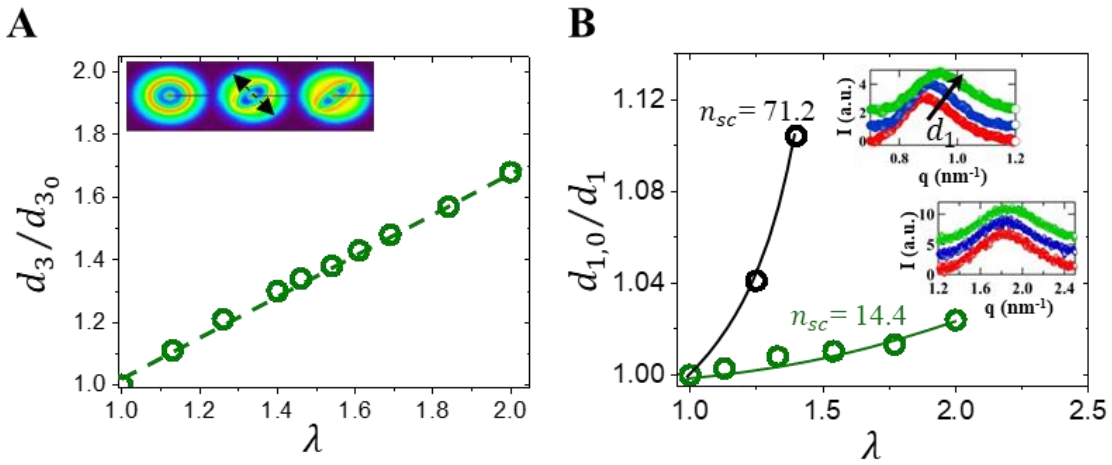

Figure 7.2: X-ray under deformation. (A) Uniaxial extension of an LBL plastomer results in increased d_3 obtained from in-situ variation of the structure factor $S(q)$ in the stretching direction (arrow in inset). Azimuthal variations in the 2D USAXS pattern suggest network topology restructuring during deformation. **(B)** Relative decrease of the d_1 spacing during elongation was deduced from the high-q shifts of the brush peak (insets) with pure MCR-M17 brushes exhibiting stronger dependence consistent with enhanced strand firmness.

In addition to backbone extension, a d_3 shift suggests eventual withdrawal of linear blocks from L-domains, which provides an explanation for the origin of the yielding regime. Potential linear withdrawal could be identified by variations of the d_2 peaks, yet no measurable evidence is observed likely due to the negligible size differential for withdrawing from domains; However, the yielding effect can be probed in additional mechanical experiments. For instance, the transition from the elastic to yielding phase can be mechanically probed via the emergence of both strain-rate dependence, and a hysteresis upon strain release. **Figure 7.3** probes the stress-strain response of an LBL plastomer at different strain-rates. Throughout the elastic phase, an invariance with strain-rate is observed as expected, but when approaching the theoretical yielding transition (~$0.5\lambda_{max}$), higher strain-rates lead to increased stress responses. Similar conclusions can be drawn from cyclic loading-unloading stress-strain cycles where straining throughout the elastic phase (~$0.5\lambda_{max}$) yields a perfectly elastic recoil (**Figure 7.4A**). However, at high strains the emergence of a small (<10%) hysteresis is observed with a quantifiable

hysteresis energy (**Figure 7.4B**). It is important to note that this yielding response does not lead to permanent plastic deformation as the initial mechanics are recovered given an appropriate time.

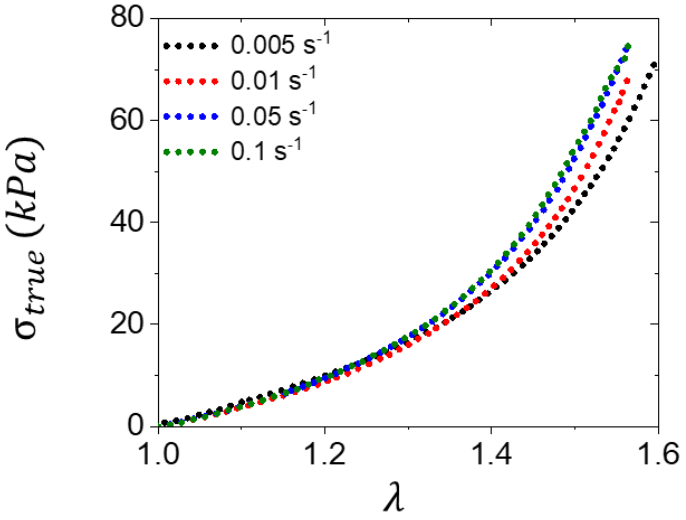

Figure 7.3: Strain-rate dependence. No strain-rate dependence was observed throughout the elastic regime (λ < 1.5) of deformation where fitting eq 2.3 applies. In contrast, stress increases with the strain rate in the yielding regime (λ > 1.5).

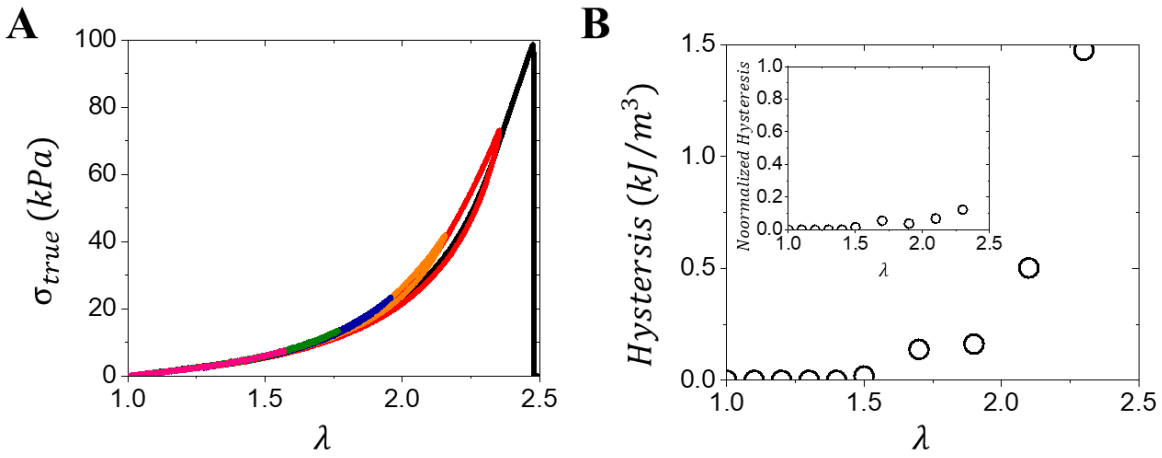

Figure 7.4: Hysteresis at large deformations. (A) Cyclic loading-unloading curves of an LBL plastomer to λ = 1.6 (pink), λ = 1.8 (green), λ = 2.0 (blue), λ = 2.2 (orange), λ = 2.4 (red) and to break (black) revealing the emergence of a hysteresis approximately at $0.5\lambda_{max}$. **(B)** Hysteresis energy as a function of elongation, inset: normalized hysteresis.

Furthermore, both deformation regimes of LBL plastomers were corroborated by simulations (**Figure 7.5**),[61,73] which found that network deformation is first supported by the elongation of the brush strands with linear domains acting as classical multifunctional crosslinks. The yielding regime only emerges when the forces generated in brush strands become greater than the enthalpic penalty of pulling linear chains from domains into the brush matrix and forming additional linear-brush interfaces (**Figure 7.5**).[27,61,73] Upon meeting this threshold, additional extension requires constant force thereby causing a linear stress-strain relationship throughout the yielding phase.

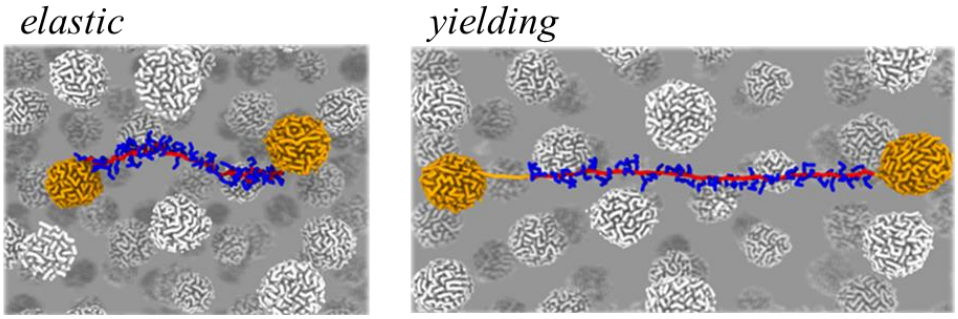

Figure 7.5: Computer simulations of elastic and yielding responses. Illustration of the different network deformation regimes. Elastic deformation of the brush backbone (red) with side chains (blue) that connect domains (yellow) and subsequent pulling of linear blocks out of domains during yielding.

7.3 Conclusion

In summary, LBL plastomers prove to be a resourceful scaffold given the hierarchical integration of molecular and particulate motifs within each network strand, which activate under different stresses (**Figure 7.6**). On a mesoscopic scale, brush strands behave as relatively flexible filaments that exhibit low bending rigidity and unfold at lower forces (*I*) imparting softness. This is followed by stretching of the brush backbone (*II*) responsible for the material's firmness, which is enhanced by the side chain length (**Chapter 6**). Lastly, sufficient forces enable

concomitant withdrawal of linear chains from domains (*III*). Critically, these linear blocks serve as hidden length reservoirs[74] that offset the limited extensibility of the inherently strained brush strands while also mitigating uneven stress distributions. This hierarchical organization empowers telescoping activation of deformation mechanisms responsible for the soft-to-firm transition, which qualitatively mimics the sequential unfolding, stretching, and yielding of microfibrils in collagen (**Chapter 1**).[11]

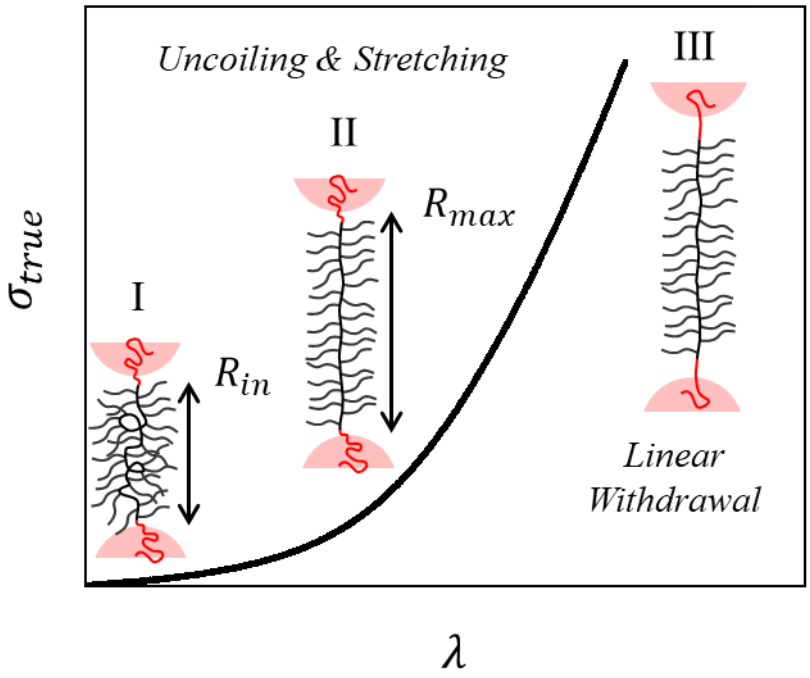

Figure 7.6: A unified theory for the hierarchical deformation of LBL plastomers. A cascade of deformation mechanisms during uniaxial extension of LBL networks provides their unique tissue-mimetic mechanical response: (*I*) unfolding of brush filaments, (*II*) stretching of backbones inside brush envelops, and (*III*) pulling linear chains from microdomains creating a new interface between exposed linear block sections and the brush matrix.

CHAPTER 8

SIDE CHAIN ARRANGEMENT: ADDITIONAL LESSONS LEARNED

8.1 Introduction

The successful demonstration of tunable firmness by programming side chain mixtures into network strands (**Chapter 6**) introduces a plethora of questions regarding the role of side chain arrangement within LBL plastomer networks. The boundaries of this inquiry are investigated and monitored by their effect on the resulting mechanical properties. Distinct side chain arrangements (**Figure 8.1**) include a brush-star transition (**Section 8.2**), brush impurities in LBL networks (**Section 8.3**), distinct pentablock $LB_1B_2B_1L$ networks (**Section 8.4**) and finally mixtures of brush strands with different n_{sc} in LBL networks (**Section 8.5**).

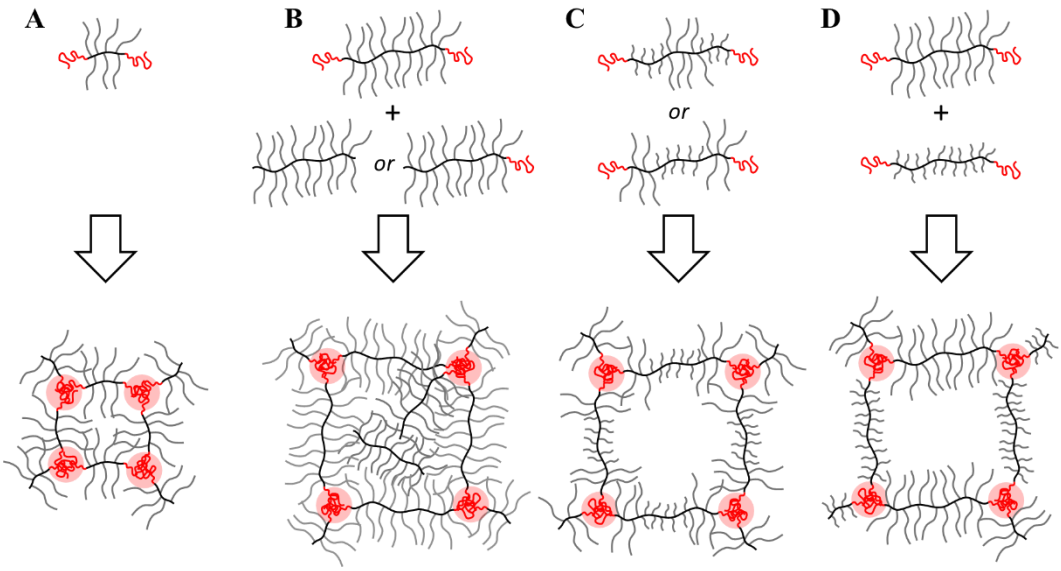

Figure 8.1: Different side chain arrangements. (A) Star-like transitions **(B)** Introduced LBL impurities **(C)** Pentablock $LB_1B_2B_1L$ plastomers **(D)** Self assembled mixtures of distinct brush strands.

8.2 Brush-Star Transition

The first realization of the importance of side chain arrangement naturally emerged from tuning architectural parameters of LBL plastomers encoded with long MCR-M17 side chains. As previously discussed, LBL plastomers synthesized with $n_{bb} \gg n_{sc}$, such as those found in **Figure 6.12** where n_{bb} = 300, 450 and n_{sc} = 71.4, coalesce and behave predictably within the overarching rules governing the LBL platform (**Section 6.3**). Yet the use of these long side chains presents a unique scenario where side chains are on length scales of the brush backbone ($n_{bb} \cong n_{sc}$). This previously unrealized case is typically irrelevant in MCR-M11 based LBL plastomers where n_{bb} is always significantly greater than n_{sc} = 14.4. The consequence of this realization is the formation of star-like strands, and although brush-star transitions are well documented in the literature,[47,75] discussion of the transition's effect on the resulting mechanical properties of networks is absent. Indeed, growing MCR-M17 brushes with n_{bb} = 100 (**Figure 8.2A**) yields deformation responses inconsistent with those presented in **Chapter 6**, which becomes more pronounced when delving well past the transition boundary with n_{bb} = 33 (**Figure 8.2B**).

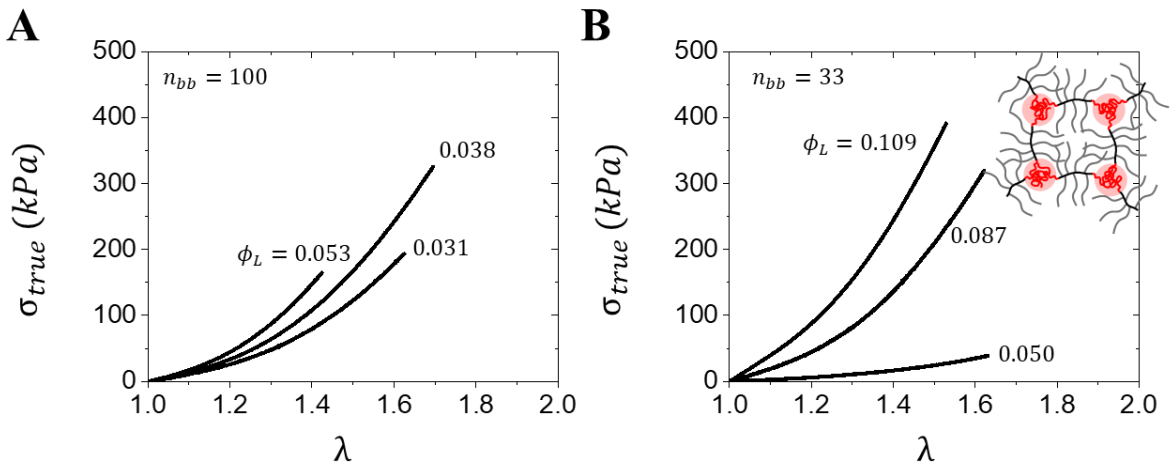

Figure 8.2: Stress-strain of star-like MCR-M17 LBL plastomers. (A) n_{bb} = 100 **(B)** n_{bb} = 33

Extracted elastic parameters overlaid on the LBL platform [E_0, β] map highlight the distinct mechanical response of these star architectures (**Figure 8.3**). Although the n_{bb} = 100 series behaves in a similar vein to the overarching platform, the n_{bb} = 33 series behaves vastly different and indicates a complete transition to the star-like arrangement. The reason for their distinct mechanical response is not fully understood, but is likely a product of a unique self-assembly pathway. Regardless, both self-consistent series violate the coalescence trend of the LBL platform, which serves as an additional tunable avenue given a fixed n_{sc}.

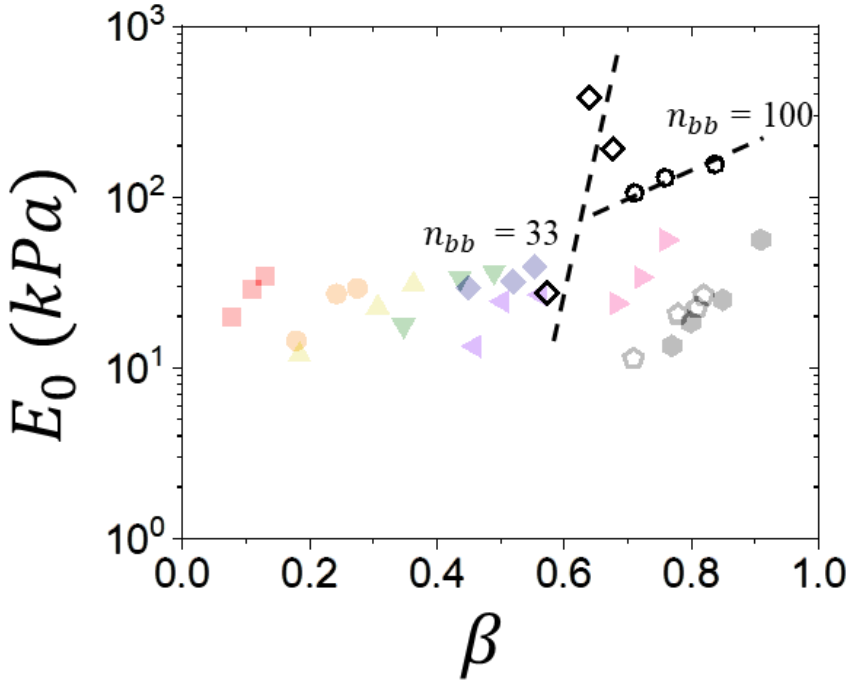

Figure 8.3: The brush-star transition on the elastic landscape. An [E_0,β] map showing LBL plastomers with n_{sc} = 71.2 and n_{bb} = 100 (black circles) and n_{bb} = 33 (black diamonds) in relation to various random brush LBL's highlighted in **Figure 6.12**. The n_{bb} = 100 series breaks the coalescence trend as a result of a brush-star transition further exemplified in the n_{bb} =33 series, which shares no similar trend with the overarching LBL platform.

8.3 LBL Brush Impurities

All tissue types exhibit a varied mechanical response depending on external factors such as bodily location, and age. Therefore, to demonstrate the additional tunability of the LBL platform to meet these variations without changing the underlying architectural parameters, simple mixing techniques of brush-based additives can be employed. Here, side chains in free brushes no longer bound to the LBL structure, can still provide desired effects. For instance, mixing LBL plastomer networks with their precursor B brush leads to noticeable changes in softness while largely maintaining the firmness (**Figure 8.4**).

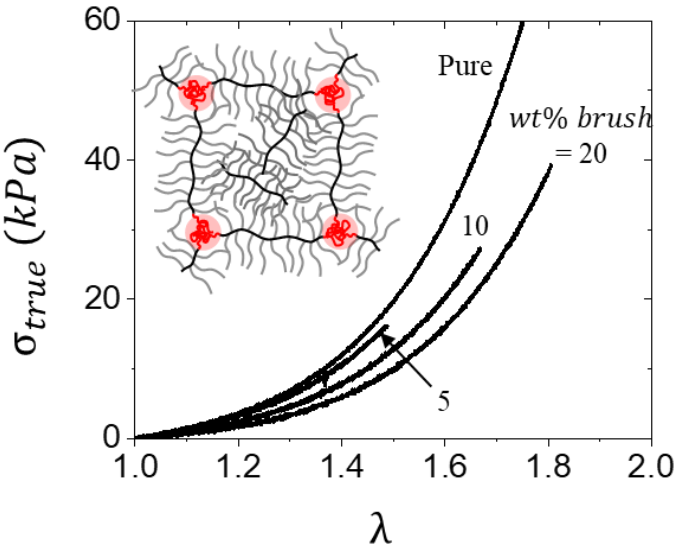

Figure 8.4: Stress-strain of LBL plastomers with brush impurities. A pure LBL plastomer diluted with different weight fractions of corresponding brush during film preparation.

This result suggests a single LBL network can be additively altered to provide limited elastic mobility without the laborious synthesis of programming distinct architectural parameters to achieve the same effect. The resulting elastic parameters are overlaid on the $[E_0, \beta]$ map in **Figure 8.5**, showing remarkable mechanical variation from just 10-20% impurity by weight. However, the method of mixing, which requires casting premade mixtures of LBL plastomers and brushes, likely affects the self-assembly process. This is distinct from traditional swelling experiments where a diluent swells premade films (i.e. gels in **Section 3.4**), which is almost certainly impossible to accomplish with macromolecular brushes. Indeed, this distinction necessitates future research, specifically investigating the effect of the brush impurity dimensions on the self-assembly pathway of casted premade mixtures. For instance, macromonomer diluents (n_{bb}= 1) and brush diluents (n_{bb}= n_{bb} of the LBL) will likely result in different mechanical properties.

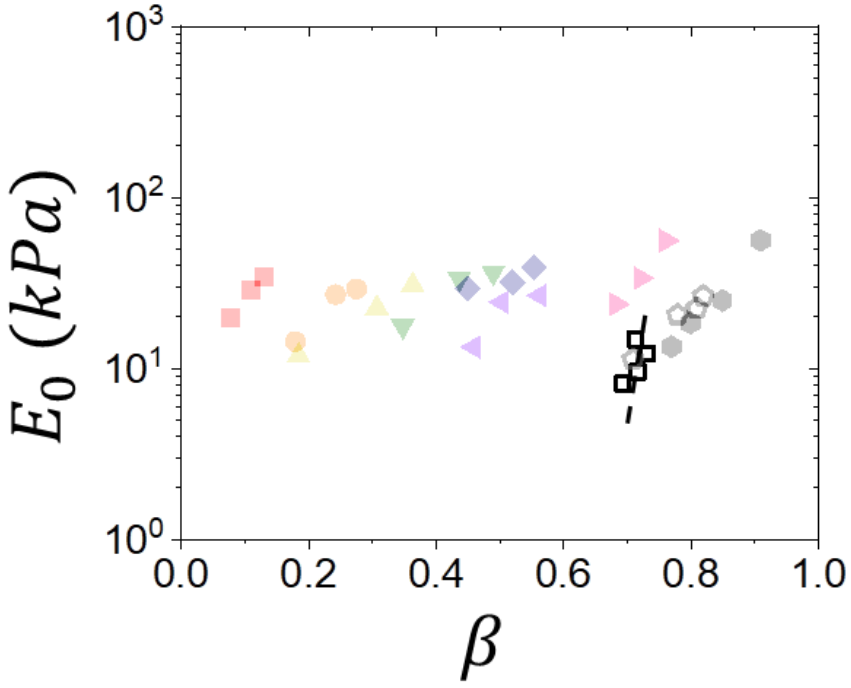

Figure 8.5: LBL plastomers with brush impurities on the elastic landscape. An [E_0,β] map showing LBL plastomers diluted with free corresponding brushes in relation to various random brush LBL's highlighted in **Figure 6.12**. The trend agrees with initial predictions that free brush blocks dilute network with minimally changing firmness.

8.4 Pentablock $LB_1B_2B_1L$ Plastomers

To reinforce the validity of mixing side chain lengths within a given strand (**Chapter 6**), two edge cases can be identified - $LB_1B_2B_1L$ pentablock plastomers where B_1 and B_2 are sequentially synthesized with either pure MCR-M11(n_{sc} =14.4) or MCR-M17 (n_{sc} = 71.2) side chains and vice versa. To this end, two $LB_1B_2B_1L$ pentablock plastomers with inverted side chains were grown (**Figures 8.6** and **8.7**) to have similar effective n_{sc} to an analogous random comonomer mixture (**Section 6.2**). The challenge of this approach is ensuing the accuracy of the sequential brush steps to achieve the appropriate average n_{sc} as B_1 growth uses the same peak positions as the macroinitiator B_2. However, carefully measuring added B_2 brush and B_1

macromonomer assists ^{1}H-NMR to appropriately quantify the resulting n_{sc} as described in **Figures 8.6** and **8.7**. Fortunately, the LBL platform is forgiving towards both n_{bb} and ϕ_L as their variation do not radically affect the position of coalescence on an [E_0, β] map (**Section 6.3**). Therefore, outside of n_{sc}, it is not necessary for the resulting pentablocks to be identical in order to demonstrate the effect of side chain arrangement, as is the case for the two presently programmed pentablocks.

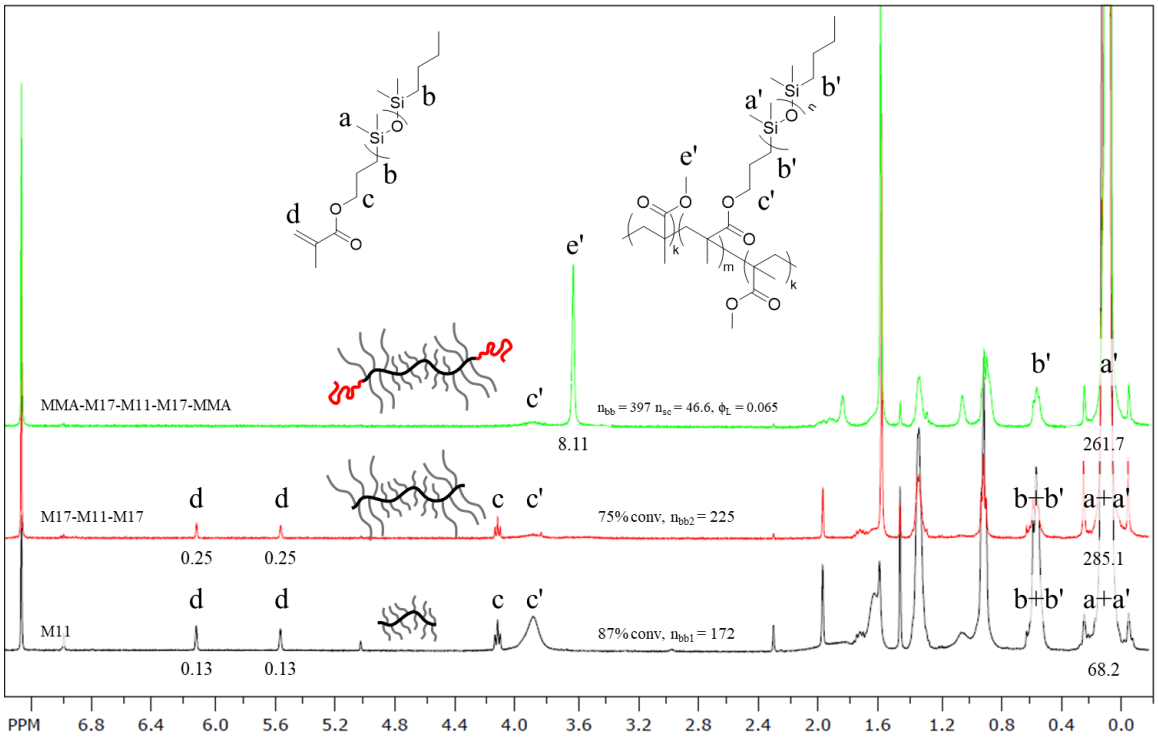

Figure 8.6: ^{1}H-NMR growth of LB$_1$B$_2$B$_1$L MMA-M17-M11-M17-MMA pentablocks. Each ^{1}H-NMR trace shows unpurified stages of each brush addition and final purified triblock to achieve analogous n_{sc} materials to a randomly mixed MCR-M11/MCR-M17 25/75 brush (400 MHz, $CDCl_3$): 6.12, 5.56 (C**H$_2$**=C(CH$_3$)C=O, unreacted macromonomer, s, 1H), 4.12 (CO-OC**H$_2$**-, unreacted macromonomer, t, 2H), 3.91 (CO-OC**H$_2$**-, PDMS brush, m, 2H), 3.62 (COO-C**H$_3$**, linear MMA, s, 3H), 0.55 (-CH$_2$-(Si(CH$_3$)$_2$-O)$_n$-C**H$_2$**-CH$_2$-, m, 2H) 0.09 (-Si(C**H$_3$**)$_2$-, s). n_{bb1} = [area(a'+a)/68.4-area(d)/1]/[area(a'+a)/68.4]∗[PDMS$_{MCR\text{-}M11}$]/[I]. n_{bb2}= [area(a'+a)/285.1-area(d)/1]/[area(a'+a)/285.1] *[PDMS$_{MCR\text{-}M17}$]/[PDMS$_{MCR\text{-}M11\text{-}brush}$], note that the amount of PDMS H is calculated from added MCR-M17 to afford comparable n_{sc} of mixed MCR-M11/MCR-M17 25/75 brush series at 75% conversion. n_L= [area(e')/3]/[area(a')/261.7]* n_{bb}, where n_{bb}= n_{bb1}+n_{bb2}. Note that between each growth step, purification of residual macromonomer was performed.

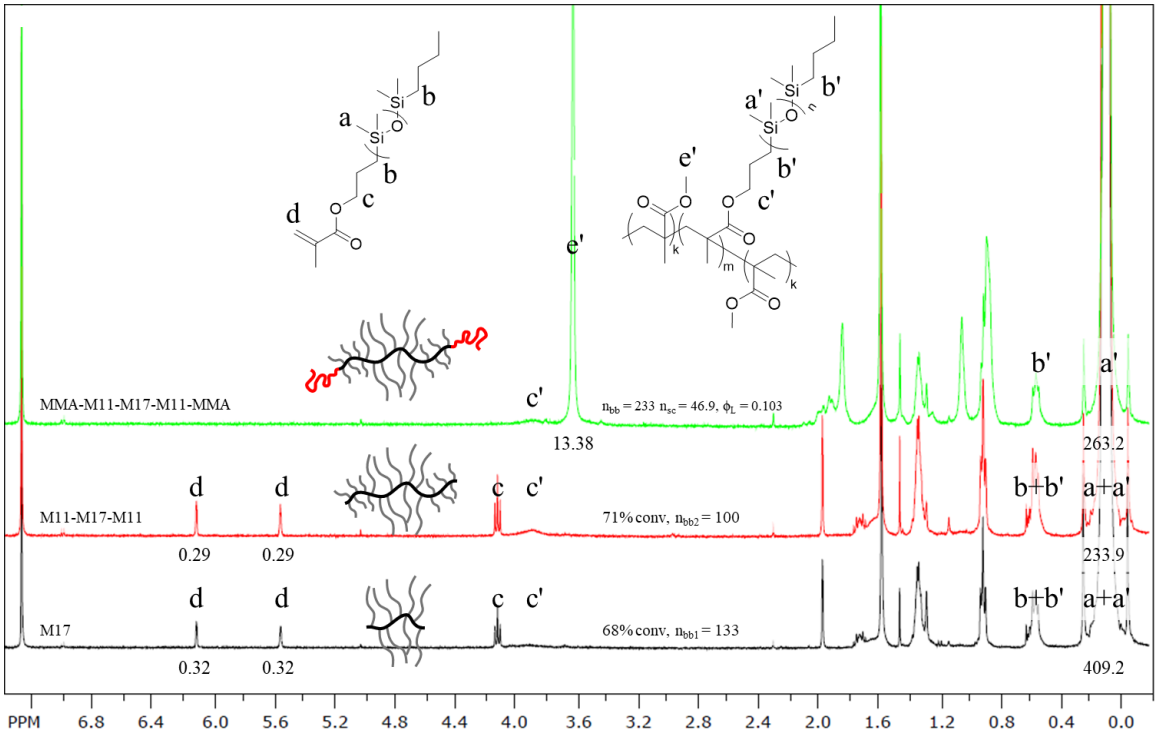

Figure 8.7: ^{1}H-NMR growth of LB$_1$B$_2$B$_1$L MMA-M11-M17-M11-MMA pentablock. ^{1}H-NMR trace shows unpurified stages of each brush addition and final purified triblock to achieve analogous n_{sc} materials to a randomly mixed MCR-M11/MCR-M17 25/75 brush (400 MHz, $CDCl_3$): 6.12, 5.56 (C**H$_2$**=C(CH_3)C=O, unreacted macromonomer, s, 1H), 4.12 (CO-OC**H$_2$**-, unreacted macromonomer, t, 2H), 3.91 (CO-OC**H$_2$**-, PDMS brush, m, 2H), 3.62 (COO-C**H$_3$**, linear MMA, s, 3H), 0.55 (-CH_2-($Si(CH_3)_2$-O)$_n$-C**H$_2$**-CH_2-, m, 2H) 0.09 (-Si(C**H$_3$**)$_2$-, s). n_{bb1} = [area(a'+a)/409.2-area(d)/1]/[area(a'+a)/409.2]∗[PDMS$_{MCR-M17}$]/[I]. n_{bb2}= [area(a'+a)/233.9-area(d)/1]/[area(a'+a)/233.9] *[PDMS$_{MCR-M11}$]/[PDMS$_{MCR-M17-brush}$], note that the amount of PDMS H is calculated from added MCR-M11 to afford comparable n_{sc} of mixed MCR-M11/MCR-M17 25/75 brush series at 75% conversion. n_L= [area(e')/3]/[area(a')/263.2]*n_{bb}, where n_{bb}= n_{bb1}+n_{bb2}. Note that between each growth step, purification of residual macromonomer was performed.

The resulting mechanical properties of these materials (**Figure 8.8**) are reasonable, given the programmed n_{sc} and the difference in ϕ_L. A few observations may be drawn from their extracted elastic properties as overlaid on the [E_0, β] map (**Figure 8.9**). First, although having different n_{bb} and ϕ_L, these pentablocks show an agreeable coalescence consistent with the overarching LBL platform as described in **Chapters 5** and **6**. Second, their absolute position on

the $[E_0, \beta]$ map is relatively consistent within the LBL framework as they are programmed to match n_{sc} = 47.1 of random mixed brushes (pink right triangles). The observed coalescence shift further suggests the n_{sc} quantification developed by ^{1}H-NMR (**Section 5.2**) may be inaccurate as pentablocks are precisely characterized through each sequential growth step. Therefore, it is possible all random comonomer mixtures (**Chapter 6**) have higher n_{sc} then calculated and requires further investigation. Regardless, both of the above observations suggest a powerful conclusion: the arrangement of side chain mixtures programmed into a network strand is inconsequential, and only the average n_{sc} over the entire strand dictates the resulting mechanical footprint on the $[E_0, \beta]$ map.

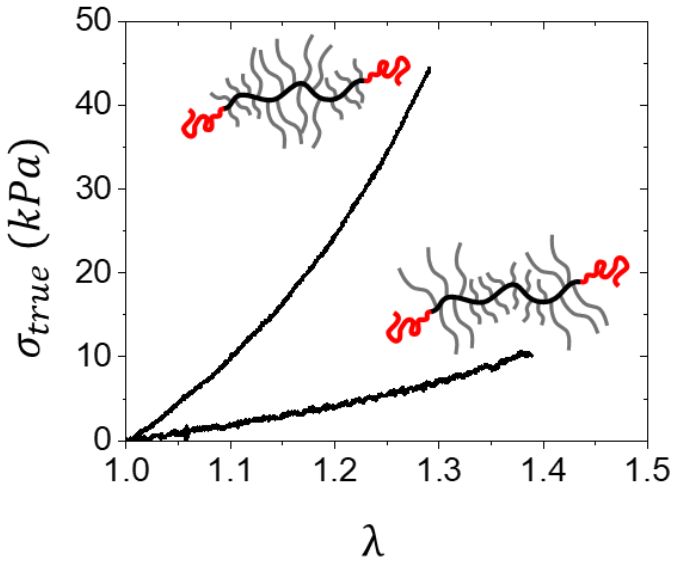

Figure 8.8: Stress-strain responses of LB$_1$B$_2$B$_1$L pentablock plastomers. M11-M17-M11 based pentablock plastomer (top) and M17-M11-M17 based pentablock plastomer (bottom).

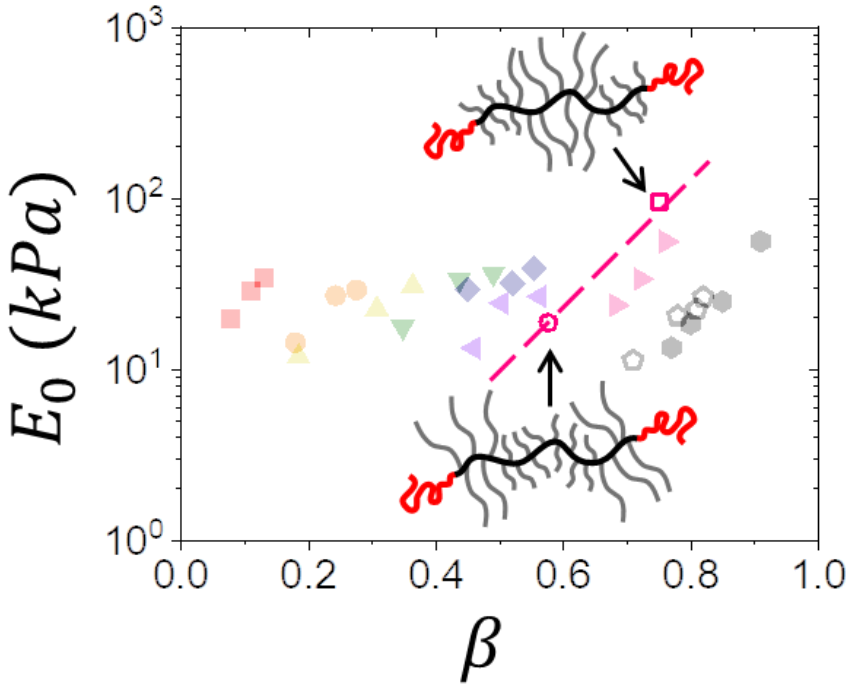

Figure 8.9: LB$_1$B$_2$B$_1$L pentablock plastomers on the elastic landscape. An [E_0,β] map showing M11-M17-M11 based plastomer (open pink square) and M17-M11-M17 based plastomer (open pink circle) designed to match random brush series n_{sc} = 47.1 (pink triangles) in relation to various random brush LBL's highlighted in **Figure 6.12**.

This is a rather interesting conclusion as it has powerful implications for both the understanding of L-B phase separated interface and L block growth kinetics. For instance, it is expected that longer side chains near the L-B interface have a higher driving force for phase separation resulting in enhanced firmness, yet this is inconsistent with the conclusions presented here. Additionally, it is expected that growth kinetics of L blocks from an interface of longer side chains would be hindered in relation to shorter side chains. Therefore, the conclusions presented here could be exploited to assist future industrial LBL scale-up without affecting the resulting mechanical properties. Nevertheless, future kinetic studies and comprehensive pentablock series should be pursued.

8.5 Strand Mixtures

The self-assembled nature of the LBL platform also permits combination of well-defined strands with different stiffness. Therefore, a natural iteration is investigating whether the relationships established for side chain mixtures encoded into individual network strands (**Sections 6.3** and**8.4**) extend to networks of mixed strands with distinct side chains. It is important to note that probing this arrangement is unique to the self-assembled nature of the LBL platform. First, the arrangement is explored in solutions of brush strand mixtures (**Figure 8.10A-C**) with either identical n_{sc} = 14.4 (**Figure 8.10A**), similar n_{bb} = 300 (**Figure 8.10B**) or similar strand mass (**Figure 8.10C**). In cases of strand mixtures with different n_{sc} (**Figure 8.10B,C**), clear immiscibility is observed with visibly well-defined phase separated droplets emerging after a set period of time (**Figure 8.10D**). To reiterate, these brushes are identical in chemistry, but only differ in their local *stiffness*.

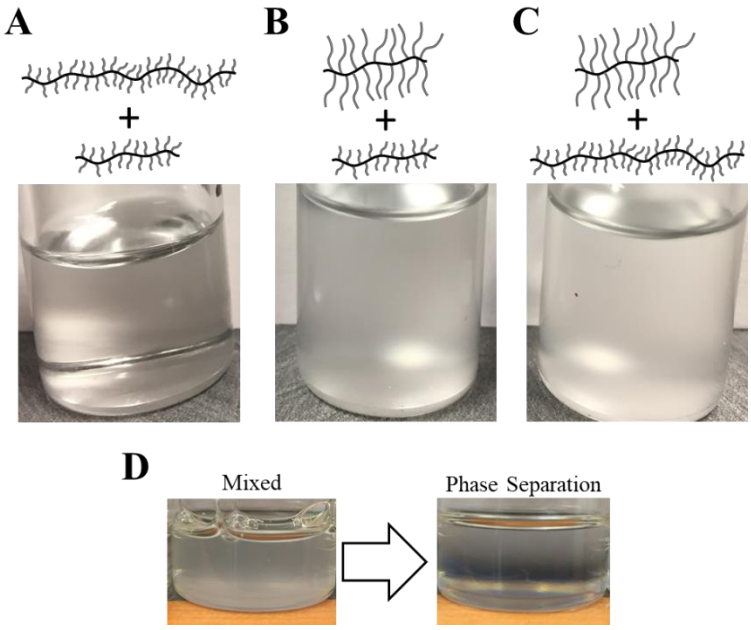

Figure 8.10: Mixing brushes with different architectural parameters. (A) Brushes with identical side chain length n_{sc} = 14.4 and different n_{bb} = 300, 1500 form a completely clear and miscible mixture. **(B)** Two brushes of similar length n_{bb} = 300 and different n_{sc} = 14.4, 71.2

for a poorly miscible and opaque mixture. **(C)** Two brushes of similar mass distinctly encoded with n_{bb} = 300 & n_{sc} = 71.2 and n_{bb} = 1500 & n_{sc} = 14.4 form a poorly miscible and opaque mixture. **(D)** Poorly miscible strands in **B, C** unmix over time (~1 day) to yield phase separated droplets.

Setting aside this intriguing observation, LBL plastomers programmed with different brush stiffnesses can be mixed to provide average network n_{sc} matching the final achieved n_{sc} of random mixed brushes (**Section 6.2**). The resulting mechanical properties (**Figure 8.11**) are inconsistent with expectations as the programmed n_{sc} = 71.2, 47.1 and 33.8 mixtures provide largely identical mechanical responses, which is starkly distinct from the mechanical responses observed in random mixed brushes in **Figure 6.11A**. The resulting extracted elastic parameters also distinctly emerge on the [E_0, β] map relative to their theoretical molar counterparts programmed into individual strands (similar colored symbols **Figure 8.12**). This observation suggests these materials behave under a different mechanical model reminiscent of a composite, which could have significant consequences to warrant further study.

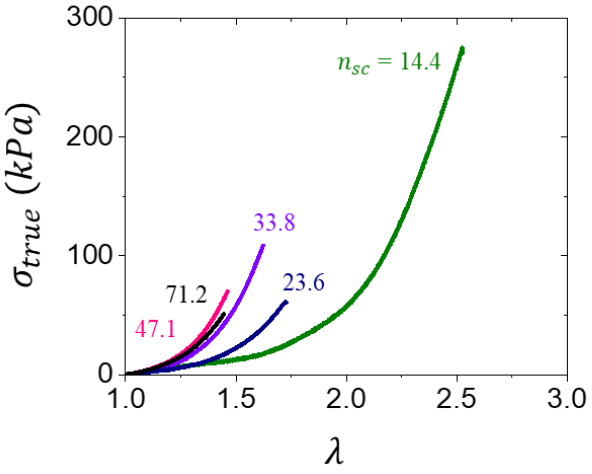

Figure 8.11: Stress-strain responses of LBL plastomers with strand mixtures. The mixtures were programmed to replicate average n_{sc} of LBL plastomers with random side chains encoded into brushes.

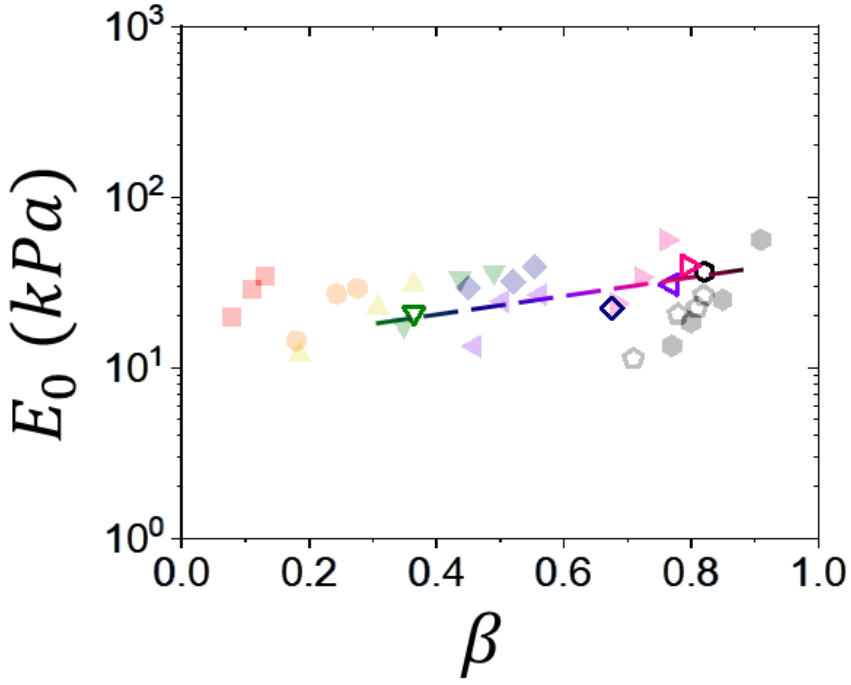

Figure 8.12: LBL plastomer strand mixtures on the elastic landscape. An [E_0,β] map showing mixed n_{sc} =14.4 (green) and n_{sc} = 71.2 (black) in different ratios to afford analogous n_{sc} to random brush LBL's highlighted in **Figure 6.12** where n_{sc} = 23.6 (blue), n_{sc} = 33.8 (purple), n_{sc} = 47.1 (pink).

8.6 Conclusion

Combining all of the probed side chain arrangements described in this chapter onto an [E_0, B] map (**Figure 8.13**) paints a clear image: the boundaries and potential of the LBL plastomer platform are still ill-defined. Fully understanding the effects of side chain arrangement represents more than simple scientific inquiry, but rather can be exploited to empower other functions relevant to industry and other scientific pursuits such as: (i) controlling LBL plastomer self-assembly for distinct coloration, (ii) simplifying the laborious synthesis required to attain specific mechanical properties and streamline future industrial scale-up efforts and (iii) assisting

the design of future mechanochemistry[76] applications where highly strained brushes can serve to deliver tailored stresses to mechanophores.

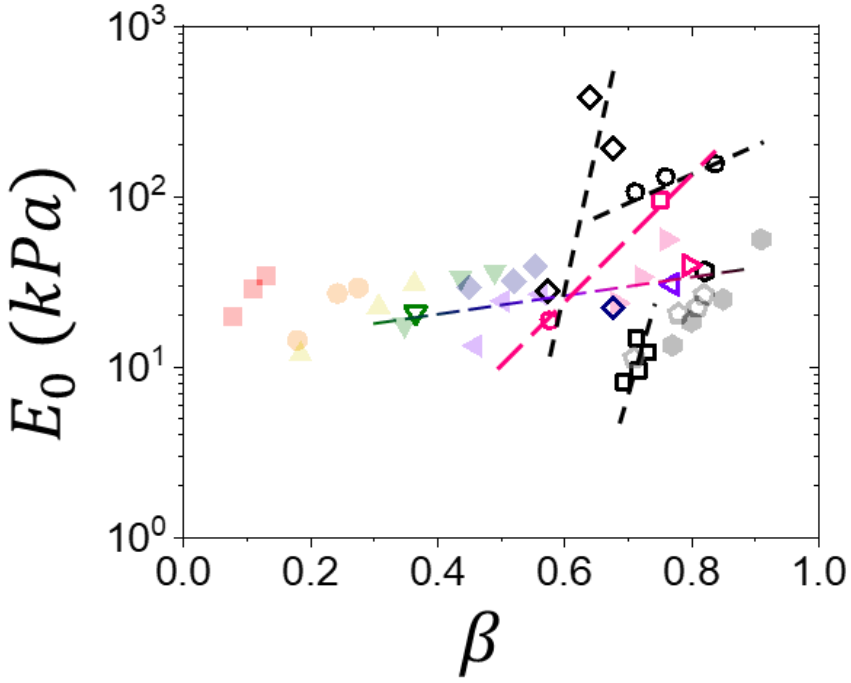

Figure 8.13: Different LBL plastomer side chain arrangements on the elastic landscape. An [E_0,β] map showing a summary of all studied conformations of star-like transition (**Figure 8.3**), free brush mixtures (**Figure 8.5**), pentablock plastomers (**Figure 8.9**) and strand mixtures (**Figure 8.12**) in relation to various random brush LBL's highlighted in **Figure 6.12**.

CHAPTER 9
FUTURE WORK AND CONCLDUING REMARKS

9.1 Introduction

Not only does the linear-brush-linear (LBL) self-assembled platform enable materials with unprecedented elastic control through a hierarchical deformation cascade, the LBL scaffold also permits integrating additional desired functionalities and properties. For instance, the following sections propose exploring additional L-block chemistries to allow LBL thermoforming (**Section 9.2**), decoupling material strength to traverse the entire mechanical landscape (**Section 9.3**), and encoding side chains with complex functionality (**Section 9.4**), all while maintaining the LBL platform's unique elastic properties. It is important to note that this chapter is highly speculative with minimal supporting data and instead serves as a foundation for future research.

9.2 Thermoforming LBL plastomers

All LBL plastomers reported in this dissertation have been self-assembled into films casting from large amounts of solvent. Although this procedure is acceptable in the vacuum of a scientific setting, it is neither a scalable procedure nor permits molding complex objects. In contrast, industrial strategies typically mold materials without solvent through the use of thermoforming or injection molding. Fortunately, the nature of the LBL physical network theoretically translates to these methods, however, LBL plastomers described in this dissertation

are mechanically stable well past the glass transition of the PMMA (T_g = 105°C) L-block domains as demonstrated by oscillation of an LBL plastomer at different temperatures (**Figure 9.1A)**. This dynamic test is accompanied by tensile tests within the elastic regime at different temperatures surrounding the T_g of PMMA (**Figure 9.1B**), which show almost identical deformation responses. This nonideal result is likely a consequence of the well-known order-disorder transition observed in block copolymers,[77-79] which require elevated temperatures to enable mixing of the chemically immiscible blocks to flow. Therefore, LBL plastomers must face similar requirements and is likely enhanced by the distinct architecture of each block.

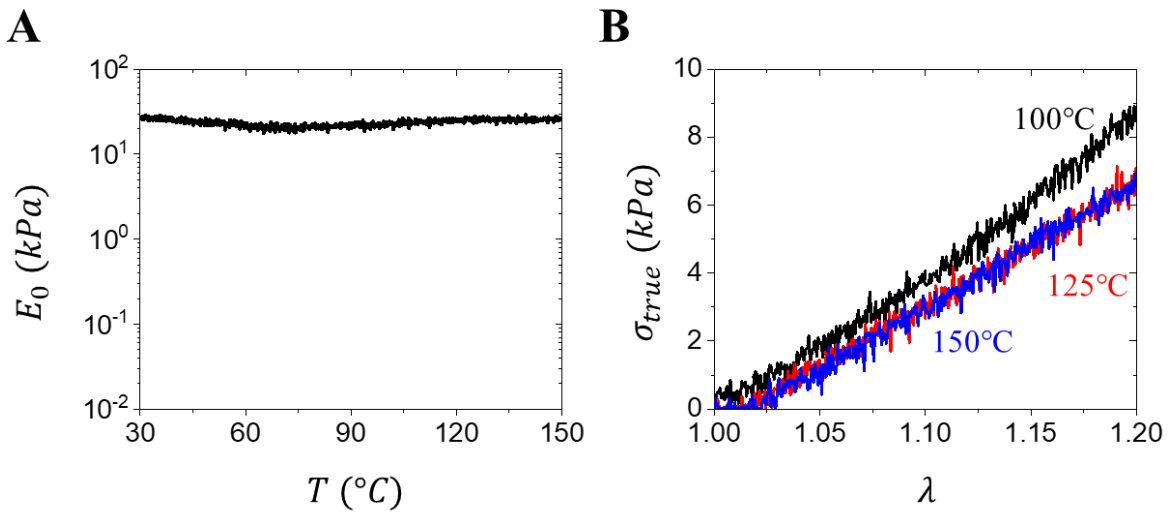

Figure 9.1: LBL plastomer thermal stability. (A) Softness over a thermal ramp of an LBL plastomer above L-block glass transition (T_g = 105°C) via 5% strain oscillation experiment. **(B)** Short stress-strain curves of an LBL plastomer at different temperatures below and above L-block glass transition. Samples were deformed well within the elasticity boundary before L-block yielding.

To this end, tuning L block chemistry can be selected to lower either the T_g or the solubility parameter (δ) gap to induce the order-disorder transition. The deformation response has been measured of a preliminary set of LBL plastomers synthesized with a PDMS (δ = 15.3

MPa$^{0.5}$) brush block and different methacrylate-based L blocks including *tert*-butyl methacrylate (T_g = 116 °C, δ = 17.1 MPa$^{0.5}$), isopropyl methacrylate (T_g = 83 °C, δ = 18.0 MPa$^{0.5}$) and benzyl methacrylate (T_g = 54 °C, δ = 20.3 MPa$^{0.5}$) (**Figure 9.2**). These materials have been programmed with similar architectural parameters (ϕ_L) and show a remarkably similar deformation response, which highlights the potential to decouple mechanics and thermal processability. It is important to note that other distinct chemistries are applicable outside of methacrylates or acrylates through brush chain end functionalization. Regardless, this is important preliminary data that warrants further investigation as architectural contributions of LBL triblocks on the order-disorder transition has not fully been described and may permit L-blocks with T_g well below room temperature. Such research along with other approaches in triggering self-assembly are essential for molding and 3D-printing in industry.

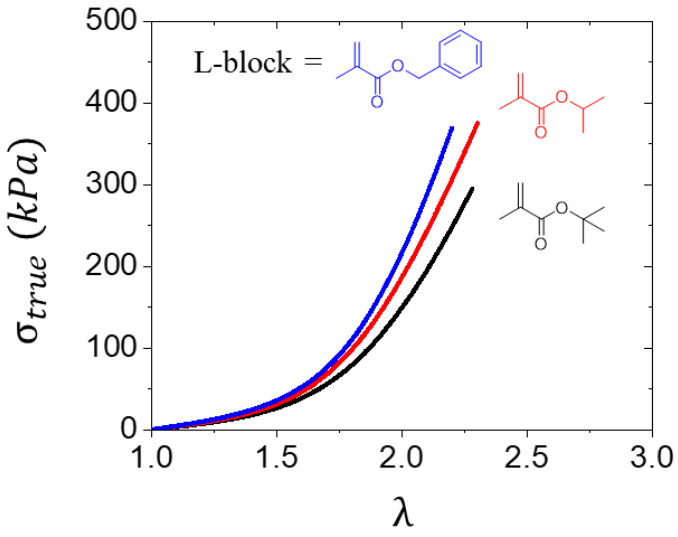

Figure 9.2: Stress-strain responses of LBL plastomers with distinct L-block chemistry. Different L-blocks were grown from an architecturally identical brush to a similar ϕ_L = 0.13, benzyl methacrylate (blue), isopropyl methacrylate (red), *tert*-butyl methacrylate (black).

9.3 Decoupling Strength with Graft Copolymers

The central goal of this dissertation is the pursuit of mimicking tissue's elastic properties and subsequent coverage of the entire elastic landscape. However, elasticity is not the only mechanical process of interest as both tissues and LBL plastomers contain a yielding regime (**Sections 1.2** and **7.2**). Yielding holds significant importance as it imparts highly strained and firm materials with added strength and extensibility unattainable by pure elastic systems, as the large strain features are inherently coupled to elasticity as described by equation 2.3 in **Section 2.2** and demonstrated in **Figure 2.4**. Comparison between the strength of tissue and LBL plastomers in a 3D softness-firmness-strength plot (**Figure 9.3**) paints an interesting picture. Although this dissertation has shown LBL plastomers can mimic tissue elasticity, their strengths are often magnitudes less than corresponding tissue. Specifically, LBL plastomers suffer in strength due to their enhanced firmness and weakly compensating yielding responses. Therefore, the next logical step is to iterate upon the LBL hierarchical platform to enable traversing the entire *mechanical* landscape, which consists of softness, firmness and strength (**Figure 9.3**).

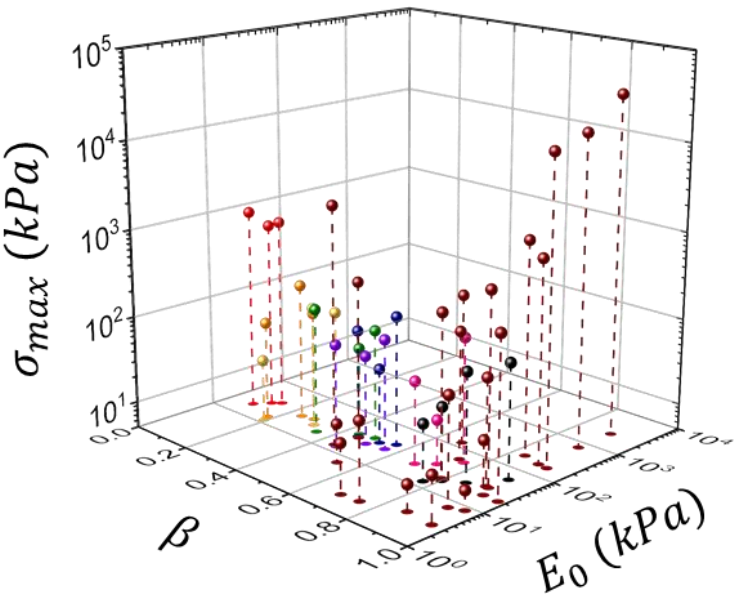

Figure 9.3: Highlighting tissue's strength. A [E_0,β,σ_{max}] 3-D map showing selected tissue mechanical parameters in relation to the LBL plastomer platform highlighted in **Figure 6.12**. Although the LBL plastomer platform can achieve broad elastic control (in the xy plane), tissue strength (dark red) remains an elusive parameter. Attaining independent control of softness (E_0), firmness (β) and strength (σ_{max}) will enable traversing the entire mechanical landscape.

The proposed challenge is highly nontrivial, but a reasonable suggestion is to embed the LBL structure as a repeat unit in to a larger scaffold (**Figure 9.4**). This thought experiment leverages two key assumptions: (i) preserving the LBL repeat unit will largely maintain control over the strand conformation, which dictates the elastic properties and (ii) the increased number of side chains that phase separate into distinct domains will resist both network fracture and crack propagation as a single L-block withdrawal will not render the entire strand mechanically inactive. Therefore, increased forces are required to remove an entire macromolecule from the network, which will impart enhanced strength. This graft copolymer platform maintains the LBL architectural parameters of side chain length (n_{sc}), strand brush length (n_{bb}), phase separating

side chain length (n_L) and volume fraction (ϕ_L), but also introduces total strand length (n_s) and the number of LBL repeat units ($n_r = n_s/n_{bb}$). Although this thought experiment promises a highly tunable platform, the synthetic reality of achieving this goal is challenging. For instance, attempted copolymerization of any chemically distinct end functionalized macromonomers (i.e. PMMA and PDMS) will inevitably lead to immediate immiscibility. Sequential polymerization approaches may be necessary such as grafting through copolymerization of macromonomers (PDMS) and monomers that can then enable subsequent growth of the second polymer (PMMA). Therefore, this will require orthogonal controlled radical polymerization methods such as ATRP and reversible atom fragmentation technique (RAFT). Significant effort will be necessary to carefully characterize each step and the resulting encoded parameters, but success represents the next thrust area for brush-based materials.

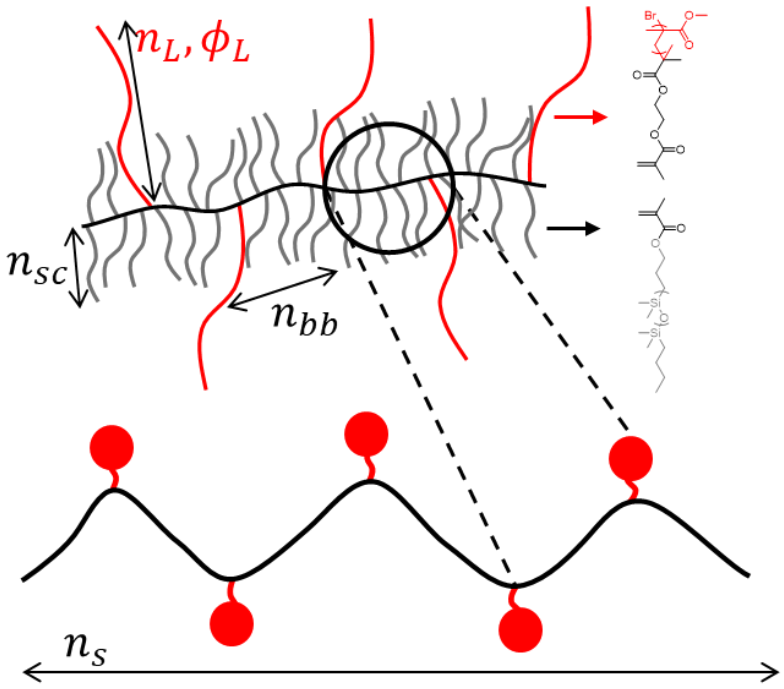

Figure 9.4: Graft copolymers: an LBL plastomer iteration. LBL architectural parameters of brush length (n_{bb}), side chain length (n_{sc}) and linear block length (n_L) can be embedded into an over-arching graft copolymer structure. In theory the LBL parameters will maintain control over

network elasticity, while the extended strand length (n_s) and repeat units ($n_r = n_s/n_{bb}$) will control material strength.

9.4 Programming Functionality into Core-Shell Brushes

Brush side chains serve an important role in regulating the mechanical properties of LBL plastomer materials, however, besides the rubbery requirement (i.e. operating temperatures above T_g, or T_m of side chains), there are not many resections on their chemistry. Naturally this suggests future research via tuning the LBL platform with a wide range of chemically distinct side chains (e.g. polyolefins, polyacrylates, etc.) for specified application (e.g. tackiness, adhesion, etc.). Although this is an admirable avenue, it can be taken one step further by incorporating multiple functionalities into a single side chain in a core-shell brush[80,81] approach (**Figure 9.5**). Note that this concept is distinct from random graft copolymer mixtures (**Section 9.3**) as the isolated core (n_c) is theoretically prohibited from interacting with neighboring brushes and the shell matrix.

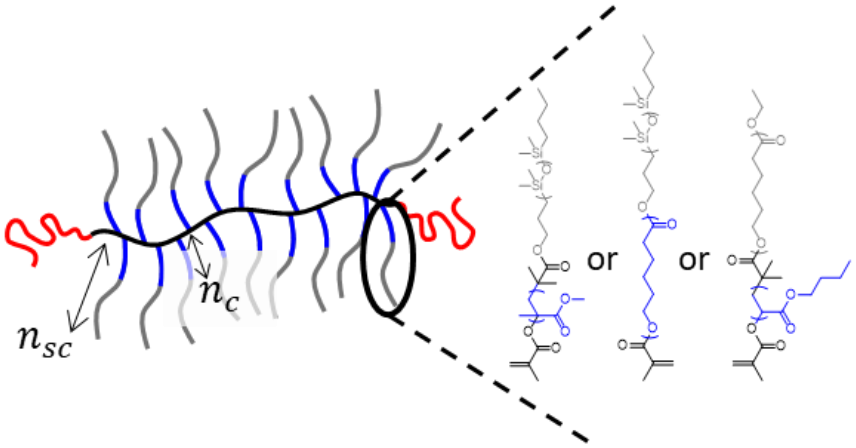

Figure 9.5: Core-shell brush LBL plastomers. A representation of possible core-shell brush components, where the inner core is either glassy PMMA or crystallizable PCL components. Crystallizable PCL shells can also be used in targeted applications.

The programmed copolymer side chains can range from conjugated polymers[82] to enable tissue-like electronic devices or polymers instilled with controlled release mechanisms[83] to empower a new generation of long-term drug release vessels. As these polymers are buried in the core, they are expected to have minimal effect on the overall LBL mechanical performance. As a proof-of-concept, diblock macromonomer side chains containing an outer rubbery PDMS shell and glassy PMMA or crystallizable polycaprolactone (PCL) core could be synthesized into the LBL platform. As these glassy and crystal domains are sequestered from neighboring brushes, they should not affect the material softness. If successful, tissue-mimetic materials with potentially 75% by weight of traditionally rigid MMA can be achieved. Conversely, crystalline PCL can be encoded into the brush shell with tunable length in order to interact with neighboring brushes. The result is a hard material at room temperature that can melt to tissue-like mechanics on demand. Here, the novelty lies in the ability to decouple melting temperature from LBL firmness, which are both n_{sc} dependent. This will enable hard biomedical devices which can be easily inserted into the body, but then exhibit tissue-like mechanics upon melting at body temperature. These types of initial tests would serve to establish structure-property correlations that can translate into more complex chemistries, functionality and applications.

9.5 Outlook and Concluding Remarks

This dissertation has aimed to advance the LBL plastomer platform by (i) decoding the platform's unique deformation mechanism encoded into a single network strand and (ii) demonstrating that these synthetic materials not only achieve tissue-like elasticity, but is the only material platform to achieve unprecedented control over softness and firmness to traverse the entire elastic landscape. Although additional future work is required to fully explore the

platform's architectural boundaries and expand current understanding of LBL self-assembly, LBL plastomers appear to offer limitless tunable pathways that can be exploited for equally limitless future applications.

REFERENCES

(1) Doraiswamy, V.; Dehdashti, B.; Feng, X.; Lu, B.; Poston, R.; Khalpey, Z.; Ghaffari, R.; Huang, Y.; Slepian, M. J.; Rogers, J. A. Conformal piezoelectric energy harvesting and storage from motions of the heart, lung and diaphragm. *PNAS* **2014**, *111*, 1927-1932.

(2) Thuruthel, T. G.; Shih, B.; Laschi, C.; Tolley, M. T. Soft robot perception using embedded soft sensors and recurrent neural networks. *Sci. Robot.* **2019**, *4*, eaav1488.

(3) Storm, C.; Pastore, J. J.; MacKintosh, F. C.; Lubensky, T. C.; Janmey, P. A. Nonlinear elasticity in biological gels. *Nature* **2005**, *435*, 191-194.

(4) Carrillo, J.-M. Y.; MacKintosh, F. C.; Dobrynin, A. V. Nonlinear elasticity: from single chain to networks and gels. *Macromolecules* **2013**, *46*, 3679-3692.

(5) Fung, Y. C. *Biomechanics: Mechanical Properties of Living Tissues*, 2nd ed.; Springer, 1993.

(6) Holzapfel, G.A. Biomechanics of soft tissue. In *Handbook of Material Behavior Models*, 1st ed.; LeMaitre J., Eds.; Academic press, 2001, p 1057-1071.

(7) Jabareen, M.; Mallik, A. S.; Bilic, G.; Zisch, A. H.; Mazza, E. Relation between mechanical properties and microstructure of human fetal membranes: an attempt towards a quantitative analysis. *Eur. J. Obstet. Gynecol. Reprod. Biol.* **2009**, *144*, 5134-5141.

(8) Muiznieks, L. D.; Keeley, F. W. Molecular assembly and mechanical properties of the extracellular matrix: A fibrous protein perspective. *Biochimica et Biophysica Acta* **2013**, *1832*, 866-875.

(9) Shoulders, M. D.; Raines, R. T. Collagen structure and stability. *Annu. Rev. Biochem.* **2009**, *78*, 929-958.

(10) Orgel, J. P. R. O.; Irving, T. C.; Miller, T.; Wess, T. J. Microfibrillar structure of type I collagen in situ. *PNAS* **2006**, *103*, 9001-9005.

(11) Depalle, B.; Qin, Z.; Shefelbine, S. J.; Buehler, M. J. Influence of cross-link structure, density and mechanical properties in the mesoscale deformation mechanisms of collagen fibrils. *J. Mech. Behav. Biomed. Mater.* **2015**, *52*, 1-13.

(12) Roy, S.; Boss, C.; Rezakhaniha, R.; Stergiopulos, N. Experimental characterization of the distribution of collagen fiber recruitment. *J. Biorheology* **2010**, *24*, 84-93.

(13) Blair, G. W. S. A new criterion for expressing the 'intensity of firmness' of soft bodies. *Nature* **1943**, *152*, 412.

(14) Faber, T. J.; Jaishankar, A.; McKinley, G. H.; Describing the firmness, springiness and rubberiness of food gels using fractional calculus. Part I: Theoretical framework. *Food Colloids* **2017**, *62*, 311-324.

(15) Brown, T.; Brown, S.; Murphy, T. Breast durometer (mammometer): A novel device for measuring soft-tissue firmness and its application is cosmetic breast surgery. *Aesthetic. Plast. Surg.* **2017**, *41*, 265-274.

(16) Juarez, B.; King. J. J.; Bachlava, E.; Wentzell, A. M.; Mills, J. M. Methods and compositions for watermelon firmness. US Patent 10,036,032, July 31, 2018.

(17) Kraft, E. Varying firmness mattress. US Patent 4,999,868, May 11, 1990.

(18) Dobrynin, A. V.; Carrillo, J. Y. Universality in nonlinear elasticity of biological and polymeric networks and gels. *Macromolecules* **2011**, *44*, 140-146.

(19) Carrillo, J.-M. Y., MacKintosh, F. C. & Dobrynin, A. V. Nonlinear elasticity: from single chain to networks and gels. *Macromolecules* **2013**, *46*, 3679-3692.

(20) Fung, Y. C. Elasticity of soft tissues in simple elongation. *Am. J. Physiol*. **1967**, *213*, 1532-1544.

(21) Gent, A. N. A new constitutive relation for rubber. *Rubber Chem. Technol.* **1996**, *69*, 59-61.

(22) Ogden, R. W. Large deformation isotropic elasticity−on the correlation of theory and experiment for incompressible rubberlike solids. *Proc. R. Soc. Lond. A* **1972**, *328*, 567-583.

(23) Ogden, R. W. *Non-linear Elastic Deformations*; Dover Publications: New York, 1997.

(24) Krag, S.; Andreassen, T. T. Mechanical properties of human lens capsule. *Prog. Retin. Eye Res.* **2003**, *22*, 749-767.

(25) Roberts, T. J. Contribution of elastic tissues to the mechanics and energetics of muscle function during movement. *J. Exp. Biol.* **2016**, *219*, 266-275.

(26) Zhou, B.; Xu, F.; Chen, C. Q. Strain rate sensitivity of skin tissue under thermomechanical loading. *Phil. Trans. R. Soc.* **2010**, *368*, 679-690.

(27) Keith, A. N.; Vatankhah-Varnosfaderani, M.; Clair, C.; Fahimipour, F.; Dashtimoghadam, E.; Lallam, A.; Sztucki, M.; Ivanov, D. A.; Liang, H.; Dobrynin, A. V.; Sheiko, S. S. Bottlebrush bridge between soft gels and firm tissues. *ACS Cent. Sci.* **2020**, *6*, 413-419.

(28) Krejsa, M. R.; Koenig, J. L. A review of sulfur crosslinking fundamentals for accelerated and unaccelerated vulcanization. *Rubber Chem. Technol.* **1993**, *66*, 376-410.

(29) Jacobs, M.; Liang, H.; Dashtimoghadam, E.; Morgan, B. J.; Sheiko, S. S.; Dobrynin, A. V. Nonlinear elasticity and swelling of comb and bottlebrush networks. *Macromolecules* **2019**, *52*, 5095-5101.

(30) Troegel, D.; Stohrer, J. Recent advances and actual challenges in late transition metal catalyzed hydrosilylation of olefins from an industrial point of view. *Coord. Chem. Rev.* **2011**, *11*, 1440-1459.

(31) Yuk, H.; Zhang, T.; Parada, G. A.; Liu, X.; Zhao, X. Skin-inspired hydrogel-elastomer hybrids with robust interfaces and functional microstructures. *Nat. Comm.* **2016**, *7*, 12028.

(32) Ranzani, T.; Gerboni, G.; Cianchetti, M.; Menciassi, A. A bioinspired soft manipulator for minimally invasive surgery. *Bioinspir. Biomim.* **2105**, 10, 035008.

(33) A Rubinstein, M.; Colby, R, H. *Polymer Physics*, 1st ed.; Oxford University Press, 2003.

(34) Daniel. W. F. M.; Burdyńska, J.; Vatankhah-Varnosfaderani, M.; Matyjaszewski, K.; Paturej, J.; Rubinstein, M.; Dobrynin, A. V.; Sheiko, S. S. Solvent-free, supersoft and superelastic bottlebrush melts and networks. *Nat. Mater.* **2016**, *15*, 183-189.

(35) Urayama, K.; Kawamura, T.; Kohjiya, S. Elastic modulus and equilibrium swelling of networks crosslinked by end-linking oligodimethylsiloxane at solution state. *J. Chem. Phys.* **1996**, *105*, 4833.

(36) Rubinstein, M; Colby, R. H. Network modulus and superelasticity. *Macromolecules* **1994**, *27*, 3191-3198.

(37) Feig, V. R.; Tran, H.; Lee, M.; Bao, Z. Mechanically tunable conductive interpenetrating network hydrogels that mimic the elastic moduli of biological tissue. *Nature Comm.* **2018**, *9*, 2740.

(38) Li, J.; Suo, Z.; Vlassak, J. J. Stiff, strong and tough hydrogels with good chemical stability. *J. Mater. Chem. B* **2014**, *2*, 6708-6713.

(39) Yue, Y. F.; Haque, M. A.; Kurokawa, T.; Nakajima, T.; Gong, J. P. Lamellar hydrogels with high toughness and ternary tunable photonic stop-band. *Adv. Mater.* **2013**, *25*, 3106-3110.

(40) Ohmori, K.; Bin, I. A.; Seki, T.; Liu, C.; Mayumi, K.; Ito, K.; Takeoka, Y. Molecular weight dependency of polyrotaxane cross-lined polymer gel extensibility. *Chem. Commun.* **2016**, *52*, 13757.

(41) Haraguchi, K.; Takehisa, T. Nanocomposite hydrogels: a unique organic-inorganic network structure with extraordinary mechanical, optical and swelling/de-swelling properties. *Adv. Mater.* **2002**, *14*, 1120-1124.

(42) Gong, J. P.; Katsuyama, Y.; Kurokawa, T.; Osada, Y. Double-network hydrogels with extremely high mechanical strength. *Adv. Mater.* **2003**, *15*, 1155-1158.

(43) Durcot, E.; Chen, Y.; Bulters, M.; Sijbesma, R. P.; Creton, C. Toughening elastomers with sacrificial bonds and watching them break. *Science* **2014**, *344*, 186-189.

(44) Sheiko, S. S.; Dobrynin, A. V. Architectural code for rubber elasticity: from super-soft to super-firm materials. *Macromolecules* **2019**, *52*, 7531-7546.

(45) Vatankhah-Varnosfaderani, M.; Daniel, W. F. M.; Everhart, M. H.; Pandya, A. A.; Liang, H.; Matyjaszewski, K.; Dobrynin, A. V.; Sheiko, S. S. Mimicking biological stress-strain behavior with synthetic elastomers. *Nature* **2017**, *549*, 497-501.

(46) Vatankhah-Varnosfaderani M.; Daniel, W. F. M.; Zhushma, A. P.; Li, Q.; Morgan, B. J.; Matyjaszewski, K.; Armstrong, D. P.; Spontak, R. J.; Dobrynin, A. V.; Sheiko, S. S. Bottlebrush elastomers: a new platform for freestanding electroactuation. *Adv. Mater.* **2017**, *29*, 1604209.

(47) Verduzco, R.; Li, X.; Pesek, S. L.; Stein, G. E. Structure, function, self-assembly, and applications of bottlebrush copolymers. *Chem. Soc. Rev.* **2015**, *44*, 2405-2420.

(48) Feng, C.; Li, Y.; Yang, D.; Hu, J.; Zhang, X.; Huang, X. Well-defined graft copolymers: from controlled synthesis to multipurpose applications. *Chem. Soc. Rev.* **2011**, *40*, 1282-1295.

(49) Lee, H.; Pietrasik, J.; Sheiko, S. S.; Matyjaszewski, K. Stimuli-responsive molecular brushes. *Prog. Polym. Sci.* **2010**, *35*, 22-44.

(50) Tasdelen, M. A. Diels-alder "click" reactions: recent applications in polymer and material science. *Polym. Chem.* **2011**, *2*, 2133-2145.

(51) Meldal, M.; Tornøe, C. W. Cu-catalyzed azide-alkyne cycloaddition. *Chem. Rev.* **2008**, *108*, 2952-3015.

(52) Bielawski, C. W.; Grubbs, R. H. Living ring-opening metathesis polymerization. *Prog. Polym. Sci.* **2007**, *32*, 1-29.

(53) Perrier, S. 50th Anniversary perspective: RAFT polymerization – a user guide. *Macromolecules* **2017**, *50*, 7433-7447.

(54) Matyjaszewski, K. Atom transfer radical polymerization (ATRP): Current status and future perspectives. *Macromolecules*, **2012**, *45*, 4015-4039.

(55) Nuyken, O.; Pask, S. D. Ring-opening polymerization – An introductory review. *Polymers* **2013**, *5*, 361-403.

(56) Eisch, J. J. Fifty years of Ziegler-Natta polymerization: from serendipity to science. A personal account. *Organometallics* **2012**, *31*, 4917-4932.

(57) Yu, J. M.; Dubois, Ph.; Teyssié, Ph.; Jérôme, R. Syndiotactic Poly(methyl methacrylate)(sPMMA)-Polybutadiene (PBD)-sPMMA Triblock Copolymers: Synthesis, Morphology, and Mechanical Properties. *Macromolecules* **1996**, *29*, 6090-6099.

(58) Erk, K. A.; Henderson, K. J.; Shull, K. R.; Strain Stiffening in Synthetic and Biopolymer Networks. *Biomacromolecules* **2010**, *11*, 1358-1363.

(59) Ohta, T.; Kawasaki, K. Equilibrium morphology of block copolymer melts. *Macromolecules* **1986**, *19*, 2621-2632.

(60) Bates, F. S.; Fredricksom, G. H. Block copolymer thermodynamics: theory and experiment. *Annu. Rev. Phys. Chem.* **1990**, *41*, 525-557.

(61) Vatankhah-Varnosfaderani, M.; Keith, A. N.; Cong, Y.; Liang, H.; Rosenthal, M.; Sztucki, M.; Clair, C.; Magonov, S.; Ivanov, D. A.; Dobrynin, A. V.; Sheiko, S. S. Chameleon-like elastomers with molecularly encoded strain-adaptive stiffening and coloration. *Science* **2018**, *359*, 1509-1513.

(62) Luo, Y.; Montarnal, D.; Kim, S.; Shi, W.; Barteau, K. P.; Pester, C. W.; Hustad, P. D.; Christianson, M. D.; Fredrickson, G. H.; Kramer, E. J.; Hawker, C. J. Poly(dimethylsiloxane-b-methyl methacrylate): A promising candidate for sub-10 nm patterning. *Macromolecules* **2015**, *48*, 3422-3430.

(63) Sheiko, S. S.; Silva, M.; Shirvaniants, D.; LaRue, I.; Prokhorova, S.; Moeller, M.; Beers, K.; Matyjaszewski, K. *J. Am. Chem. Soc.* **2003**, *125*, 6725-6728.

(64) Clair, C.; Lallam, A.; Rosenthal, M.; Sztucki, M.; Vatankhah-Varnosfaderani, M.; Keith, A. N.; Cong, Y.; Liang, H.; Dobrynin, A. V.; Sheiko, S. S.; Ivanov, D. A. Strained bottlebrushes in super-soft physical networks. *ACS. Macro. Lett.* **2019**, *8*, 530-534.

(65) Foster, M. P.; Mcelroy, C. A.; Amero, C. D. Solution NMR of large molecules and assemblies. *Biochemistry* **2007**, *46*, 331-340.

(66) Burdyńska, J.; Daniel. W.; Li, Yuanchao, Robertson, B.; Sheiko, S. S.; Matyjaszewski, K. Molecular bottlebrush with bimodal length distribution of side chains. *Macromolecules* **2015**, *48*, 4813-4822.

(67) Liang, H.; Wang, Z.; Dobrynin A. V. Scattering from melts of combs and bottlebrushes: molecular dynamics simulations and theoretical study. *Macromolecules* **2019**, *52*, 5555-5562.

(68) Yu, L. T.; Latorre, G.; Marotta, J.; Batich, C.; Hardt, N. S. In vitro measurement of silicone bleed form breast implants. *Plast. Reconstr. Surg.* **1996**, *97*, 756-764.

(69) Coroneos, C. J.; Selber, J. C.; Offodile, A. C.; Butler, C. E.; Clements, M. W. US FDA breast implant postapproval studies: long-term outcomes in 99,993 patients. *Ann. Surg.* **2019**, *269*, 30-36.

(70) Shreiber, D. I.; Hao, H.; Elias, R. A. Probing the influence of myelin and glia on the tensile properties of the spinal cord. *Biomech. Model. Mechanobiol.* **2009**, *8*, 311-321.

(71) Rashid, B.; Destrade, M.; Gilchrist, M. D. Mechanical characterization of brain tissue in tension at dynamic strain rates. *J. Mech. Behav. Biomed. Mater.* **2014**, *33*, 43-54.

(72) Alkhouli, N.; Mansfield, J.; Green, E.; Bell, J.; Knight, B.; Liversedge, N.; Tham, J. C.; Welbourn R.; Shore, A. C.; Kos, K.; Winlove, C. P. The mechanical properties of human adipose tissues and their relationships to the structure and composition of the extracellular matrix. *Am. Physiol. Soc.* **2013**, *305*, E1427-E1435.

(73) Liang, H.; Wang, Z.; Dobrynin, A. V. Strain-adaptive self-assembled networks of linear-bottlebrush-linear copolymers. *Macromolecules* **2019**, *52*, 8617-8624.

(74) Fantner, G. E.; Oroudjev, E.; Schitter, G.; Golde, L. S.; Thumer, P.; Finch, M. M.; Turner, P.; Gutsmannm T.; Morse, D. E.; Hansma, H.; Hansma, P. K. Sacrifical bonds and hidden length: unraveling molecular mesostructures in tough materials. *Biophys. J.* **2006**, *90*, 1411-1418.

(75) Levi, A. E.; Lequieu, J.; Home, J. D.; Bates, M. W.; Ren, J. M.; Delaney, K. T.; Fredrickson, G. H.; Bates, C. M. Miktoarm stars via grafting-through copolymerization: Self-assembly and the star-to-bottlebrush transition. *Macromolecules* **2019**, *52*, 1794-1802.

(76) Ramirez, A. L. B.; Kean, Z. S.; Orlicki, J. A.; Champhekar, M.; Elsakr, S. M.; Krause, W. E.; Craig, S. L. Mechanochemical strengthening of a synthetic polymer in response to typically destructive shear forces. *Nat. Chem.* **2013**, *5*, 757-761.

(77) Khandpur, A. K.; Foerster, S.; Bates, F. S.; Hamley, I. W.; Ryan, A. J.; Bras, W.; Almdal, K.; Mortensen, K. Polyisoprene-polystyrene deblock copolymer phase diagram near the order-disorder transition. *Macromolecules* **1995**, *28*, 8796-8806.

(78) Han, C. D.; Kim. J.; Kim, J. K. Determination of the order-disorder transition temperature of block copolymers. *Macromolecules* **1989**, *22*, 393-394.

(79) Gehlsen, M. D.; Almdal, K.; Bates, F. S. Order-disorder transition: Diblock versus triblock copolymers. *Macromolecules* **1992**, *25*, 939-943.

(80) Lee, H.-i.; Jakubowski, W.; Matyjaszewski, K.; Yu, S.; Sheiko, S. S. Cylindrical core-shell brushes prepared by a combination of ROP and ATRP. *Macromolecules* **2006**, *39*, 4983-4989.

(81) Djalali, R.; Li, S.-Y.; Schmidt, M. Amphipolar core-shell cylindrical brushes as templates for the formation of gold clusters and nanowires. *Macromolecules* **2002,** *35*, 4282-4288.

(82) Zhou, H.; Yang, L.; You, W. Rational design of high performance conjugated polymers for organic solar cells. *Macromolecules* **2012**, *45*, 607-632.

(83) Kamaly, N.; Yameen, B.; Wu, J.; Farokhzad, O. C. Degradable controlled-release polymers and polymeric nanoparticles: mechanisms of controlling drug release. *Chem. Rev.* **2016**, *116*, 2602-2663.